Hardware Invariant Protocol Disruptive Interference and an Analysis of Stochastic Plane Wave Coupling to Uniform Transmission Lines

by

Ian Jeffrey

B.Sc. Computer Engineering,

University of Manitoba 2002

Submitted in partial fulfillment of the requirements
for the degree of Master of Science in Electrical Engineering
in the Graduate Faculty of the
University of Manitoba, 2004

Winnipeg, Manitoba

THE UNIVERSITY OF MANITOBA

FACULTY OF GRADUATE STUDIES

*****

COPYRIGHT PERMISSION

Hardware Invariant Protocol Disruptive Interference and an Analysis of Stochastic Plane Wave Coupling to Uniform Transmission Lines

BY

Ian Jeffrey

A Thesis/Practicum submitted to the Faculty of Graduate Studies of The University of Manitoba in partial fulfillment of the requirement of the degree

Of

MASTER OF SCIENCE

Abstract

This research introduces a novel electromagnetic interaction problem referred to as Hardware Invariant Protocol Disruptive Interference or HIPDI. It is theorized that HIPDI should be parameterized from the target protocol using the developed concept of *hardware aperture*. This theory is applied to the 100BaseTX Ethernet protocol and, through experimental analysis, it is shown that low-level, narrowband, differential-mode voltage levels radiatively coupled to a 100BaseTX Ethernet twisted-pair are capable of seriously degrading network throughput. This degradation has been achieved for all considered experiments independent of the network hardware implementation.

As a consequence of HIPDI research, an attempt is made to determine the termination voltage distributions resulting from stochastic fields coupled to uniform transmission lines. The approach uses Monte Carlo analysis and the theory of transformation of random variables as applied to the BLT solution to the plane wave coupling problem. It is shown that the complex nature of this problem makes Monte Carlo analysis necessary for arbitrary transmission line parameters. In specific cases, it is demonstrated that exponential, gamma and Rayleigh densities give good approximations to the termination voltage distributions. Finally, in the case of matched loads and specific field randomness, an empirical approximation is obtained for the termination voltage densities.

Contributions

This thesis contains the development of a novel electromagnetic interaction problem appropriately named Hardware Invariant Protocol Disruptive Interference (HIPDI). The HIPDI problem asks: *Is it possible to disrupt a communication channel independent of the communication protocol in a manner that is undetectable at the system level?* Developed theory of a protocol's *hardware aperture* has been used to demonstrate the existence and potential threat of HIPDI for 100BaseTX Ethernet.

The investigation of random plane wave coupling to a uniform transmission line is shown to be very sensitive to the field and line parameters. The development of a Monte Carlo analysis tool for determining the probability density functions of the line termination voltages greatly simplifies EMC analysis and demonstrates, that in many cases, the probability density functions can be accurately approximated with exponential, gamma or Rayleigh distributions.

Finally, this work contains an empirical solution for the voltage distributions arising from a plane wave source coupling to a matched transmission line when the source is located horizontally from the transmission line with equally likely polarization and angle of incidence.

Acknowledgments

First, I wish to thank Professor Joe LoVetri, my thesis advisor. I express great gratitude for his ideas and founding contributions to HIPDI as well as his experience with, and deep understanding of, the stochastic coupling problem. Without his knowledge, ideas and guidance the contributions of this thesis would not have been possible.

For their extreme efforts in HIPDI experimentation I wish to thank Mr. Colin Gilmore and Mr. Greg Seimens who, by assisting in the experimental setup, data collection and analysis made it possible to prove that HIPDI is indeed a severe threat. I also wish to thank Dr. Bob McLeod for his extensive expertise of the Ethernet protocol as well as his assistance in the formulation of HIPDI for 100BaseTX Ethernet.

Thanks to Jem Berkes, Domo Schaub and Tim Czyrnyj for their expert programming advice. Thanks also to Behzad Kordi for his help with the Continuous Wavelet Transform and countless other problems encountered along the way.

Indescribable gratitude is extended to Ms. Laura Chatelain for her love, understanding, patience and support since the day we met.

Finally, thanks to my parents and friends for their love, support and encouragement.

Nomenclature

AM	- Amplitude Modulation
CDF	- Cumulative Distribution Function
CSMA	- Carrier Sense Multiple Access
CWT	- Continuous Wavelet Transform
CW	- Continuous Wave
EMC	- Electromagnetic Compatibility
EMI	- Electromagnetic Interference
EMP	- Electromagnetic Pulse
FFT	- Fast Fourier Transform
GPIB	- General Purpose Interface Bus
GTEM	- Gigahertz Transverse Electromagnetic
GUI	- Graphical User Interface
HIPDI	- Hardware Invariant Protocol Disruptive Interference
HPM	- High-power Microwave
MLE	- Maximum Likelihood Estimation
MLT-3	- MultiLevel Transition-3
NIC	- Network Interface Controller
OSI	- Open System Interconnect
PCI	- Peripheral Component Interconnect
PDF	- Probability Density Function
RF	- Radio Frequency
RFC	- Request For Comments
RV	- Random Variable
TCP	- Transport Control Protocol
TEM	- Transverse Electromagnetic
UDP	- User Datagram Protocol
UTP	- Unshielded Twisted Pair

Table of Contents

List of Figures

List of Tables

CHAPTER 1. INTRODUCTION

The field of electromagnetic compatibility and interference (EMC/EMI) has developed over the years into an area of great interest and study. Typically, an EMC design engineer is concerned with ensuring that electronic devices function within specific standards in terms of both the devices susceptibility to- and generation of electromagnetic radiation. However, in certain cases, such protection is prohibited by the very nature of the electronic system in question. Consider the novel electromagnetic interaction problem that asks: *Is it possible to couple energy into a communication channel that will disrupt communication independent of the hardware implementation?* Clearly, if it is possible to couple energy that is indistinguishable from the protocol signalling being used for communication, protection of the hardware used to interpret the protocol will be impossible. This theorized interference is called Hardware Invariant Protocol Disruptive Interference (HIPDI) and is one of two primary foci of this thesis. In Chapter 2 HIPDI is formally introduced and appropriate theory is developed such that HIPDI waveforms can be parameterized for any given protocol. This procedure is exhibited for the specific case of 100BaseTX Ethernet, a protocol that operates over twisted-pair, and verification of HIPDI is presented in the form of experimental analysis for various network implementations.

Due to the results of HIPDI research it was desired to determine probability distributions for the termination voltages arising from stochastic field coupling to randomly oriented twisted-pairs. Unfortunately, the majority of the literature available to an EMC engineer involves the solutions to deterministic problems where the physics of the environment in question are known. It was discovered that very few techniques are available for dealing with stochastic transmission line coupling problems. The lack of previous research is not surprising, for even in the deterministic case, the transmission line coupling problem is complicated. Due to the limited history of stochastic coupling problems, the radiative coupling of a randomly oriented Ethernet twisted-pair proved to be

too difficult for analysis. Instead, the secondary purpose of this thesis is to analyze the problem of radiating a deterministic, uniform, lossless transmission line with a random plane wave in order to examine the resulting termination voltage (or current) distributions. Therefore, Chapter 3 reviews the BLT solution for transmission line termination voltages and currents caused by a plane wave incident on a transmission line in the deterministic case, while Chapter 4 reports on a statistical tool developed in Matlab for generating Monte Carlo densities from the BLT equation when the impinging plane wave is stochastically defined. The statistical tool is equipped with the ability to fit gamma, exponential and Rayleigh distributions to the obtained results and it is shown that in some cases, these functions accurately exhibit the random nature of the resulting voltage and current distributions.

In an attempt to obtain analytic probability density functions for the termination voltages, Chapter 5 deals extensively in the theory required for finding closed-form analytic solutions to the desired probability densities and although application of the theory proves to be too complicated even in the simplest cases, Chapter 6 obtains an empirical density function for the transmission line termination voltages in a specific case.

CHAPTER 2. HARDWARE INVARIANT PROTOCOL DISRUPTIVE INTERFERENCE

In this chapter, the novel EMC/EMI problem referred to as Hardware Invariant Protocol Disruptive Interference (HIPDI) is introduced. HIPDI is then theoretically discussed. The developed theory is applied to the specific protocol of 100BaseTX Ethernet for which experiments and results are presented.

2.1 MOTIVATION

Technological advancements have made transfer of information possible on a scale unfathomable a generation ago. From the internet to local networks there exists a vast array of protocols for relaying data over both wired and wireless mediums. While there is large interest in methods for protecting the security and integrity of an individual's information via encryption, network security from a physical standpoint is often neglected. Previous research has shown that high-power microwave (HPM) pulses pose a serious threat to network communications and any other electronic system [1]-[5]. Although capable of damaging communication network hardware, HPM is both an overt threat and is expensive to generate. This suggests that perhaps there exists a greater threat to network communications: an inexpensive, covert threat that is undectable at the system level. This chapter attempts to theorize the existence of such a threat for which no immediate protection technique is available. The methodology developed exploits the very protocol being used for data communication to parameterize interference radiation. It is an attempt to determine if low-power, simple waveform, radiated electromagnetic interference can cause degradation to network throughput without damaging network hardware (or, in the case of a computer network, undetectable to the user in terms of all

other computer functionality). Finally, the goal is to find interference that will disrupt network communication regardless of the physical nature of the network. Such interference is referred to as Hardware Invariant Protocol Disruptive Interference or HIPDI.

2.2 HIPDI AND THE HARDWARE APERTURE

Theoretically, the existence of HIPDI is verified by considering interference that once coupled to the medium of data communication (wired or wireless), is indistinguishable from data. If it were possible to create such interference, then the *hardware interpreter* (the device responsible for deciphering the protocol) would be constantly occupied with false information, rendering the communication channel useless.

As hardware interpreters for a given protocol are designed by various different manufacturers, their sole commonality must be that they respond to the protocol appropriately. Beyond this, different hardware implementations may exhibit arbitrarily different behaviour. Because of such hardware differences, disruptive interference that is completely distinct from communication cannot possible have hardware independent effects. Furthermore, interference outside of the set of parameters that defines a protocol may be protected against using physical means. As a simple example consider the interference frequency. If a protocol is limited by a maximum frequency, interference above this frequency can simply be filtered at the hardware input. It is the idea that a hardware interpreter is designed to respond to the protocol that is referred to as the *hardware aperture* of the protocol: *all hardware used to interpret a protocol produces an interference aperture to which the hardware must respond!*

By extracting as much information as possible from the protocol in question, parameterization of HIPDI interference is possible. Intuitively, this would suggest using radiated patterns that emulate protocol bitstreams. While such radiation would not be overly expensive to generate, the research reported herein looks for the simplest waveforms possible. Therefore, only continuous wave (CW) and amplitude modulation (AM) radiation are considered.

In the following discussion, HIPDI is developed for the 100BaseTX Ethernet protocol. In the development of HIPDI for this wired communication scheme, it is assumed that the coupling of energy into the medium is possible. Therefore, the search is for *quasi*-hardware invariant interference as the physical orientation of the channel will affect the required radiation power level. The deterministic coupling problem has been studied extensively [6] and is not considered for the remainder of this chapter.

2.3 A SUMMARY OF 100BASETX ETHERNET

The following sections describe the 100BaseTX Ethernet protocol beginning with the physical medium and proceeding to the logical signalling scheme and data encapsulation. It is from these features that the parameters of HIPDI will be extracted.

2.3.1 The 100BaseTX Physical Medium

100BaseTX Ethernet is a common protocol used for internet communications by personal computers (PCs). The hardware interpreters of the protocol are commonly referred to as network interface cards (NICs). The protocol typically operates over CAT-5 unshielded twisted-pair (UTP) cables which are characterized by four twisted pairs of lines protected by a plastic sheath as shown in Fig. 2-1.

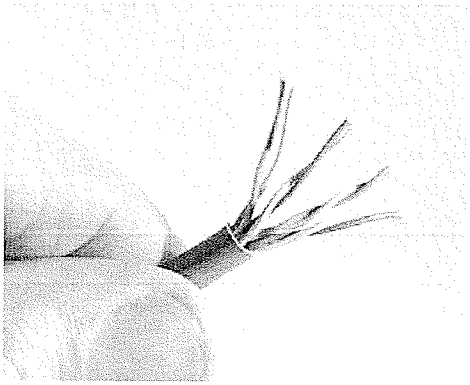

Figure 2-1. Cat-5 UTP twisted-pairs

The cables have a 100Ω characteristic impedance and are rated up to 100 MHz (although enhanced cable which is rated to 350 MHz is available). Shielded CAT-5 cables are also available but are generally more expensive and are seldom used in residential or commercial networks. Fig. 2-2 shows the wire pairs of a cross-over CAT-5 cable used to connect a PC to a PC (a non-crossed cable is used to connect a PC to a HUB or other gateway device). Ethernet is capable of half- or full-duplex operation, the later being used primarily in point-to-point links. In full-duplex operation two pairs of wires are used to transmit and receive as denoted by the Tx and Rx pair in Fig. 2-2. The other wires have various purposes depending on the implementation but are not the concern of this research.

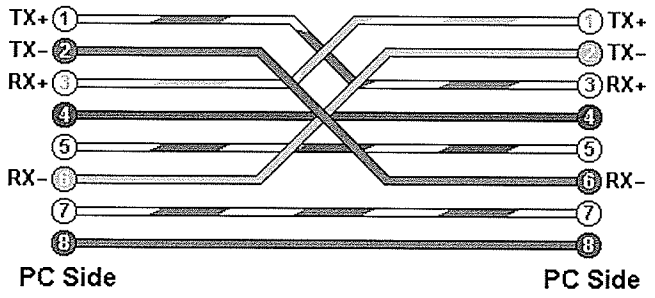

Figure 2-2. Cat-5 twisted-pair usage (PC to PC)

2.3.2 The 100BaseTX Protocol and Physical Signalling

The 100BaseTX protocol transmits data at 100 MBps (megabits per second). In order to achieve this data-rate, two encoding schemes are used. First, every 4 bits of data are encoded by look-up table into a 5 bit string. This encoding is known as 4-bit-to-5-bit or 4b/5b encoding and is used to reduce the number of successive 1's in the 5-bit string as shown in Table 2-1. After 4b/5b encoding, another encoding scheme called Multi-Level Transition-3 or MLT-3 is applied to the 4b/5b encoded data. MLT-3 functions by making use of three logic levels, -1, 0 and 1 represented by -1, 0 and 1 V on the CAT-5 cable.

Table 2-1. 4b/5b Encoding

4b	5b
0000	11110
0001	01001
0010	10100
0011	10101
0100	01010
0101	01011
0110	01110
0111	01111
1000	10010
1001	10011
1010	10110
1011	10111
1100	11010
1101	11011
1110	11100
1111	11101
idle	11111

From the 4b/5b encoded data, MLT-3 transitions from one state to another whenever the 4b/5b data is a logical 1, and remains in its current state whenever the 4b/5b data is 0. In this manner MLT-3 cycles through -1 to 0 to 1 to 0 to -1 etc. This behaviour is most easily represented by the state transition diagram of Fig. 2-3.

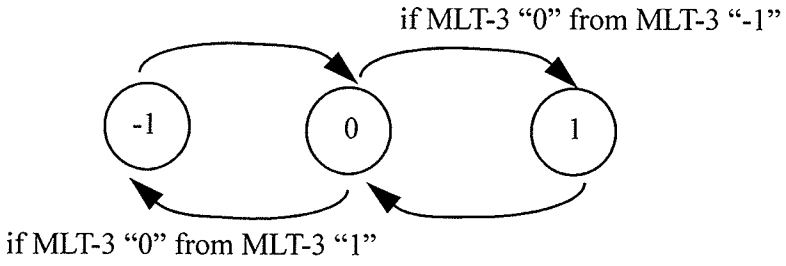

Figure 2-3. MLT-3 state transition diagram

In order to achieve the desired 100 MBps data rate, the MLT-3 signal is transmitted and received at 125 MBps (due to the 4b/5b encoding) resulting in a bit duration of 8 ns. As a consequence, cycling through MLT-3 values from -1 and back to -1 requires four 8 ns bits giving a 32 ns period or a fundamental cycle frequency of 31.25 MHz. This is displayed in Fig. 2-4. Such a waveform only occurs if the MLT-3 signal is transmitting all 1's in a 4b/5b converted bitstream. This is exactly the case for the 100BaseTX Ethernet "idle" signal, which is used in the absence of data transmission to verify link integrity [7]. According to Table 2-1 all other 4b/5b codes contain at least one 0, effectively lengthening the cycle time and reducing the fundamental frequency of the waveform to below 31.25 MHz. This particular encoding scheme was selected to allow 100BaseTX Ethernet to conform with FCC standards for radiated emissions above 30 MHz. An example MLT-3 encoded stream is shown in Fig. 2-5.

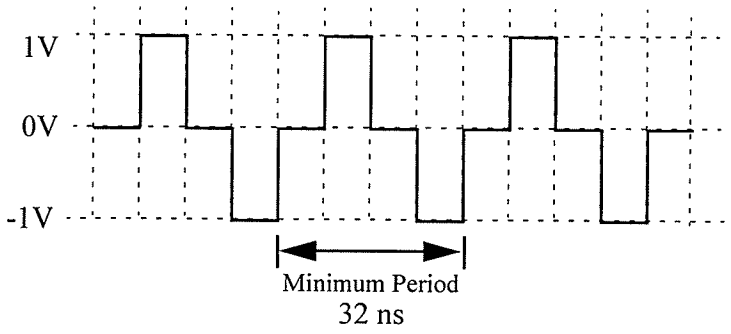

Figure 2-4. Periodicity of the 100BaseTX idle signal

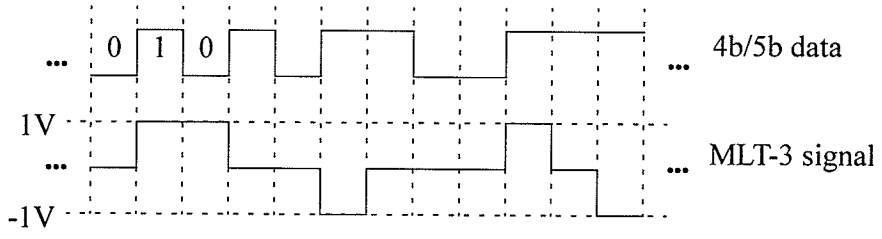

Figure 2-5. Sample 4b/5b to MLT-3 encoded bitstream

In addition to the discussed encoding schemes, Ethernet uses a technique for medium arbitration called Carrier Sense Multiple Access (CSMA). In brief, the Ethernet hardware first tests the line to see if it is in use by another device. If the line is free, transmission is initiated. If the line is occupied (a result commonly referred to as a collision), the hardware waits and then tries again. As a result, it is possible that coupled interference need only resemble data to a degree that suggests to the hardware that the line is in use.

2.3.3 Data Encapsulation and Protocols over Ethernet

The Ethernet Protocol does not end at its physical implementation or encoding schemes. There are stringent rules for the maximum length of data that can be sent in a bundle. Each bundle of data is called an Ethernet frame and the protocol details that the maximum frame length must not exceed 1500 bytes [7]. In addition, each frame contains fields indicating its source and destination address as well as an error correction and control sequence. These are shown in Table 2-2.

Table 2-2. Ethernet Frame Fields

Label	Description
Preamble	7 bytes; alternating ones and zeros
Start of frame delimiter	1 byte alternating ones and zeros stopped by two ones
Destination Address (DA)	6 bytes
Source Address (SA)	6 bytes
Length/Type	4 bytes
Data	*n* bytes of any value (less than or equal to 1500)
Frame check sequence (FCS)	4 bytes 32 bit CRC over DA, SA, Length/Type & Data

The Ethernet protocol is not sufficient to ensure successful delivery of data over a data network. This is accomplished by using higher levels of the Open System Interconnection (OSI) reference model, all of which are transparent to the Ethernet layer and the hardware interpreters. Most computer applications rely on Transport Control

Protocol (TCP). TCP is described officially in RFC 793 [8]. A TCP data bundle is called a packet and TCP contains very strict rules for dealing with network congestion and packet loss. In the case of a lost packet or any other TCP time-out, the protocol will request a resend. Ideally resends should ensure that no packets are ultimately lost but transfer rates will greatly decrease if the required number of resends is substantial. This decrease in transfer rates became very apparent when preliminary experiments were performed using TCP file transfer times as a measurement of throughput. In such experiments, it was difficult to determine if the file transfer was occurring much more slowly than expected, or not occurring at all (that is to say that only some, or all of the TCP packets were being lost or corrupted). With no way of controlling the resend in TCP, packet loss and packet loss rate are more accurately monitored using the User Datagram Protocol (UDP) over 100BaseTX Ethernet, a protocol hat allows for more flexibility.

UDP is described in RFC 768 to have a "minimum of protocol mechanism," meaning very little overhead [9]. Specifically, RFC 768 merely describes how UDP data packets, called datagrams, should be constructed and leaves any error checking or handshaking between network hosts up to the UDP implementer. UDP datagrams are formatted as a 2 byte source port, a 2 byte destination port, 2 bytes for the number of data bytes enclosed and a 2 byte checksum followed by the actual data. Since it is possible to simply send UDP datagrams without worrying about the occurrence of resends on lost or corrupt packets, UDP is well suited for throughput monitoring by simply comparing the total number of datagrams sent and the total number of datagrams received as a measure of throughput. Therefore, UDP was adopted for all performed experiments. Finally, it is noted that while all data packaging undoubtable leads to regular patterns in the transmitted data stream, the encapsulated data should be relatively random from network to network. Hence, the material is simply presented for awareness, and is not explicitly exploited in the parameterization of HIPDI for 100BaseTX Ethernet.

2.3.4 The Parameterization of HIPDI for 100BaseTX Ethernet

It is the physical medium and signalling of the 100BaseTX protocol that defines its hardware aperture. From the physical medium, HIPDI must be differential-mode interference below 100 MHz. The choice of differential-mode interference is required because common-mode interference will be arbitrarily converted to differential-mode by mismatches in hardware amplifiers. This phenomenon is obviously hardware dependent. In addition, common-mode interference is not recognized by differential receivers and can therefore only cause hardware failure. The frequency limit is selected because above 100 MHz the cable itself acts as a filter and other filtration techniques could be used to remove such interference without affecting communication.

From the signalling scheme used in 100BaseTX, further parameters of possible HIPDI interference are inferred. By creating a simulated bitstream using Matlab in which a computer file was appropriately packaged (using both a UDP and Ethernet framing schemes) and encoded using both 4b/5b and MLT-3, the time- and frequency-domain information of the protocol was extractable. The simulated signal was heavily over-sampled to provide a near-analog digital representation. An example is shown in Fig. 2-6. As the time-domain signal provides little insight into HIPDI parameters, the Fast Fourier Transform (FFT) was applied in Matlab in order to analyze the frequency spectrum of a typical bitstream. The FFT in Fig. 2-7 shows that the majority of the energy lies in the 15 to 20 MHz range but the relative magnitude of the FFT is not large enough to suggest that interference in this frequency range will be capable of reducing or halting data throughput more readily than other frequencies. Of course, the frequency of the signal will also vary with time and therefore the overall frequency response may not adequately describe the spectral energy content of the protocol as a function of time.

In order to investigate how the frequency of the protocol varies with time, the Continuous Wavelet Transform (CWT) was applied to both the simulated bitstream as well as a portion of the 100BaseTX idle signal. The purpose herein is not to discuss the CWT but instead to use it as a tool (relevant theory and a recent application to EMC is found in [10] and [11] respectively). In general, the CWT sacrifices some frequency-domain information to preserve some time-domain information. Preliminary applications

of the CWT found that a 10th order complex Gaussian wavelet using 60 frequency points from 0 to 100 MHz gave adequate time and frequency resolution in a tolerable amount of computation time. The upper frequency limit was once again selected due to the nature of the CAT-5 cable. Fig. 2-8 and Fig. 2-9 show the results. As the protocol dictates, the idle signal has a large frequency component that is constant in time at 31.25 MHz. It also exhibits a null at the second harmonic of 62.5 MHz. This is explained by the square nature of the wave and its symmetry about 0 V. In the case of the simulated bitstream, the frequency information is primarily contained from 10-50 MHz Finally, for the case of the idle signal it appears that there is sufficient signal component in the 80-100 MHz range.

From this simple analysis of the time-frequency information of the 100BaseTX protocol, HIPDI can be parameterized. In order to resemble data (or the idle signal), interference energy should be selected in the frequency ranges of 10-50 and 80-100 MHz. In the case of the idle signal, 31.25 MHz is selected as the target frequency. Of additional interest is that the null in the vicinity of 60-70 MHz could play a large role in the hardware aperture because energy coupled to the transmission line at this frequency is not expected to exist during normal data communication. The possibility is sufficient energy in this spectrum could act to confuse the hardware interpreters.

In summary, this brief, theoretical analysis of HIPDI and the 100BaseTX protocol allows the conclusions that for this particular protocol, HIPDI must be differential interference below 100 MHz having fundamental frequency in the ranges of 10-50 MHz, 60-70 MHz or 80-100 MHz. Specifically, 32.15 MHz and 62.5 MHz appear to be good choices.

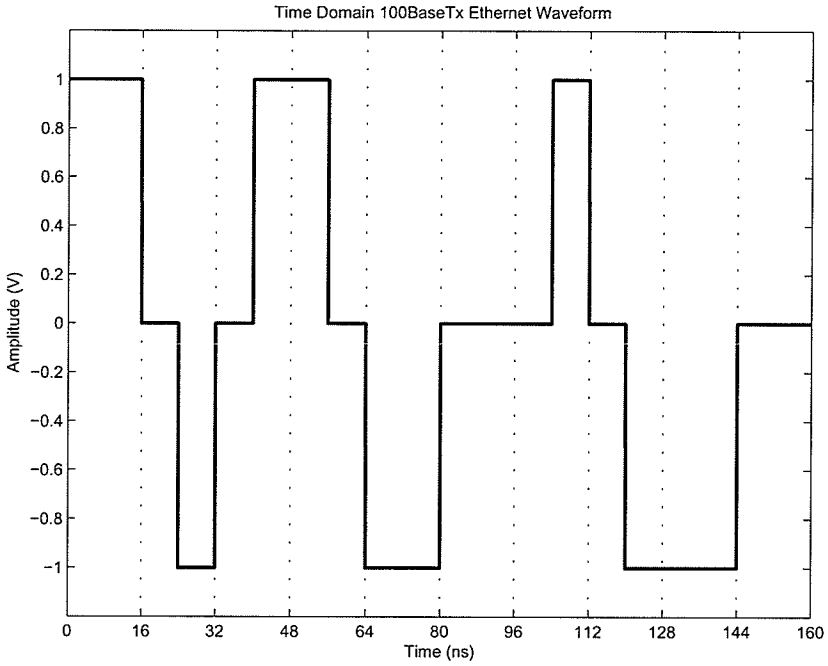

Figure 2-6. Simulated 100BaseTX bitstream

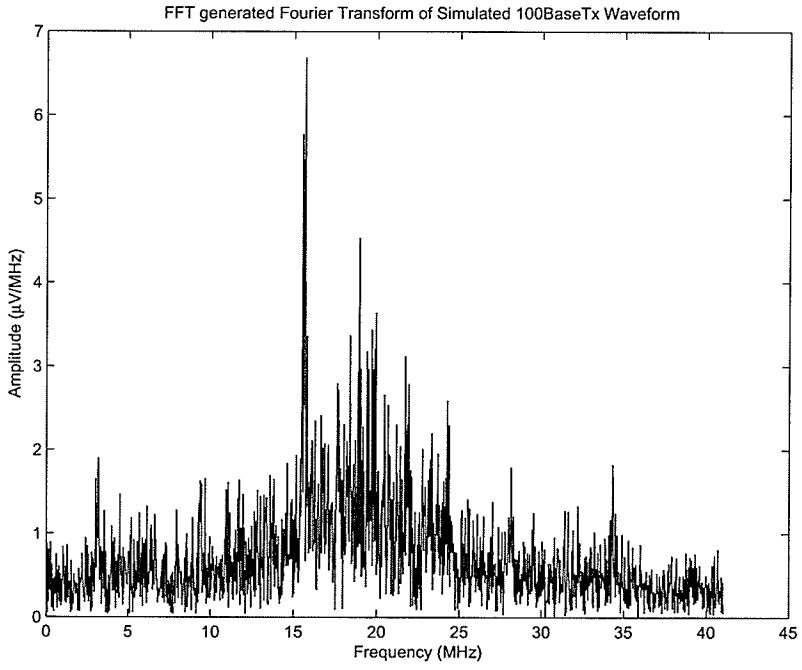

Figure 2-7. FFT of simulated 100BaseTX bitstream

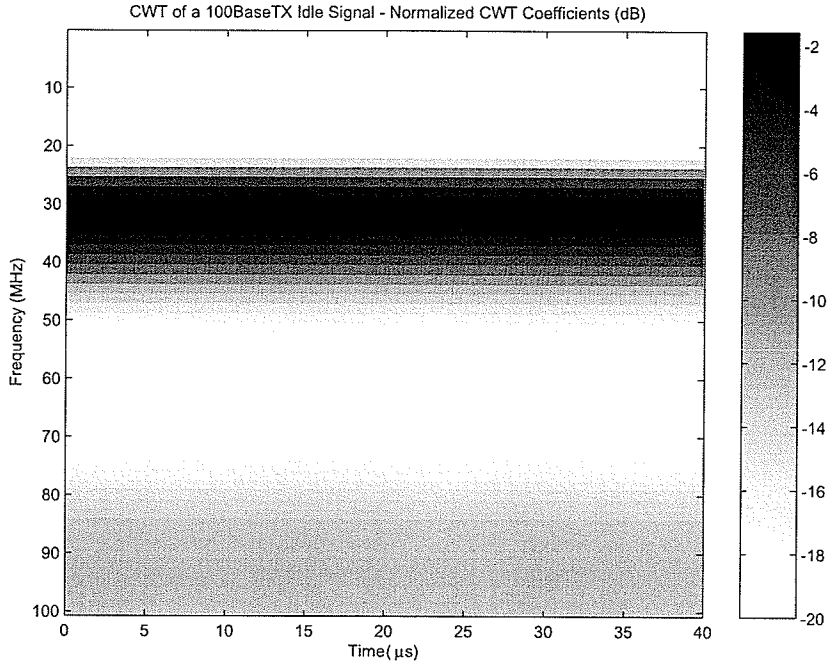

Figure 2-8. CWT of 100BaseTX simulated idle signal

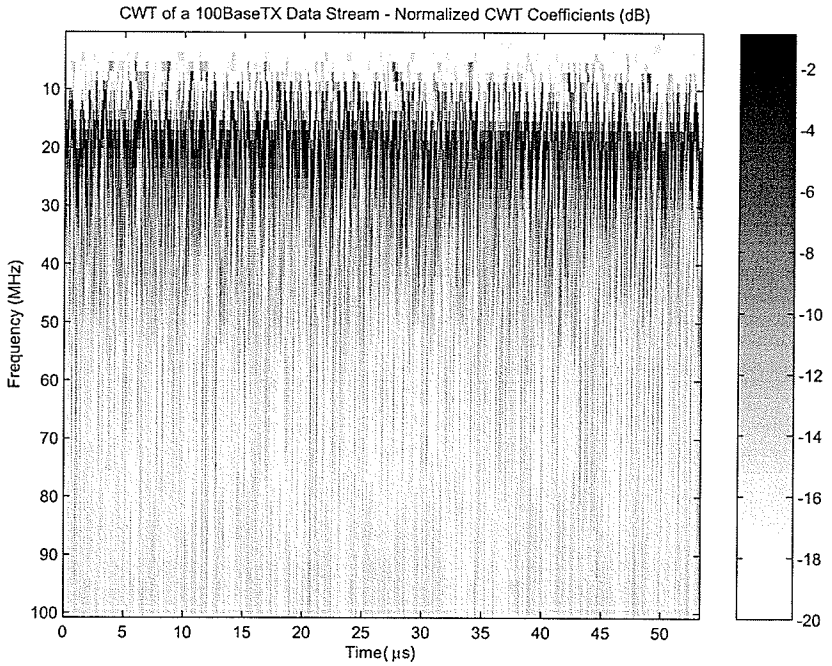

Figure 2-9. CWT of 100BaseTX simulated bitstream

2.4 EXPERIMENTAL SETUP

The experimental system consists of the following major parts: a test network consisting of a server and a client PC (communicating point-to-point via Ethernet for which only the interconnecting Ethernet cable is radiated); an electromagnetic interference generating system consisting of a GTEM cell (wherein the radiation of the cable takes place), a signal generator and amplifier both programmable by the control PC over the General Purpose Interface Bus (GPIB); an interference measurement system consisting of an EMI receiver, two oscilloscopes and high impedance probes; and lastly, data communication throughput monitoring software (running on a control PC). The general setup is shown in Fig. 2-10.

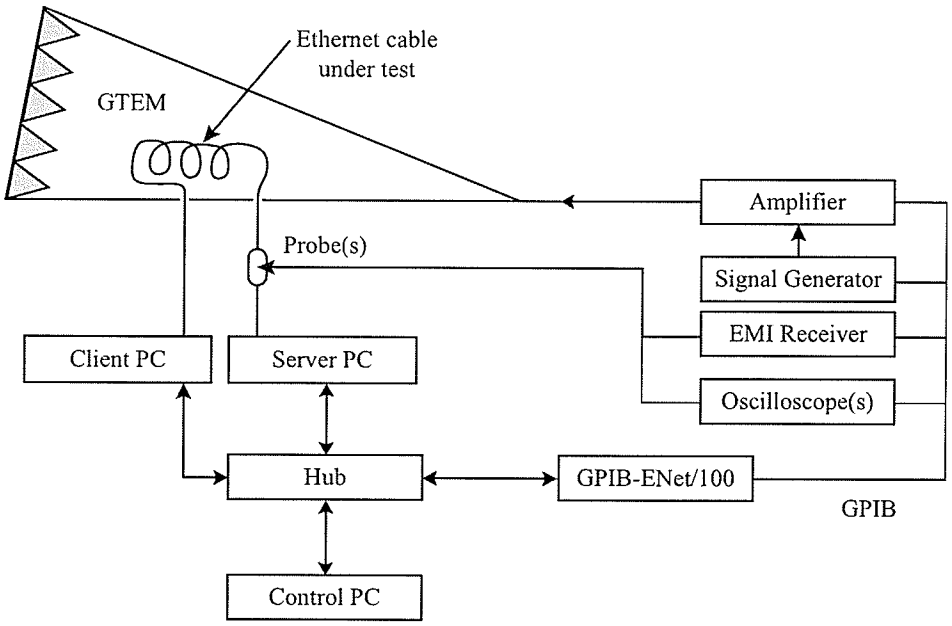

Figure 2-10. Experimental setup

2.5 THE TEST NETWORKS

For conducting experiments, two test networks were selected: Network A and Network B. Network A, consists of two Pentium III - 667 MHz computers running the Linux operating system forming the client and server of a point-to-point Ethernet transfer

link while Network B, consists of two Pentium II - 266 MHz computers, once again running Linux. Linux, without graphical user interface, was installed on the client/server computers in order to reduce any transfer fluctuations that might be caused by maintaining a graphical user interface on these machines. For Network A, the client and server computers each had three NIC cards installed: one pair was used for the non-radiated connection to the experiment control computer, and the remaining two pairs for introducing variation in the hardware technology used to implement the communications. For Network B, the client and server computers each had two NIC cards installed, one each for the non-radiated and radiated connections. In total, three different commercial brands of NIC cards were used for communicating over the transfer link: two AT-2500Tx models and one 3Com model.

2.6 NETWORK INTERFACE CARDS

The three types of network cards used in all experiments are listed in Table 2-3. Technical information for both the AT-2500Tx (V2 and V3) and 3Com cards are available as online documentation published by the manufacturers. All three of these NICs are Peripheral Component Interconnect (PCI) Bus based cards, compatible with all PCI supported motherboards. They all support half and full-duplex operation and both function, from a transmit and receive point of view in the same manner. The purpose for selecting these three specific network cards, with associated chipsets, is simply based on their availability in the commercial market. The Real-Tek RTL-8139 chipsets are common to nearly all commercially available 100BaseTX network cards in the market today. While the most current versions of the RTL-8139 chipsets are the 8139c and 8139d they are functionally the same as the 8139a and 8139b used in the experiments.

Table 2-3. The Network Interface Cards

NIC	Chipset used	Relevant NIC Specifications
Allied Telesyn AT-2500Tx V2	Real-Tek RTL8139a	50 MHz Xtal converted to 25 MHz chip clock 3.3V supplies with 5V tolerant I/O Tx takes 5 bits parallel at 25 MHz and serializes to 125 MHz Rx uses a PLL to extract 125 MHz clock and converts incoming serial bits to 5 bit parallel at 25 MHz
Allied Telesyn AT-2500Tx V3	Real-Tek RTL8139b	25 MHz Xtal and chip clock 3.3V supplies with 5V tolerant I/O Tx takes 5 bits parallel at 25 MHz and serializes them 125 MHz Rx uses a PLL to extract 125MHz clock and converts to parallel.
3Com 3C905C-Tx-M Etherlink	3Com 920Br05	25 MHz Xtal 25 Mhz internal clock (assumed) 3.3V supplies with 5V tolerant I/O (assumed) Similar transmission and reception (assumed)

2.7 THE ETHERNET CABLE

Two lengths of CAT-5 Ethernet cable were used as the cable under test: 30 metres (100 ft.) or 14 metres (46 ft.).

2.8 DIFFERENTIAL-MODE INTERFERENCE GENERATION

As previously discussed, in order to generate interference possible of being classified as HIPDI, it is necessary to generate differential-mode power on the data-pair of the Ethernet cable. Moreover, the radiation should be covert and therefore remote radiation of the cable is considered ideal. Although simply injecting differential-mode interference directly onto the cable would eliminate the problem of coupling energy to a twisted-pair, this technique is not as revealing because single point injection may produce a less applicable effect than distributive injection by means of radiation. Therefore, in all

tests performed, the cable was radiated using a GTEM cell. This required that any interference resulting in no throughput reduction be checked to ensure that the interference was truly non-HIPDI rather than interference for which little or no coupling to the cable was attained.

The RF interference generation system consists of a control computer, connected via an Ethernet connection to a National Instruments GPIB-ENet/100 Ethernet hub. The control PC is used to control a Rohde and Schwarz 5 kHz – 3 GHz signal generator (model number SMT 03), and a Kalmus 10 kHz – 1 GHz, 100 W amplifier. The interference signal was taken from the signal generator, run through the amplifier and into the GTEM cell. The forward power from the amplifier was monitored over the GPIB. The gain of the amplifier could also be set over the GPIB but it was more accurate and efficient to keep the amplifier gain constant and vary the power using the signal generator output power.

Two types of simple interference signals were used in all tests; continuous wave (CW) and amplitude modulation (AM). The AM modulation was set to 100% depth using a 15 kHz square wave. This choice was based on preliminary test results that showed data-rate degradation to be nearly invariant to the selected AM frequency. For both CW and AM signals, discrete carrier frequencies from 1 MHz to 100 MHz (in 1 MHz increments) were selected.

2.9 THE NETWORK SOFTWARE

Each of the server and client computers were equipped with server and client UDP software programmed in Java. Each side of the software (server and client) consists of three separate parallel processes (threads). These threads are responsible for: 1) sending/ receiving UDP datagrams; 2) monitoring the UDP send/receive rate; and 3) monitoring incoming configuration commands from the control computer via a TCP connection. The actual UDP data is configurable in content and length. Each UDP packet was selected to be a set of random data (the same random data for each packet). Due to the overhead in the

java programs themselves (thread creation and packet monitoring) a programmed inter-packet delay was set such that the transfer and receive rates were equal and maximum in the absence of interference.

In order to control the test equipment (source, amplifier, and EMI receiver) from the control computer, two executable programs were developed in C++; one for writing to and one for reading from the GPIB bus. These programs were compiled into executables such that they could be integrated into Matlab along with the Java UDP software. In this manner the experiments were completely automated.

2.10 EXPERIMENTAL PROCEDURES

Two experimental procedures were performed in order to fully expose possible HIPDI. The first set of experiments was performed on Network A and the second on Network B, and are denoted as Experiments A and Experiments B respectively. They are described in the following sections.

2.10.1 Experiments A

In these experiments, the Ethernet cable was selected as either 30 metres or 14 metres in length, which will be simply referred to as long and short respectively. The cable was randomly oriented in the GTEM cell and attached to the client and server PCs. For Experiments A, the portion of the cable outside of the cell was left unshielded and no attempt was made to reduce the common-mode component of the coupled interference.

The GTEM cell (EMCO GTEM, model 5317) was used to expose the cable to the interference and to isolate the rest of the network. The leakage from the GTEM cell into the laboratory room was measured to be minimal over the frequency range of interest (although a small amount of leakage was unavoidable because of the way the cable was fed through the GTEM cell). The operation of the computers was not affected by this leakage energy.

For Experiments A, the actual differential-mode voltage induced on the cable was measured during communication using a standard high impedance probe (Tektronix P2100) connected to the server side of the Ethernet cable, and a Hewlett-Packard 9 kHz – 6.5 GHz EMI Receiver/Spectrum Analyzer (model number 8546A). The receiver was controlled remotely through the National Instruments GPIB-ENet/100 hub. A two-inch section of the Ethernet cable's protective jacket was removed approximately six inches from where it connected to the Server in order to attach the probe across the data pair. The probe used did not posses a flat magnitude transfer function, so a calibration test was performed on the probe and connecting cable. This calibration procedure involved measurement of the attenuation factors of the probe connected by 7 m of LMR400 Coaxial cable and is described in Appendix A.

Each Experiment of type A consisted of four *tests*. Each test used an interference signal type (CW or AM) over the frequency range 1-100 MHz, where the radiation power level was adjusted in order to achieve the desired coupled power level on the data-pair (as measured using the EMI receiver and probe). The desired power levels on the data-pair were selected as -20, -15, -10 and -5 dBm.

It was found that taking measurements using the EMI receiver and probe in this way did not affect data throughput in the absence of interference and was therefore assumed to have no affect on data throughput in the presence of radiation (even though an unbalanced probe was being used). Unfortunately, the high-impedance probe as used in Experiments A, does not give an accurate measurement of the differential-mode interference induced onto the cable because: 1) the Ethernet cable was left unshielded and the large common-mode current induced on the cable inductively coupled to the probe; and 2) the probe used was unbalanced on a balanced pair. While results of these experiments do not accurately show the amount of power required to produce throughput degradation, they do show frequencies at which reductions in throughput are possible. Finally, as these experiments aim to achieve a set power level on the cable, they somewhat compensate for variations in coupling over frequency.

In all tests, UDP packets of 200 bytes of random data were continually transmitted from the server to the client. The resulting bit-rate was roughly 2800 packets per second in the absence of interference. This rate was established by using the inter-packet delay to ensure that the server transfer rate and the client receive rate were equal.

2.10.2 Experiments B

For Experiments of type B, the Ethernet cable was selected as 14 metres in length. In an attempt to limit the common-mode coupling and to increase the differential-mode coupling, the cable was oriented parallel to the septum of the cell as shown in Fig. 2-11.

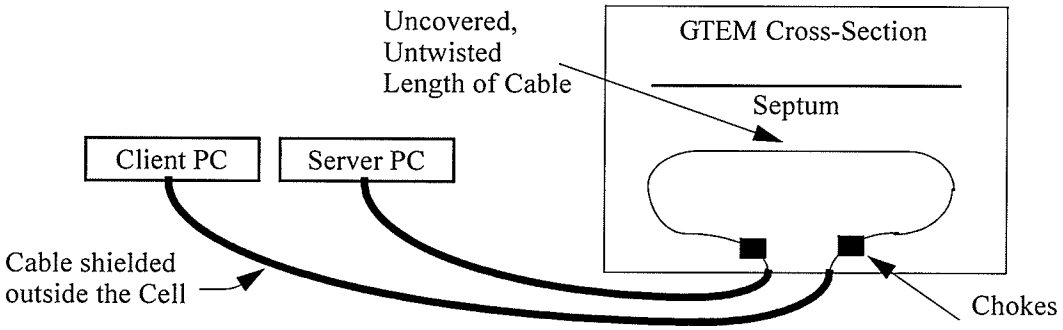

Figure 2-11. Experiment B cable orientation

Approximately 2 m of the cable covering, was removed and the data-pair was untwisted and separated by roughly 5 mm in order to maximize the amount of differential-mode coupled into the cable. Although untwisting and separating the data-pair alters its impedance, the physical change was found to have no affect on throughput rates in the absence of radiation. For these experiments, the portion of the cable outside of the cell was shielded with aluminum foil and grounded to both the GTEM cell and the client or server

PC. This was done in order to reduce the common-mode radiation coupled to the probe outside of the cell. In addition, common-mode chokes were used inside the cell in order to further minimize the amount of common-mode propagated on the cable.

A UDP packet size of 20 bytes was selected resulting in roughly 1000 packets per second. Notably, the smaller packet size was selected in order to increase the number of packets per second since the computers used in these experiments were significantly slower than those of Experiments A.

Each experiment of type B consisted of ten tests. Each test selected a single interference signal type (CW or AM) over the frequency range 1-100 MHz using CW radiation power of 10, 20, 30....100 W. No probing was performed during the tests. In the absence of transmission, an oscilloscope was used to measure the differential- and common-mode voltage on the data-pair at frequencies of interest. The differential voltage was measured using two high-impedance probes, one for each of the data wires. The probe cords were twisted together in order to minimize any extraneous field pick-up formed by the loop between the probe cords. The common-mode voltage was measured by using a single high-impedance probe from one of the data-lines to the ground of the computer case.

2.11 TEST METHODOLOGY

The standard test procedure for all types of experiments is shown below (steps A denote experiments A while steps B denote experiments B):

1. A UDP transfer was initiated, the data being constant throughout each experiment.
2. Prior to radiation, a baseline receive rate was measured through the cable under test.

3A. For each test a level of power was chosen for the measured intentional interference on the Ethernet cable (using the probe and EMI receiver as described above): -20, -15, -10 or -5 dBm.

3B. For each test a power level was chosen as the power input into the GTEM cell (forward power measured on the amplifier): 10, 20, 30 ... 100 W.

4. The desired radiation type, CW or AM, was chosen.

5. The radiation was turned on.

6A. At each frequency the signal generator source power was increased in 1 dB steps from −50 dBm until the desired power level on the cable under test was measured. For certain frequencies, the desired power level was not achievable because the coupling to the cable was too low and sufficient power was not available from the amplifier.

6B. The signal generator and amplifier were set to achieve the desired power level.

7A. Once the desired power was established, the receive data-rate as a percentage of the baseline rate was measured and stored along with the signal generator source power, frequency and the achieved twisted-pair differential-mode power level.

7B. The receive data-rate as percentage of the baseline rate was measured and stored.

8B. The data transfer was terminated and the common-mode and differential-mode levels on the data-pair were measured using the oscilloscope.

2.12 NETWORK HARDWARE CONFIGURATION

For all experiments the NIC card pairs (server and client) are listed in Table 2-4. Note that only in pair A are the server and client NIC cards different. Subsequently, the NIC card configuration will be differentiated by their NIC pair label A B or C.

Table 2-4. NIC Pairs Used

NIC Pair	Server NIC	Server Chipset	Client NIC	Client Chipset
A	AT-2500Tx V3	RTL-8139b	AT-2500Tx V2	RTL-8139a
B	AT-2500Tx V3	RTL-8139b	AT-2500Tx V3	RTL-8139b
C	3Com 905C-Tx-m	3Com-920BR05	3Com 905C-Tx-m	3Com-920BR05

2.13 SUMMARY OF EXPERIMENTS PERFORMED

Using the general experimental procedure described above, experiments of type A and B were performed. The details for each experiment of type A are shown in Table 2-5, while the details of experiments of type B are outlined in Table 2-6.

Table 2-5. Experiments A

Experiment Number	Modulation Type	Network Configuration	Cable Length (m)
1	CW	A	30
2	CW	A	14
3	CW	B	30
4	CW	B	14
5	CW	C	30
6	CW	C	14
7	AM	A	30
8	AM	A	14
9	AM	B	30
10	AM	B	14
11	AM	C	30
12	AM	C	14

Table 2-6. Type B Experiments

Experiment Number	Modulation Type	Network Configuration	Cable Length (m)
B1	CW	B	14
B2	AM	B	14

2.14 EXPERIMENTAL RESULTS AND ANALYSIS

In order to analyze the experimental results the data is presented in a series of contour plots. In each plot, the percentage throughput is shown as both a function of frequency and either the differential-mode power level on the Ethernet cable (in the case of A-type experiments) or the radiation power level (in the case of B-type experiments). For example, Fig. 2-12 shows the contour plot obtained for Experiment A1. The dark regions of the plot show areas where less than 10% throughput resulted. For example, from 10 to 18 MHz, communication has been completely disrupted with -10 dBm (100 mW) of coupled power. White regions show complete throughput (i.e., no degradation). The results for both types of experiments will now be discussed.

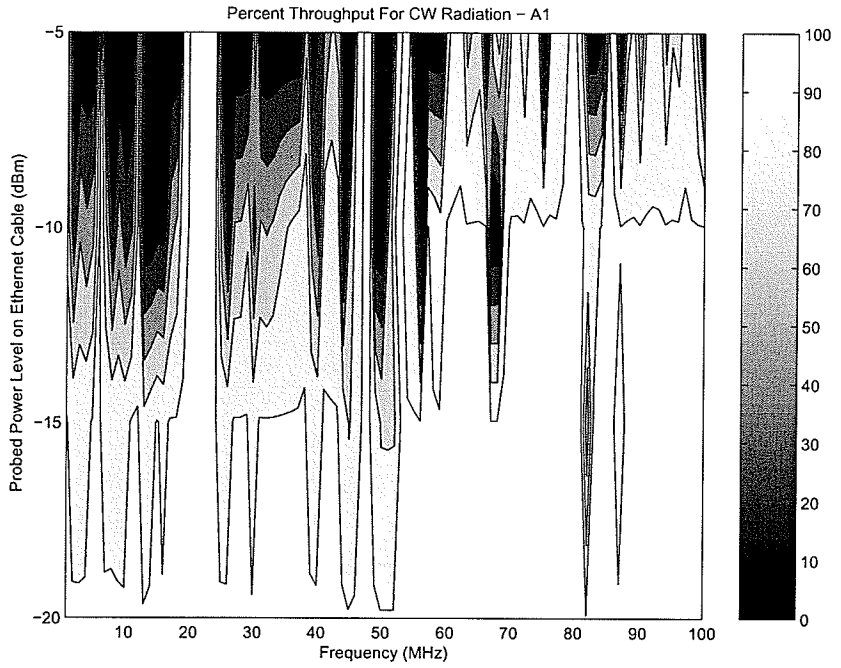

Figure 2-12. Experiment A1 - CW radiation of Network A / NIC pair A / long cable

2.14.1 Experiment A Results

As seen from Fig. 2-12, it is possible to disrupt communication completely under some interference signals, while others seem to have no affect on throughput. Of immediate interest is the cause for such immunity regions. From analysis of the actual interference power measured on the twisted-pair, it was found that some of the immunity regions correspond directly to frequency bands in which it was not possible to couple sufficient energy. The 20 MHz region of Fig. 2-12 was determined to be such a coupling null.

Comparing the results of Experiments A1 and A2, (the latter shown in Fig. 2-13 and differing only in cable length), it is seen that the contours are quite different. Above 80 MHz, for instance, it was difficult to achieve any degradation using CW with the short cable whereas with long cable significant degradation regions are visible. It was found that in this frequency band there were no coupling nulls. At this time, the only explanation is that the onset of disruption occurs suddenly when the power level reaches –5 dBm on the twisted-pair and therefore the discrepancies in disruption between the two cable lengths is caused by the adopted probing technique which does not sufficiently differentiate between the common- and differential-mode energy coupled to the cable.

More prominent degradation regions were obtained for lower frequencies. A comparison of both experiments below 80 MHz shows that many of the coupling nulls of Experiment A1 (20, 48 and 52 MHz) are not present in the short cable experiment. In contrast, new nulls are apparent for Experiment A2 that were not visible in Experiment A1. Of course, it is well known that changing the cable length will change the radiative coupling and so these results are expected.

A brief comparison of the results of Experiments A1 and A2 indicates that CW radiation in the ranges of 10-50 MHz, 60-70 MHz and 80-100 MHz may be possible HIPDI.

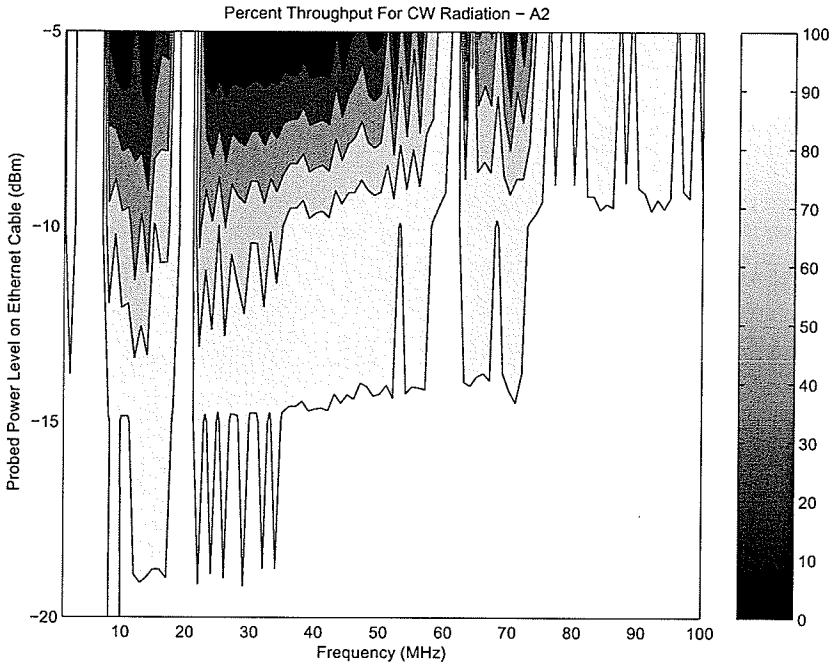

Figure 2-13. Experiment A2 - CW radiation of Network A / NIC pair A / short cable

When compared with Experiment A6, shown in Fig. 2-14, it is revealed that varying the NIC pair from A to C, over the short cable, changes the degradation contour significantly. Specifically, in the 10 to 18 MHz region, -5 dBm is now required to produce severe degradation compared with the -10 dBm required for NIC pair A. There are two possible explanations. First, although care was taken when changing the NIC pairs, the cable orientation may have been disturbed slightly within the cell causing a significant change in the field coupling. Second, it is simply possible that some of the regions of degradation are hardware dependent. Although the CWT of the 100BaseTX idle signal shown in Fig. 2-8 shows -8 to -10 dB of normalized CWT coefficient in the frequency range of 80-100 MHz (originally assumed to be significant spectral components), it is apparent that, at least for CW, this frequency range may not have a sufficient aperture for HIPDI. Although not shown, results similar to Experiment A6 were obtained for NIC pair B (Experiment A4) and, as expected, varying the cable length made little difference in the

overall degradation contour. These results simply implies the existence of hardware dependencies. The results change when the effective bandwidth of the interference radiation is increased as a result of AM radiation.

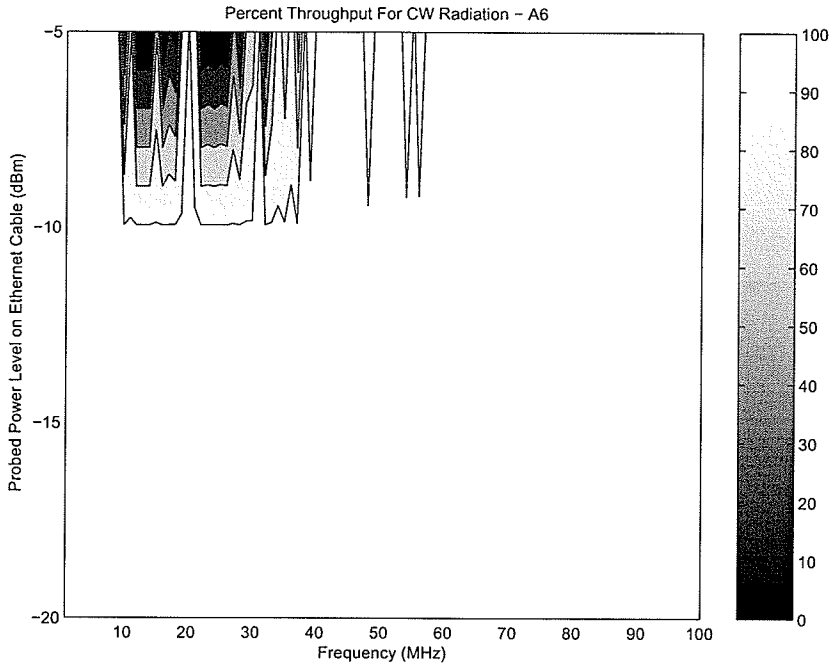

Figure 2-14. Experiment A6 - CW radiation of Network A / NIC pair C / short cable

When AM interference is considered, much deeper and broader degradation regions are displayed. For example, Fig. 2-15 shows the results of Experiment A12. Here, the short cable was used with NIC pair C as in Experiment 6 of Fig. 2-14. It is apparent that the same frequency regions where CW interference showed degradation, AM interference shows similar degradation at a lower power level. Specifically, the theorized 10-50 MHz range (except for a coupling null near 20 MHz) is such a region. AM radiation is suspected to produce better throughput reduction due to its broader spectrum that more closely resembles MLT-3 data than simple CW. As shown in Fig. 2-16 and Fig. 2-17, varying the NIC pair to A and C results in very similar contour plots for AM radiation. For each NIC pair considered, the theorized susceptible frequency ranges of 10-50 MHz and 60-70 MHz are indeed susceptible to AM interference. The susceptibility in the range 80-100 MHz seems to be hardware dependent.

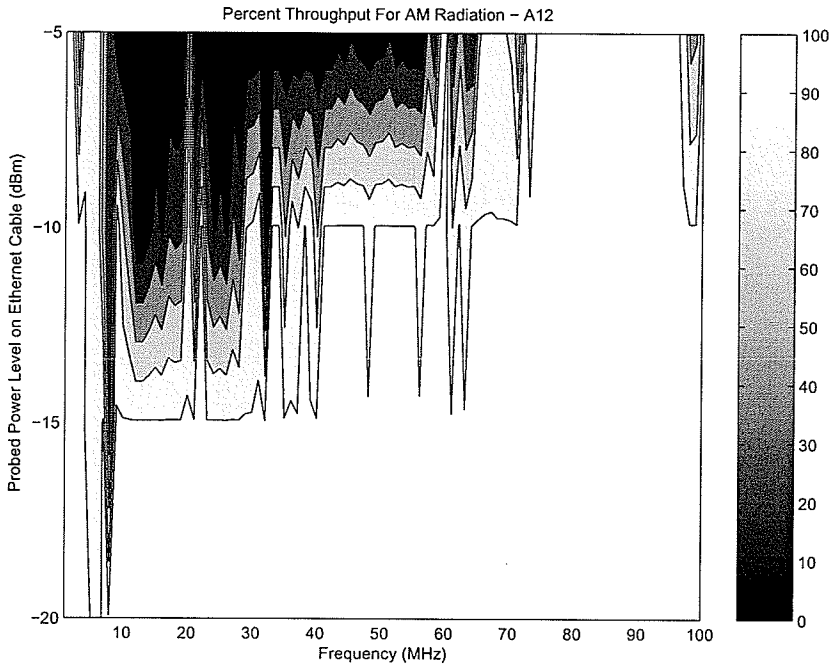

Figure 2-15. Experiment A12 - AM radiation of Network A / NIC pair C / short cable

It should be noted that for both CW and AM interference, disruption occurred only to the protocol and perhaps to the NIC card, but was undetectable in the operation of the server and client computers themselves. That is to say, all non-network related programs running on these computers always executed normally, further proof that the GTEM isolation of the interference was effective.

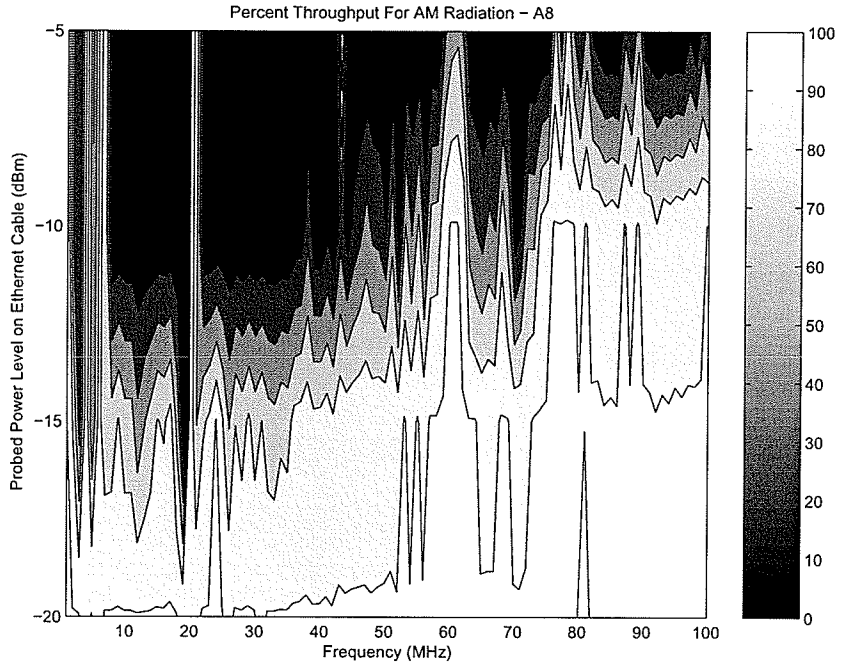

Figure 2-16. Experiment A8 - AM radiation of Network A / NIC pair A/ short cable

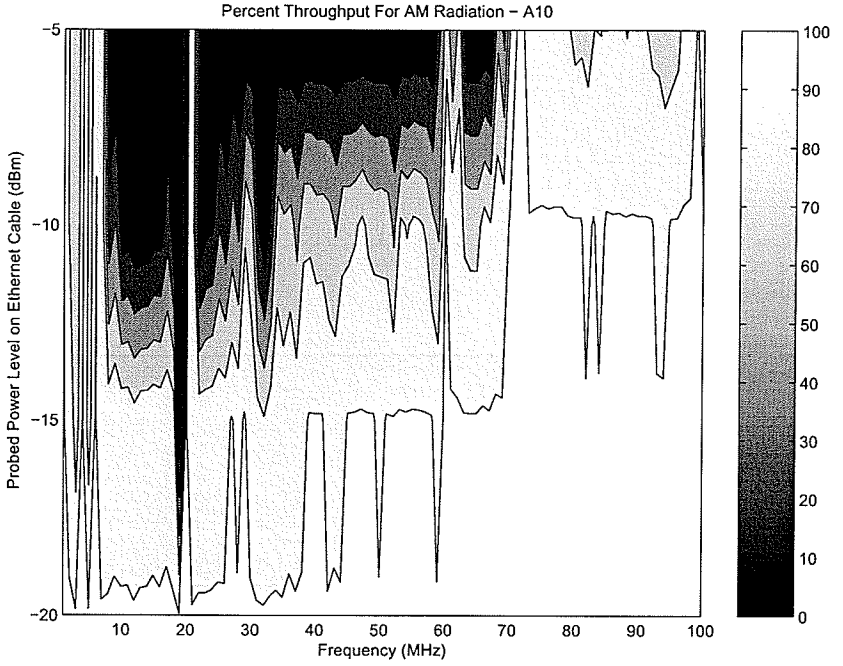

Figure 2-17. Experiment A10 - AM radiation of Network A / NIC pair B / short cable

2.14.2 Experiment B Results

As the probing method used for Experiments A lacks in its ability to differentiate between common- and differential-mode interference, Experiments B were performed in order to properly distinguish between the amount of common- and differential-mode interference generated by the radiation. The results of Experiment B1 with 20 W of forward power and 60 W of forward power (respectively approximately 30 and 55 V/m field strength at the cable) are shown in Fig. 2-18 and Fig. 2-19. Experiment B1 corresponds to CW exposure from 1 MHz to 100 MHz at 10, 20, 30 ... 100 W.

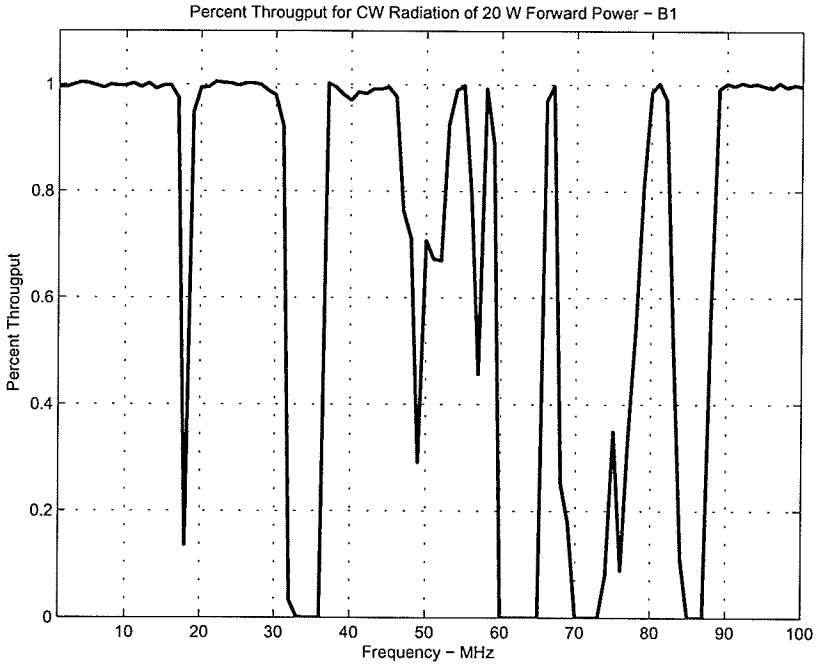

Figure 2-18. Experiment B1 - CW radiation of Network B at 20W forward power

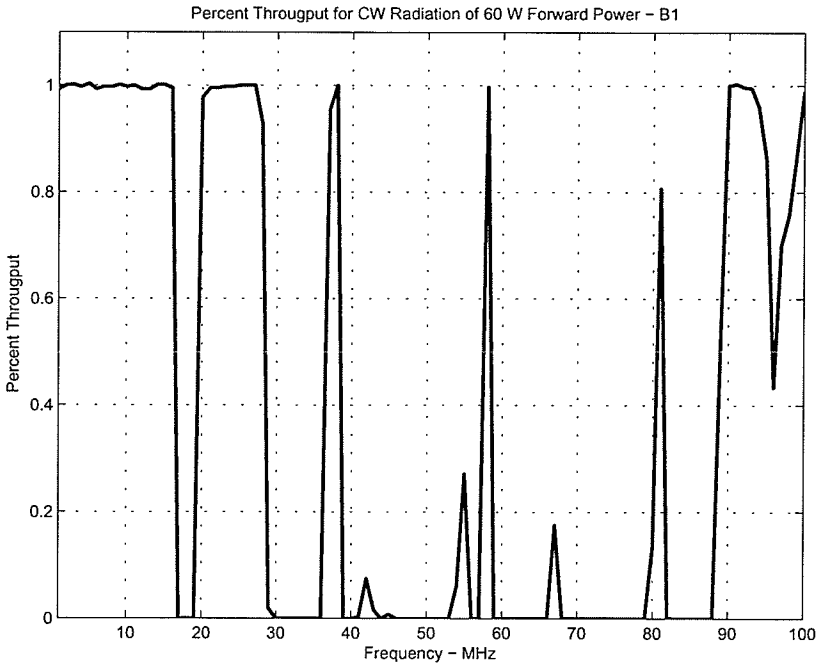

Figure 2-19. Experiment B1 - CW radiation of Network B at 60W forward power

From the contour plots, significant degradation is found even at low power levels. The lack of throughput reduction up to 17 Mhz was found to be caused by a large coupling null. When compared with the results of Experiments A in which little disruption occurred above 60 MHz, we see that for Experiments B disruption is possible up to 100 MHz. Of importance is that both 33 MHz and 65 MHz (near the idle signal and its second harmonic) are capable of disrupting throughput at 20 W of forward power. In this section, only CW results are shown. The effects of AM radiation are similar to those presented for Experiments A.

From a thorough analysis of the obtained contour plots important results were obtained. Table 2-7 and Table 2-8 summarize the measured differential- and common-mode voltage levels on the line at frequencies of interest. In Table 2-7, frequencies where disruption occurred are summarized (the lowest power level at a given frequency represents the minimum required power for throughput reduction). Table 2-8 shows frequencies where no disruption was achieved up to 100 W of forward power (the coupling null up to 17 MHz has been omitted).

Table 2-7. Experiment B1 Susceptible Frequencies

Frequency (MHz)	Radiation Power (W)	Measured Common-Mode (V pk-pk)	Measured Differential-Mode (mV pk-pk)	% Throughput
18	20	4.8	339.7	0
33	10	2.56	339.7	0
54	30 40 50 60	2.08 2.40 2.68 2.96	299.7 320.0 320.9 533.8	95 90 70 0
65	10	0.48	142.2	0
67	40 50 60	1.52 1.72 1.92	317.8 327.5 344.7	81 49 0
72	10	0.14	302.5	0
81	60 100	0.77 1.02	360.6 405.9	90 0
86	10	0.50	184.1	0
96	50 60 100	0.41 0.41 0.54	285.0 329.4 367.8	95 70 0

Table 2-8. Experiment B1 Insusceptible Frequencies

Frequency (MHz)	Radiation Power (W)	Measured Common-Mode (V pk-pk)	Measured Differential-Mode (mV pk-pk)	% Throughput
24	100	5.20	319.7	100
38	100	9.28	939.7	100
58	100	4.48	263.4	100
92	100	0.89	799.7	100

The frequencies of 33, 65, 72 and 86 MHz correspond to total failure of throughput at the lowest test power of 10 W. The question concerning if throughput reduction is a result of differential-mode interference is revealed by Table 2-7 and Table 2-8. The maximum common- mode voltage of 2.56 V pk-pk (all subsequent voltage references are assumed to be pk-pk values) and the minimum level was found to be less than 0.5 V.

The remaining frequencies of Table 2-7 (18, 54, 76, 81, 96) correspond to throughput reduction above a certain radiation level and 100% throughput below that radiation level. In nearly all cases, throughput reduction appears to begin at roughly 300 mV while total throughput failure occurs at around 340 mV. The only exception was for 65 MHz where only 142 mV of differential-mode was required. In these cases, the common-mode does not exceed 4.8 V and was typically 1-2 V.

From the results of Table 2-8 it is possible to make further inferences. Each of the four frequencies resulted in no throughput reduction up to 100 W. It was found that the frequencies 24 and 58 MHz were not capable of generating 340 mV of differential-mode which seems to be required for most cases of throughput disruption. Most importantly, at 38 MHz, the common mode was above 9 V (the highest at any of the selected test frequencies), and no disruption occurred. This is an indication that it is indeed the differential-mode protocol interference causing disruption. Finally, at 38 and 92 MHz, more than 700 mV of differential power were on the line and no failure occurred. For 92 MHz the results are consistent with Experiments A1, A2 and A6 which indicated that interference in this frequency range may not have a sufficient aperture for HIPDI. At 38 MHz, degradation was achievable when AM radiation was selected, suggesting (as did the results of Experiments A) that AM interference is a more likely HIPDI candidate.

2.15 Summary of HIPDI and Hardware Independence

In this chapter the concept of HIPDI has been introduced. The existence of a HIPDI would pose a severe threat, if implemented as intentional EMI, to the corresponding protocol for which it was designed as little can be done to guard against it or to detect it. Experimental results suggest that low-level, narrowband differential-mode

voltage levels on a 100BaseTX Ethernet twisted-pair can seriously degrade network throughput and that these voltage levels are achievable using simple CW and AM signals in the ranges of 10-50 and 60-70 MHz. Specifically, most test indicate protocol susceptible to frequencies near the second harmonic of the idle signal at 62.5 MHz and near the fundamental idle frequency of 31.25 MHz.

The question arises as to whether or not the degradation obtained is truly hardware independent. Obviously, this research has not exhausted all possible hardware configurations. Therefore there is no formal proof (if such a proof exists) that the throughput reductions achieved were independent of hardware implementation. It is possible however, to support the hardware independent claim. For example, Fig. 2-20 shows the superposition of a 65 MHz sine-wave, with a randomly selected phase over a simulated MLT-3 bitstream. The sine-wave magnitude was selected to be 150 mV pk-pk to approximate the results obtained from Experiment B1. It is inconclusive if this superposition is sufficient disruption of the existing waveform, or if the hardware interpreter may consider it to be sufficiently data-like to cause collisions at the Ethernet layer. At higher power-levels however, the waveform becomes more and more distorted. Fig. 2-21 and Fig. 2-22 show the superposition of a 31.25 MHz CW signal over a simulated bitstream (the amplitude selected as 300 mV pk-pk and 600 mV pk-pk). Especially in the 600 mV case, it seems as though the existing waveform is completely destroyed which could surely be interpreted as a collision by the NIC card.

From these results it seems appropriate to conclude that although the question of hardware independence is debatable, there is strong experimental results that support the conclusion that HIPDI for 100BaseTX Ethernet exists. Every hardware configuration tested so far has failed under the interference parameterized by the hardware aperture.

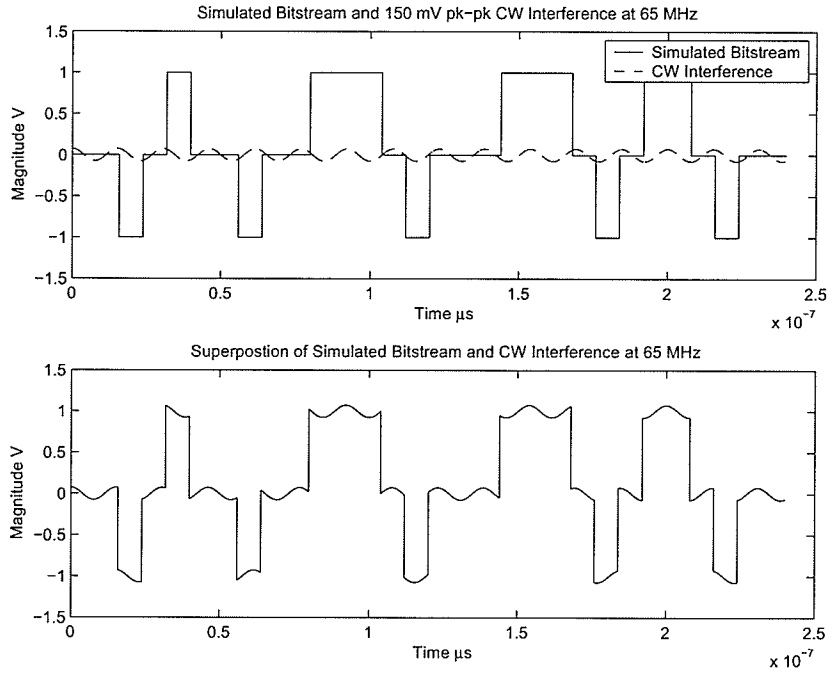

Figure 2-20. Superposition of MLT-3 with a 65 MHz sinusoid - 150 mV pk-pk

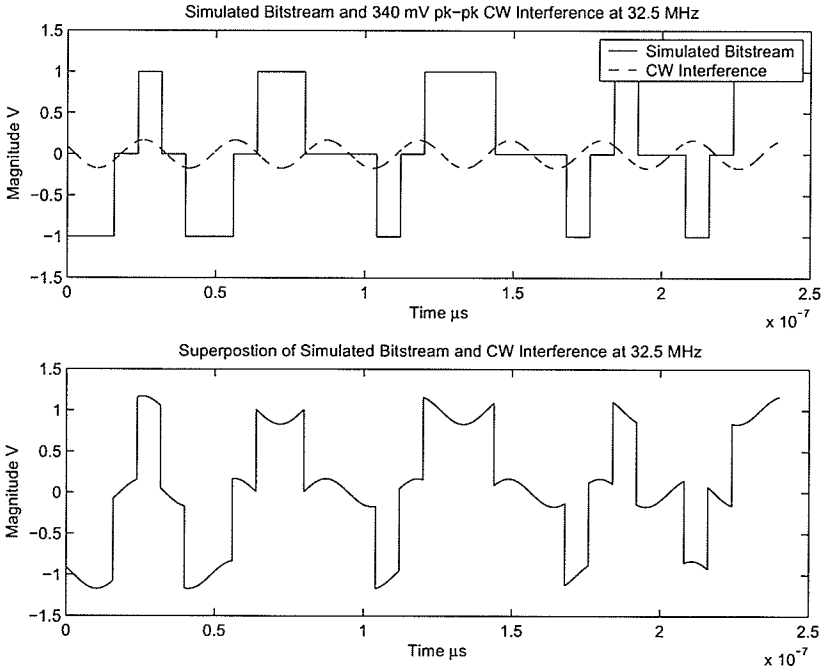

Figure 2-21. Superposition of MLT-3 with a 31.25 MHz sinusoid - 300 mV pk-pk

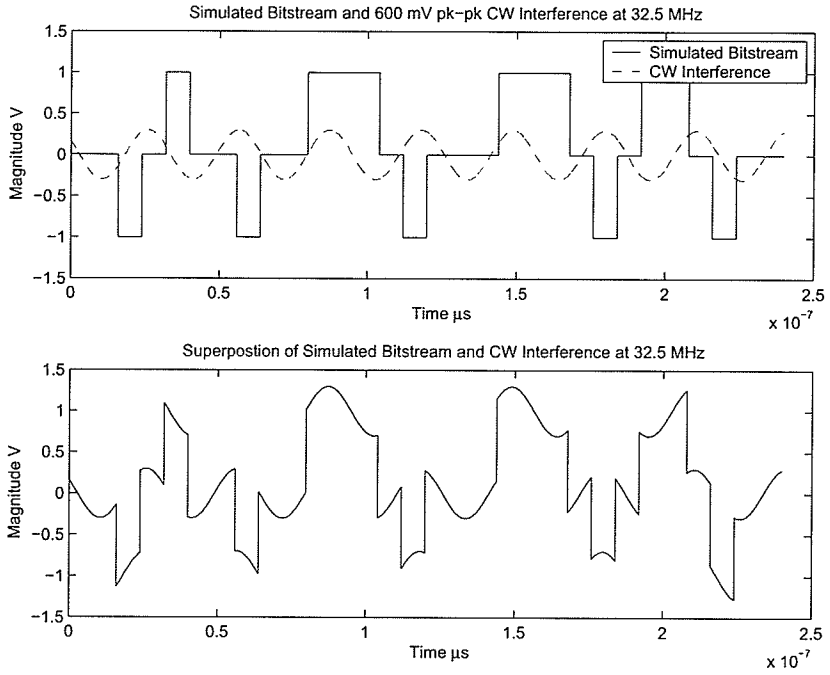

Figure 2-22. Superposition of MLT-3 with a 31.25 MHz sinusoid - 600 mV pk-pk

CHAPTER 3. PLANE WAVE COUPLING TO A UNIFORM TRANSMISSION LINE

In this chapter, as a result of the work performed in the investigation of HIPDI for 100BaseTX Ethernet, the BLT solution to the coupling of an electromagnetic plane wave to a uniform transmission line is presented.

3.1 MOTIVATION

The research conducted on HIPDI contained a fundamental assumption. For 100BaseTX Ethernet, a wired medium, the problem of coupling energy to the CAT-5 cable was conveniently avoided. Instead, analysis focused on classifying interference as HIPDI if sufficient coupling was achievable (maintaining that the coupling problem had been sufficiently discussed in the literature [6]). Unfortunately, the majority of past research considers only the case of a deterministic transmission line and interference. In many practical cases, (for example the random orientation of the CAT-5 cable inside the GTEM cell for Experiments A of the previous chapter), a probability density function of the voltage or current coupled to the transmission line terminations is necessary. The source must be capable of generating sufficient differential-mode on the twisted-pair in order to disrupt communication, and the common-mode voltage induced on the pair should be minimal in order to prevent possible hardware failure or hardware dependent common-mode to differential-mode conversion.

A thorough literature review was performed in order to determine if a solution to the random coupling problem was available. The search found no previous research in which this problem had been attempted. In fact, the only twisted-pair research of interest was found in [12]-[14]. In [12] electromagnetic pulse (EMP) coupling to a twisted pair is discussed where the source of excitation as well as the pair geometry is deterministic. In

[13] the radiated field from a twisted pair is analyzed, once again given a deterministic cable geometry while in [14] the differential- and common-mode coupling of CW radiation to twisted pair is analyzed given deterministic fields and cable geometry (with many assumptions in order to simplify the solution of the resulting electric field integral equations).

As little previous work has been done in the area of stochastic coupling, the problem of statistically evaluating the coupling to a randomly oriented twisted-pair (or even to a uniform twisted pair or a randomly oriented non-twisted transmission-line) proved to be too complicated at this time. Instead, the continuation of this research is ***to determine distributions of the termination voltage and current magnitudes caused by the coupling of time-harmonic stochastic plane waves to a deterministic, lossless, uniform transmission line in free space***. The assumption of plane-wave incidence is a good model for many coupling problems. Specifically, the fields inside a GTEM cell are generally plane and many common antennas produce plane-waves patterns in the far-field.

The random nature of the field to be studied may be inherent in its angle of incidence (although the angle is assumed to be fixed for all time), frequency, magnitude, phase and polarization. As CW interference seems to be a possible HIPDI for 100BaseTX Ethernet, the time-harmonic case is an appropriate choice. To simplify the problem, it is assumed that only the TEM mode of propagation exists. Even though this problem is physically less complicated than coupling to a stochastically defined non-uniform transmission line or to a stochastic twisted-pair, it is a problem of significant merit that has not yet been addressed. In the case of HIPDI, if the CAT-5 cable is sufficiently straight, common-mode coupling to the cable could be determined by modelling the twisted-pair as a single conductor upon which common-mode current flows.

3.2 THE STOCHASTIC COUPLING PROBLEM

The problem of coupling a time-harmonic external electromagnetic field to a single, uniform, two-wire transmission-line of length l and separation d as shown in Fig. 3-1 (taken from [15]) involves the solution of the Telegrapher's Equations (assuming only TEM fields exist on the line) given as:

$$\begin{aligned} \frac{d}{dx}V(x) + ZI(x) &= V_s(x) \\ \frac{d}{dx}I(x) + YV(x) &= I_s(x) \end{aligned} \tag{3.1}$$

where Z and Y respectively represent the total per-unit-length impedance and admittance of the line [15],[16].

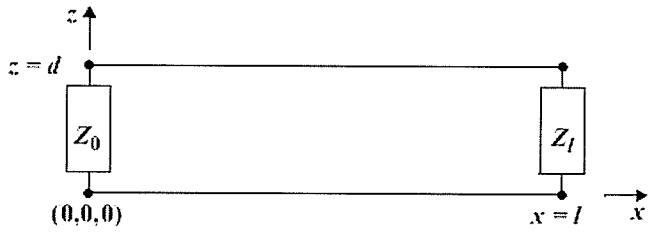

Figure 3-1. Transmission line geometry

The source terms, or forcing functions, $V_s(x)$ and $I_s(x)$ are the per-unit-length series voltage and shunt current occurring on the line due to the impinging electromagnetic radiation. The load terms Z_o and Z_l correspond to the load impedances and specify the boundary conditions of Eq 3.1. The question now arises as to how to solve this problem when $V_s(x)$, $I_s(x)$ and hence $V(x)$ and $I(x)$ are randomly defined.

For the problem under consideration, the forcing functions $V_s(x)$ and $I_s(x)$ of Eq 3.1 are related to the incident electric and magnetic field by the integrals [15]-[16]

$$V_s(x) = -j\omega\mu_o \int_0^d H_y^{inc}(x,z)dz$$
$$I_s(x) = -j\omega C \int_0^d E_z^{inc}(x,z)dz \tag{3.2}$$

and in the case of CW radiation from a fixed source, neither source varies with dimension (time, space or any other) making Eq 3.2 a function of random variables (as opposed to a stochastic process).

A simple technique was found in publications in the field of *stochastic differential equations*. Many books (see for example [17]-[21]) deal with the problem of solving differential equations such as Eq 3.1 when the parameters (coefficients, initial conditions or forcing functions) are random. In the case when randomness is only introduced in the form of random variables, as is the case of Eq 3.2, (and not stochastic processes, a more complicated problem that is the primary focus of most of the literature in this field [17]-[21]), the solution is easily found by first solving the differential equations in the deterministic case and then applying transformations of the solution to encapsulate the inherent randomness of the problem (as will be shown in the remaining chapters of this work). In the next section, a compact, analytic, closed-form *deterministic* solution to the plane-wave coupling problem, known as the BLT solution, is presented in order to numerical generate Monte Carlo densities in Chapter 4.

3.3 THE BLT SOLUTION

Although there exist different ways of solving the deterministic coupling problem of interest, the so-called BLT solution (the acronym stemming from the names of the solution's authors) was selected due to the form of the solution it provides: a compact function of the problems physical parameters [15]. The BLT solution uses both a scattered-field formulation and matrix diagonalization to uncouple the Telegrapher's Equations of Eq 3.1. A complete derivation of the BLT solution can be found in [15] and [16] although the forms of the solutions are different due to a difference in the selected

coordinate system. For convenience, a full development of the BLT solution (closely following that developed in [15] is provided in Appendix B while for conciseness only the solution is presented in this section.

For the x-directed transmission line of Fig. 3-1 and the coordinate system of Fig. 3-2 (taken from [20]) the solution to the near-end $V(0)$ and far end $V(l)$ voltages arising from an impinging plane wave are given by:

$$\begin{bmatrix} V(0) \\ V(l) \end{bmatrix} = \frac{1}{2}\begin{bmatrix} 1+\rho_0 & 0 \\ 0 & 1+\rho_l \end{bmatrix}\begin{bmatrix} -\rho_0 & e^{\gamma l} \\ e^{\gamma l} & -\rho_l \end{bmatrix}^{-1}\begin{bmatrix} S_1 \\ S_2 \end{bmatrix} \tag{3.3}$$

$$\begin{bmatrix} I(0) \\ I(l) \end{bmatrix} = \frac{1}{2Z_c}\begin{bmatrix} 1-\rho_0 & 0 \\ 0 & 1-\rho_l \end{bmatrix}\begin{bmatrix} -\rho_0 & e^{\gamma l} \\ e^{\gamma l} & -\rho_l \end{bmatrix}^{-1}\begin{bmatrix} S_1 \\ S_2 \end{bmatrix} \tag{3.4}$$

where Z_c is the characteristic impedance of the transmission line, ρ_0 and ρ_l are the near-end and far/load-end reflection coefficients determined by Z_c, Z_o and Z_l (the characteristic, near-end and far-end termination impedances) and γ is the complex propagation constant along the transmission line. In Fig. 3-2, unit vectors are denoted as $\hat{\boldsymbol{a}}_\alpha$ where α indicates the appropriate direction. The source terms S_1 and S_2 are given by:

$$\begin{bmatrix} S_1 \\ S_2 \end{bmatrix} = -Ed\begin{bmatrix} \left(\frac{jk\cos\theta(\cos\theta\cos\phi\cos\zeta-\sin\phi\sin\zeta)}{\gamma+jk\sin\theta\cos\phi}+\sin\theta\cos\zeta\right)(e^{(\gamma+jk\sin\theta\cos\phi)l}-1) \\ e^{\gamma l}\left(\frac{jk\cos\theta(\cos\theta\cos\phi\cos\zeta-\sin\phi\sin\zeta)}{\gamma-jk\sin\theta\cos\phi}-\sin\theta\cos\zeta\right)(e^{(-\gamma+jk\sin\theta\cos\phi)l}-1) \end{bmatrix} \tag{3.5}$$

where:

- E is the phasor representation of the impinging field such that $E = |E|\angle E$ with an assumed $j\omega t$ time dependence
- θ, ϕ are the azimuthal angle and the polar angle indicating the source of origin of the field in spherical coordinates as in Fig. 3-2
- ζ is the polarization angle of the incident field as measured from θ to ϕ

- k is the wavenumber of the plane-wave such that $k = \omega/v$ with v being the speed of propagation in the medium and ω being the field's angular frequency.

For the free-space medium under consideration, the velocity is related to the permittivity ε_o and permeability μ_o of the region as

$$v = \frac{1}{\sqrt{(\varepsilon_o \mu_o)}} \tag{3.6}$$

resulting in a velocity of propagation $v = c = 3 \times 10^8$ m/s.

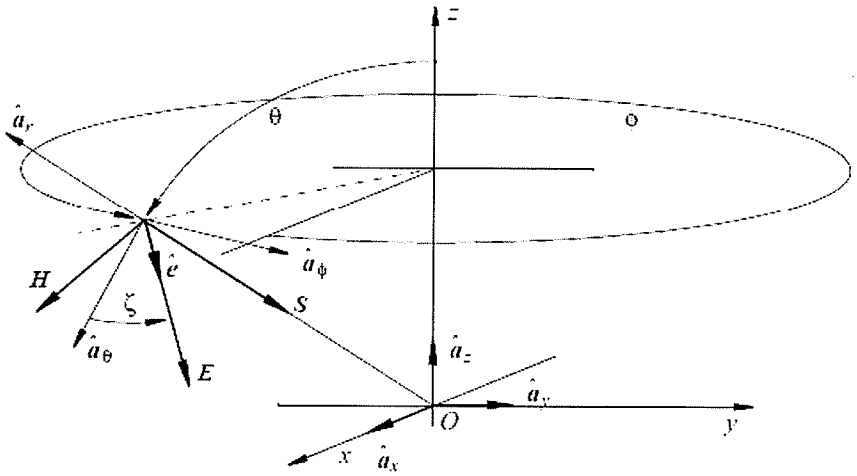

Figure 3-2. Selected coordinate system for the BLT solution

3.4 SIMPLIFICATION OF THE BLT SOLUTION

In order to analyze and efficiently program the BLT solution, it is convenient to simplify Eq 3.3 beginning with substitution of the inverse matrix:

$$\begin{bmatrix} -\rho_0 & e^{\gamma l} \\ e^{\gamma l} & -\rho_l \end{bmatrix}^{-1} = \frac{1}{\rho_0 \rho_l - e^{2\gamma l}} \begin{bmatrix} -\rho_l & -e^{\gamma l} \\ -e^{\gamma l} & -\rho_0 \end{bmatrix} \tag{3.7}$$

giving:

$$\begin{bmatrix} V(0) \\ V(l) \end{bmatrix} = \frac{1}{2(\rho_0\rho_l - e^{2\gamma l})} \begin{bmatrix} 1+\rho_0 & 0 \\ 0 & 1+\rho_l \end{bmatrix} \begin{bmatrix} -\rho_l & -e^{\gamma l} \\ -e^{\gamma l} & -\rho_0 \end{bmatrix} \begin{bmatrix} S_1 \\ S_2 \end{bmatrix} \tag{3.8}$$

Performing the required matrix multiplications yields:

$$\begin{bmatrix} V(0) \\ V(l) \end{bmatrix} = \frac{1}{2(\rho_0\rho_l - e^{2\gamma l})} \begin{bmatrix} (1+\rho_0)(-\rho_l) & (1+\rho_0)(-e^{\gamma l}) \\ (1+\rho_l)(-e^{\gamma l}) & (1+\rho_l)(-\rho_0) \end{bmatrix} \begin{bmatrix} S_1 \\ S_2 \end{bmatrix} \tag{3.9}$$

$$\begin{bmatrix} V(0) \\ V(l) \end{bmatrix} = \frac{1}{2(\rho_0\rho_l - e^{2\gamma l})} \begin{bmatrix} (1+\rho_0)(-\rho_l)S_1 + (1+\rho_0)(-e^{\gamma l})S_2 \\ (1+\rho_l)(-e^{\gamma l})S_1 + (1+\rho_l)(-\rho_0)S_2 \end{bmatrix} \tag{3.10}$$

resulting in an explicit equations for the near- and far-end voltages in terms of the source terms S_1 and S_2. Similarly, the expression for the near-end and far-end currents is obtained from Eq 3.4:

$$\begin{bmatrix} I(0) \\ I(l) \end{bmatrix} = \frac{1}{2Z_c(\rho_0\rho_l - e^{2\gamma l})} \begin{bmatrix} (1-\rho_0)(-\rho_l)S_1 + (1-\rho_0)(-e^{\gamma l})S_2 \\ (1-\rho_l)(-e^{\gamma l})S_1 + (1-\rho_l)(-\rho_0)S_2 \end{bmatrix}. \tag{3.11}$$

3.5 THE BLT SOLUTION FOR LOSSLESS TRANSMISSION LINES

As the problem under consideration is coupling to a lossless transmission line, the complex propagation constant has no attenuation factor and is related directly to the wavenumber:

$$\gamma = jk \tag{3.12}$$

Considering the termination currents, the lossless assumption results in:

$$\begin{bmatrix} I(0) \\ I(l) \end{bmatrix} = \frac{1}{2Z_c(\rho_0\rho_l - e^{2jkl})} \begin{bmatrix} (1-\rho_0)(-\rho_l)S_1 + (1-\rho_0)(-e^{jkl})S_2 \\ (1-\rho_l)(-e^{jkl})S_1 + (1-\rho_l)(-\rho_0)S_2 \end{bmatrix} \tag{3.13}$$

$$\begin{bmatrix} S_1 \\ S_2 \end{bmatrix} = -Ed \begin{bmatrix} \left(\frac{\cos\theta(\cos\theta\cos\phi\cos\zeta - \sin\phi\sin\zeta)}{1+\sin\theta\cos\phi} + \sin\theta\cos\zeta\right)(e^{(1+\sin\theta\cos\phi)jkl} - 1) \\ e^{jkl}\left(\frac{\cos\theta(\cos\theta\cos\phi\cos\zeta - \sin\phi\sin\zeta)}{1-\sin\theta\cos\phi} - \sin\theta\cos\zeta\right)(e^{(-1+\sin\theta\cos\phi)l} - 1) \end{bmatrix} \tag{3.14}$$

3.6 MATLAB IMPLEMENTATION OF THE BLT SOLUTION

Eq 3.13 and Eq 3.14 (as well as the simplified voltage expressions) were implemented in Matlab as a function in order to verify the BLT solution and obtain Monte Carlo results. The programming exploited Matlab's efficient matrix and vector operations in order to avoid the use of slower "for" loops. In this manner, the function is able to produce results for various parameter values en mass without iteration. To verify that the programmed function produced the correct results, a sample problem was selected, used in two previous implementation of the BLT solution [15],[16]. The physical problem has a characteristic impedance of 589Ω with load and source impedances of 295Ω. The transmission line was assumed lossless and in free space (although the comparative problems assigned a conductivity and thus a loss to the transmission line it was neglected herein). The angle θ was fixed at 30 degrees and the angles ϕ and ζ were fixed at 180 degrees. The frequency was varied from 0 to 90 MHz and the resulting near-end magnitude was calculated as a function of $(kd)/2$. Fig. 3-3 shows the results for the near-end current which are in agreement with the previous implementations [15],[16].

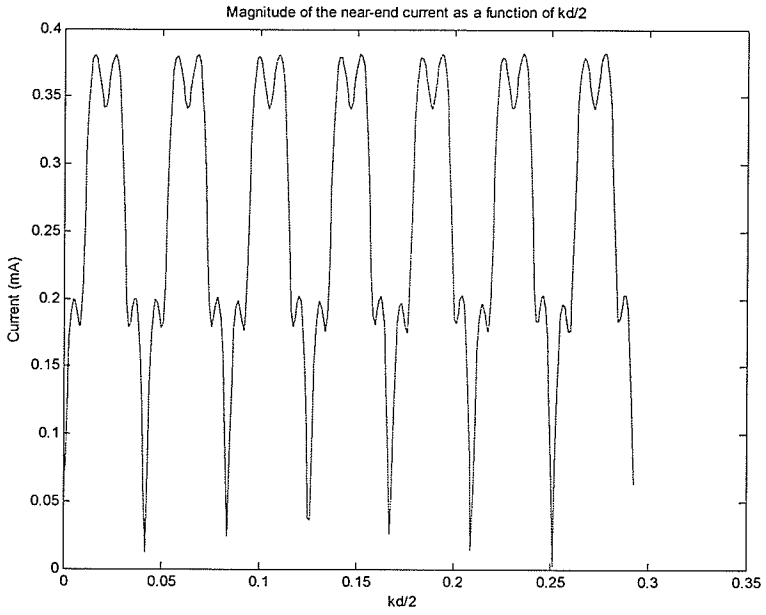

Figure 3-3. Verification of the BLT Solution

It is from the developed equations and the implemented Matlab function that a statistical analysis of the load currents and voltages arising from an impinging field on a transmission line will be investigated in the following chapters. This is first accomplished by a Monte Carlo analysis in Chapter 4, followed by an analytic approach presented in Chapters 5 & 6.

CHAPTER 4. MONTE CARLO ANALYSIS OF THE STOCHASTIC COUPLING PROBLEM

In this chapter, distributions of the BLT solution parameters are defined. The selection of these distributions is made based on physical coupling problems of interest, although any arbitrary distribution could be assigned to any of the parameters in question. From the assigned distributions and the aforementioned Matlab implementation of the BLT solution, numerical densities for various physical problems are presented in an attempt to classify the resulting probability density functions as being exponential, gamma or Rayleigh distributed.

4.1 MOTIVATION FROM THE PHYSICAL PROBLEM

It is intuitive from the complexity of the BLT solution that the randomness of the impinging plane wave, together with the physical properties of the transmission line, will greatly affect the resulting current or voltage distribution at the transmission line terminations. As an illustrative example, consider the case of a 30 m transmission line with 20 cm separation distance, matched at both ends ($\rho_0 = \rho_l = 0$). The source is assumed to have a deterministic frequency of 60 MHz while the polar angle of incidence is assumed to be from the horizon ($\theta = \pi/2$). The azimuthal angle ϕ and the field phase angle $\angle E$ are selected to be uniformly distributed over $(0, 2\pi)$ while the field magnitude is deterministically selected to be 1 V/m. In the first case, the polarization of the electric field ζ is deterministically selected to be 0 rad while in the second case, it is selected to be

uniformly distributed over $(0, 2\pi)$ rad. Fig. 4-1 shows the resulting probability densities of the near-end voltage magnitude and phase for deterministic polarization (top) and random polarization (bottom).

Even in this simplified example, it is evident that the assumed randomness of even a single field parameter can greatly affect the form of the obtained density. Therefore, the research herein considers very specific random parameter distributions extracted from potential physical problems. In addition, from the plots of Fig. 4-1 it seems as though the phase, in both cases, is uniformly distributed over $(-\pi, \pi)$. In fact, this is the case for any single source plane wave provided that the phase of the field is assumed to be uniformly distributed over $(0, 2\pi)$. Due to this result, only the magnitude of the voltage at the terminations of the transmission line will be shown for the remainder of this work.

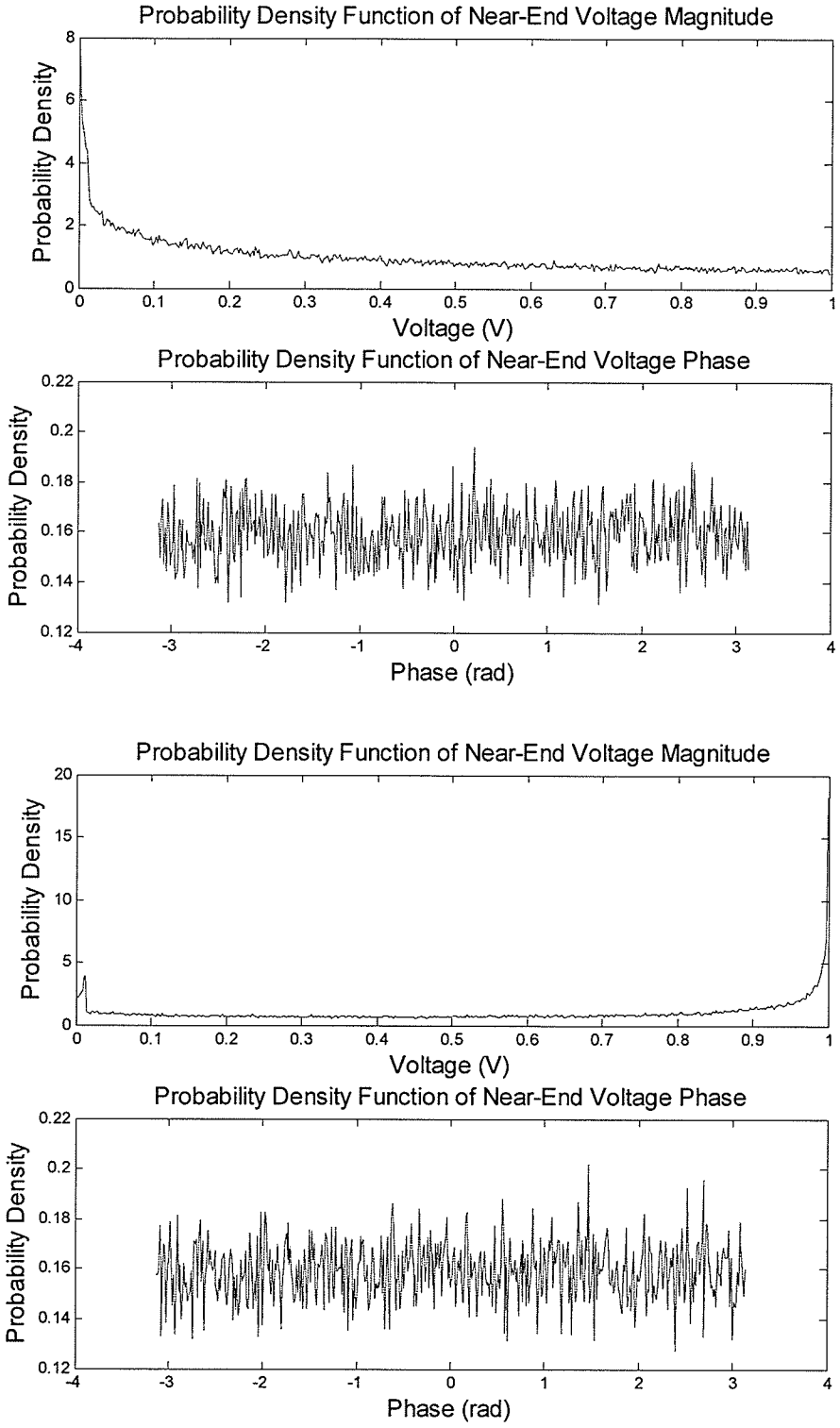

Figure 4-1. An illustration of the BLT solution complexity for random plane waves - deterministic polarization (top), random polarization (bottom)

4.2 FOUR PHYSICAL PROBLEMS

To limit the scope of this research, the following four coupling problems are considered.

4.2.1 A Single Source Incident from Anywhere in Three-Dimensions

In this problem, a single source of interference is assumed equally likely to be incident from any direction. For convenience, this source uncertainty is referred to as a three-dimensional problem (as the source can be incident from any direction in three-dimensional Cartesian space) The source may have either a deterministic frequency or a frequency uniformly distributed over a range of frequencies (from f_i to f_f). The field magnitude is also assumed to be deterministic or uniformly distributed from $|E_i|$ to $|E_f|$. Finally, the polarization and phase angles of the source are both assumed to be uniformly distributed over $(0, 2\pi)$ rad. The uniform distribution of the phase angle limits this problem to interference wavelengths much smaller than the distance from the source to the transmission line. If instead the wavelength was large relative to the source-transmission line separation, it is more likely that the phase of the field arriving at the transmission line would be congregated around a single value, a problem that is not considered herein.

4.2.2 A Single Source Incident from the Horizon

In this problem, the frequency, magnitude, polarization and phase of the field are selected as in the three-dimensional case but the source angle of incidence is assumed to be level with the transmission line at $\theta = \pi/2$. This selection of random parameters could be accurately used to describe a field from a distant transmitter such as a radio station antenna to a power line. For convenience this is referred to as the two-dimensional problem.

4.2.3 Multiple Sources Incident from Anywhere in Three-Dimensions

In this problem, the random parameters are selected as in the single source three-dimensional case but the total induced termination current or voltage is assumed to be attributed to a sum of N statistically independent plane-waves where each wave can have a different location of origin. Physically, the occurrence of each mode could be attributed to multiple paths from the source to the transmission line due to obstacle reflections. The assumption of statistical independence would only hold if the multiple paths introduced sufficient field variation from the source to the transmission line. Although using a simple sum of N modes appears to be a limited approximation to the total field at the transmission line, it has been shown to be an accurate model for the fields resulting in complex cavities [23]-[24].

4.2.4 Multiple Source Incident from the Horizon

Once again, the random parameters are selected as in the single source two-dimensional case are considered, but now the total current or voltage at the transmission line terminations is again assumed to be attributed to the sum of N independent sources.

4.3 UNIFORM DISTRIBUTIONS

In the selected problems of interest, it is necessary to select parameters that are either uniformly distributed over an interval (e.g the phase of the electric field is assumed uniformly distributed over $(0, 2\pi)$) or that are uniformly distributed over a sphere (e.g. the source angle of incidence in the three-dimensional problems).[1] The probability density function describing a random variable $\boldsymbol{x}$[2] uniformly distributed over an interval (a, b) is

1. The remainder of this research assumes that the reader is familiar with the basic concepts of probability and random variables including probability density functions and probability distributions. A concise review is available in Appendix 3.
2. In general, boldface variables are reserved for random variables

simply:

$$f_x(X) = \frac{1}{b-a} \tag{4.1}$$

Therefore, selecting a field magnitude uniformly distributed over the region E_i to E_f requires the density:

$$f_{|E|} = \frac{1}{|E_f| - |E_i|} \tag{4.2}$$

To select an incident waveform who's source is uniformly distributed over a sphere, the angles θ and ϕ in the spherical coordinate system of Fig. 3-2 are selected to be random variables calculated as:

$$\begin{aligned} \theta &= \operatorname{acos}(2u-1) \\ \phi &= 2\pi v \end{aligned} \tag{4.3}$$

where u and v are uniformly distributed random variables on the interval $(0, 1)$ [25]. This set of random variables describes source locations such that the occurrence of each spherical coordinate is equally likely.

It should be commented that the selection of uniform distributions for the field frequency and amplitude are rather arbitrary. The only justification is that in most practical problems, it is unlikely that the field frequency or amplitude will be distributed over an unbounded interval. Therefore, the simplest bounded distribution, namely the uniform one, was selected.

4.4 MONTE CARLO SIMULATION

A simple way to determine the distributions arising in a complicated problem is to use Monte Carlo simulation to numerically generate the desired probability densities and to then attempt to fit a known curve to the results. For the coupling problem in question, Monte Carlo analysis simply requires generation of the random parameters and for each

instance of the parameters, the evaluation of the termination voltages or currents using the programmed Matlab function. Once a sufficient number of solutions have been obtained, a density function can be numerically generated by normalizing a histogram of the results (where normalization is performed such that the area under the curve is unity as required of all probability density functions).

In this fashion, a transmission line analysis utility tool was developed as a GUI in Matlab. The interface is shown in Fig. 4-2. Here, the user is capable of specifying the distributions of the parameters for single and multiple waves as well as the desired number of samples and bins to be used in the calculation of the normalized histogram plots (the plots of Fig. 4-1 were created using this tool). In addition to the field parameters, the geometry of the line and the line terminations are fully adjustable. Using the developed tool, it is an easy matter to investigate the density functions that arise for the problems of interest.

In the next section, numerous different numerical probability density functions are displayed for a wide variety of source parameters and transmission line geometries (including termination impedances). The purpose of the plots is to both show that the coupling problem produces hugely varying densities based on the assumed physical parameters and to obtain a qualitative idea of how the resulting densities vary as the parameters of the problem are changed. No formal proof for the arising densities is presented.

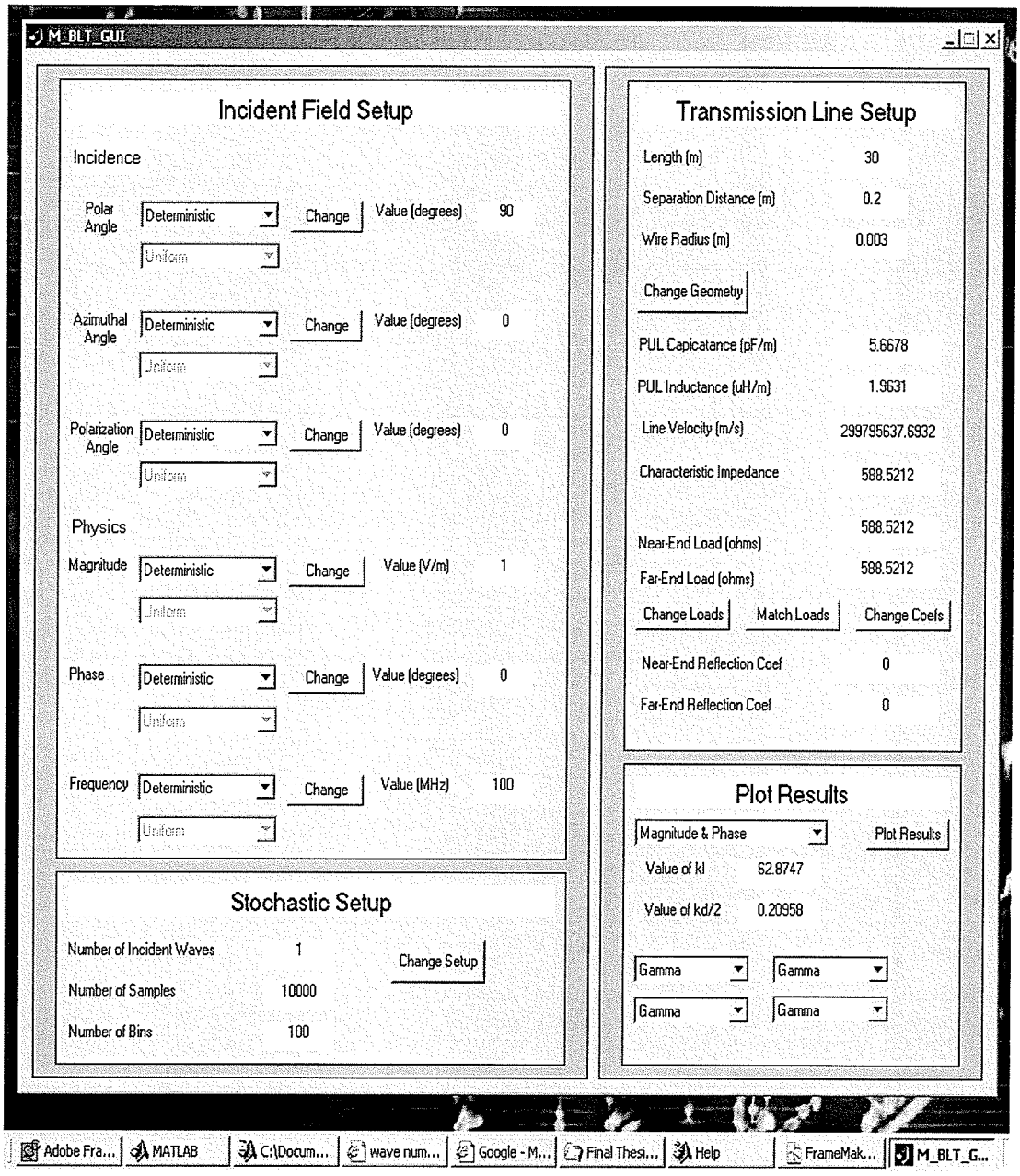

Figure 4-2. Monte Carlo analysis tool

4.5 MONTE CARLO RESULTS - A SINGLE SOURCE INCIDENT N THREE DIMENSIONS

4.5.1 The Effects of Frequency and Line-Length

Although the four specific problems under consideration have been formulated to describe the random nature of the impinging electric field, the geometry and terminations of the transmission line must also be taken into account. As a first case, consider the single source, three-dimensional problem. The transmission line is selected to have a length of 30 m and a conductor separation of 0.1 m with a characteristic impedance of 100Ω and matched loads. The field magnitude is chosen to be 10 V/m and the frequency is selected at 60 MHz. The conductor separation and field magnitude are conveniently selected such that the product $|E|d = 1$. The resulting wave number is 1.26 and the probability density function for the voltage magnitude occurring at the near- and far-end of the transmission line is shown in Fig. 4-3 (the near-end density is on the top while the far-end density is on the bottom - the convention used for all figures when both the near- and far-end densities are shown). A summary the physical parameters of all tests performed will be provided in table format for convenience. For this problem, the physical parameters are summarized in Table 4-1 and in all tables, the impedances are assumed to have units of Ω.

Table 4-1. 3-D Single Source - Setup A

Frequency	Field Strength	Length	Separation	k	Z_c	Z_0/ρ_0	Z_L/ρ_L
60 Mhz	10 V/m	30 m	0.1 m	1.26	100	100/0	100/0

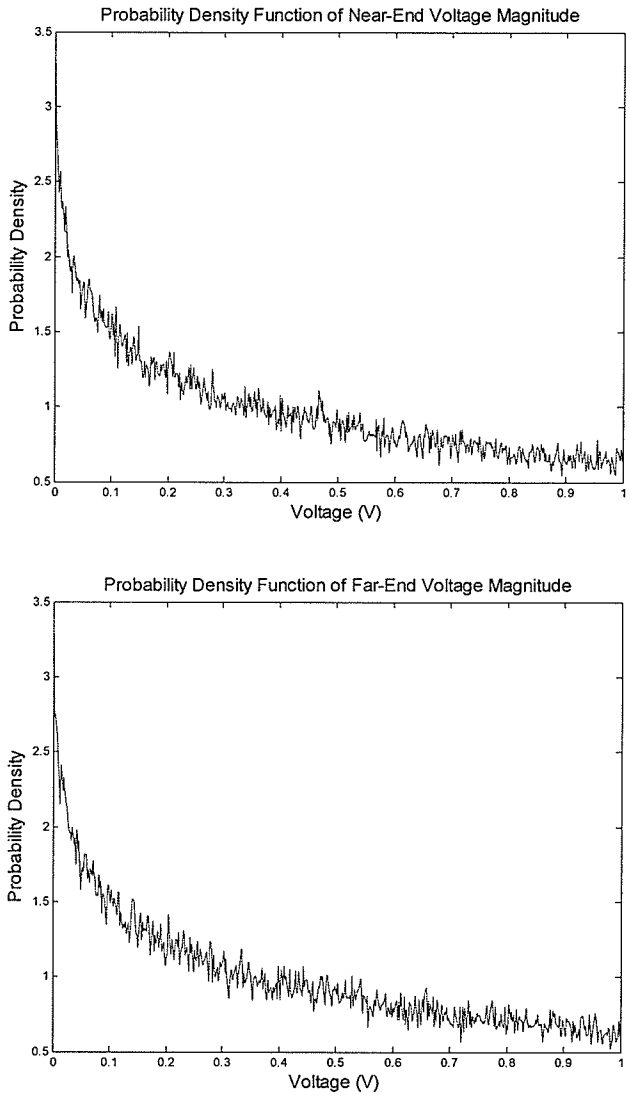

Figure 4-3. 3-D single source - Setup A

The density function reveals that the voltage is limited below a maximum of 1 V with a greater probability of voltage levels near 0 V than near the maximum.

Dropping the frequency of the source to 100 kHz results in the probability density of Fig. 4-4.

Table 4-2. 3-D Single Source - Setup B

Frequency	Field Strength	Length	Separation	k	Z_c	Z_0/ρ_0	Z_L/ρ_L
100 kHz	10 V/m	30 m	0.1 m	0.002	100	100/0	100/0

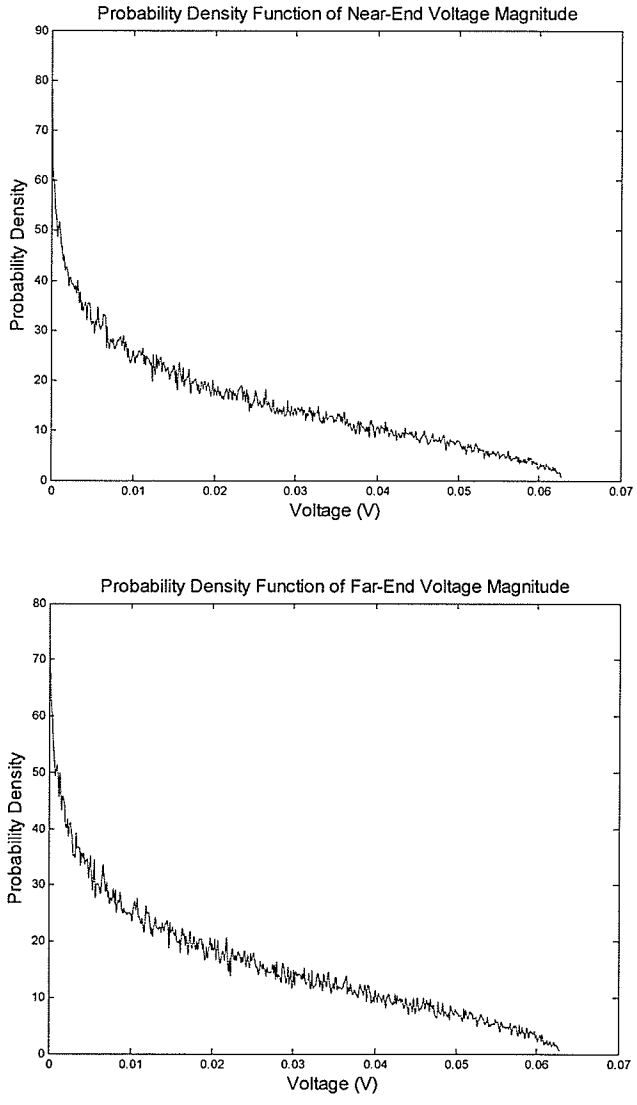

Figure 4-4. 3-D single source - Setup B

Notably, the only change in the problem parameters is that the wave number is now 0.002. Examining the resulting far-end density shows that the maximum voltage magnitude has been reduced from 1 V to 0.06 V and although the general shape of the density function seems to be approximately the same, the lower frequency density has a tail that tappers directly to 0 V. At this point, it is also apparent that due to the stochastic nature of the incident field, provided the loads are matched at both ends of the transmission line, the densities of the near- and far-end will be the same. For the remainder of this research, when the transmission-line terminations are matched, only the near-end voltage density function is shown.

In order to identify the effects of frequency and line-length, it is sufficient to analyze the BLT solution for horizontal incidence ($\theta = \pi/2$) (it is assumed that the frequency dependence will be similar in the 3-dimensional case). In the case of matched terminations, the near-end voltage becomes (from Eq 3.10):

$$V(0) = \frac{1}{2} e^{-jkl} S_2 \tag{4.4}$$

And the source term S_2 becomes:

$$S_2 = -Ed\left\{ e^{jkl}\left(\frac{\cos\theta(\cos\theta\cos\phi\cos\zeta - \sin\phi\sin\zeta)}{1 - \sin\theta\cos\phi} - \sin\theta\cos\zeta \right)\left(e^{(-1+\sin\theta\cos\phi)jkl} - 1\right)\right\} \tag{4.5}$$

For horizontal incidence $\sin(\theta) = 1$ and when $\cos(\phi) = -1$ and $\cos(\zeta) = 1$ maximum coupling occurs and the source term becomes:

$$S_2 = -Ede^{jkl}(e^{-j2kl} - 1) \tag{4.6}$$

such that the absolute value of the near-end voltage is:

$$|V(0)| = \frac{1}{2}|E|d|(e^{-j2kl} - 1)| \tag{4.7}$$

The maximum value of the voltage is clearly $|E|d$ only if $e^{-j2kl} = -1$. Therefore, the maximum coupled voltage to the transmission reaches $|E|d$ only if $kl > \pi/2$. If this value of kl is not reached, the coupling to the line will achieve a maximum value less than $|E|d$. In the results of Fig. 4-3 (Table 4-1) the value of kl is 37.8 resulting in a maximum coupling of $|E|d = 1V$. However, in the case of Table 4-2 the value of kl is 0.063 and, being less than $\pi/2$ results in a lower maximum coupling value.

To further demonstrate the effect of the kl product, consider the same transmission line geometry and a frequency of 100 MHz (effectively changing the wavenumber to 2.01). The resulting numerical probability density of the near-end voltage magnitude is shown in Fig. 4-5

Table 4-3. 3-D Single Source - Setup C

Frequency	**Field Strength**	**Length**	**Separation**	***k***	Z_c	Z_0/ρ_0	Z_L/ρ_L
100 MHz	10 V/m	30 m	0.1 m	0.02	100	100/0	100/0

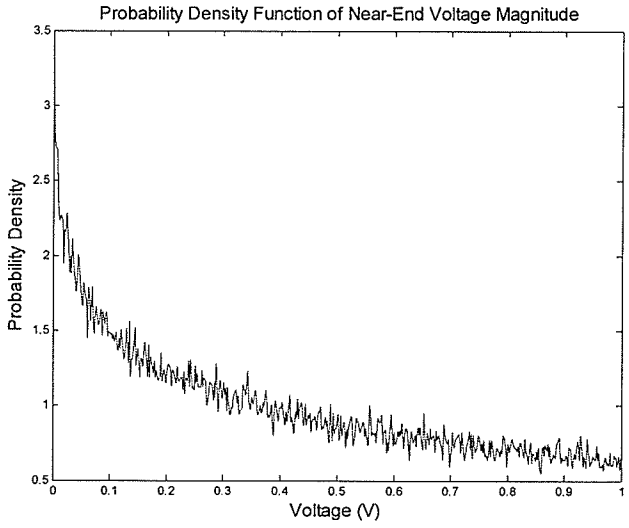

Figure 4-5. 3-D single source - Setup C

As expected, since the product kl is greater than $\pi/2$ the density function reaches the maximum value of 1 V. At this point it is apparent that changing the length of the transmission line will affect the resulting distribution in the same manner as changing the frequency and so only frequency changes are considered for the remainder of this discussion.

It is of interest to examine the effects of uncertainty on the frequency. For example, if the frequency is uniformly distributed over a range of 100 kHz to 60 MHz the numerical density of Fig. 4-6 arise:

Table 4-4. 3-D Single Source - Setup D

Frequency	**Field Strength**	**Length**	**Separation**	***k***	Z_c	Z_0/ρ_0	Z_L/ρ_L
100 kHz to 60 MHz	10 V/m	30 m	0.1 m	0.002 to 1.26	100	100/0	100/0

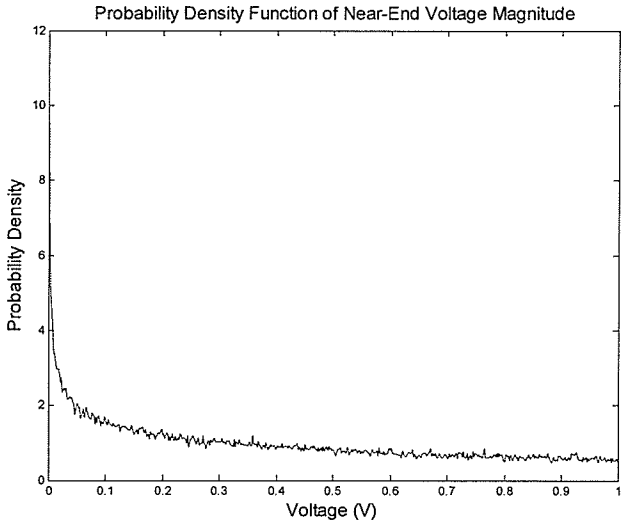

Figure 4-6. 3-D single source - Setup D

Seemingly, the low- and high-frequency effects tend to give the density the same form as the high-frequency simulations.

4.5.2 The Effects of Load Terminations

To this point, only matched terminations have been considered. As a result, no reflections occur on the transmission line and the probability density functions obtained have been relatively smooth. To begin investigating the effects of termination mismatches, a mismatch at the source is introduced. Specifically, the termination impedances are selected as $Z_o = 50$ and $Z_l = 100$ at a frequency of 60 MHz. The resulting numerical densities are shown in Fig. 4-7

Table 4-5. 3-D Single Source - Setup E

Frequency	**Field Strength**	**Length**	**Separation**	***k***	Z_c	Z_0/ρ_0	Z_L/ρ_L
60 MHz	10 V/m	30 m	0.1 m	1.26	100	50/-0.33	100/0

Notably, there is very little change in the shape of the distribution from previous matched examples. Of interest is that the near-end maximum is now approximately 0.66 V while the far-end density reaches the largest possible maximum of 1 V with a noticeable discontinuity in the density at around 0.66 V. A qualitative explanation of the probability density behaviour is obtainable by considering the form of the BLT solution:

$$\begin{bmatrix} V(0) \\ V(l) \end{bmatrix} = \frac{1}{2(\rho_0\rho_l - e^{2\gamma l})} \begin{bmatrix} (1+\rho_0)(-\rho_l)S_1 + (1+\rho_0)(-e^{\gamma l})S_2 \\ (1+\rho_l)(-e^{\gamma l})S_1 + (1+\rho_l)(-\rho_0)S_2 \end{bmatrix} \tag{4.8}$$

In the case of a mismatched source but matched load, the near-end and far-end voltages becomes:

$$\begin{bmatrix} V(0) \\ V(l) \end{bmatrix} = \frac{1}{-2e^{2jkl}} \begin{bmatrix} (1+\rho_0)(-e^{jkl})S_2 \\ (-e^{jkl})S_1 - \rho_0 S_2 \end{bmatrix} \tag{4.9}$$

and it is apparent that the near end voltage is only a function of S_2 resulting in a similar density as the matched case. In contrast, the far-end voltage is a function of both S_1 and S_2.

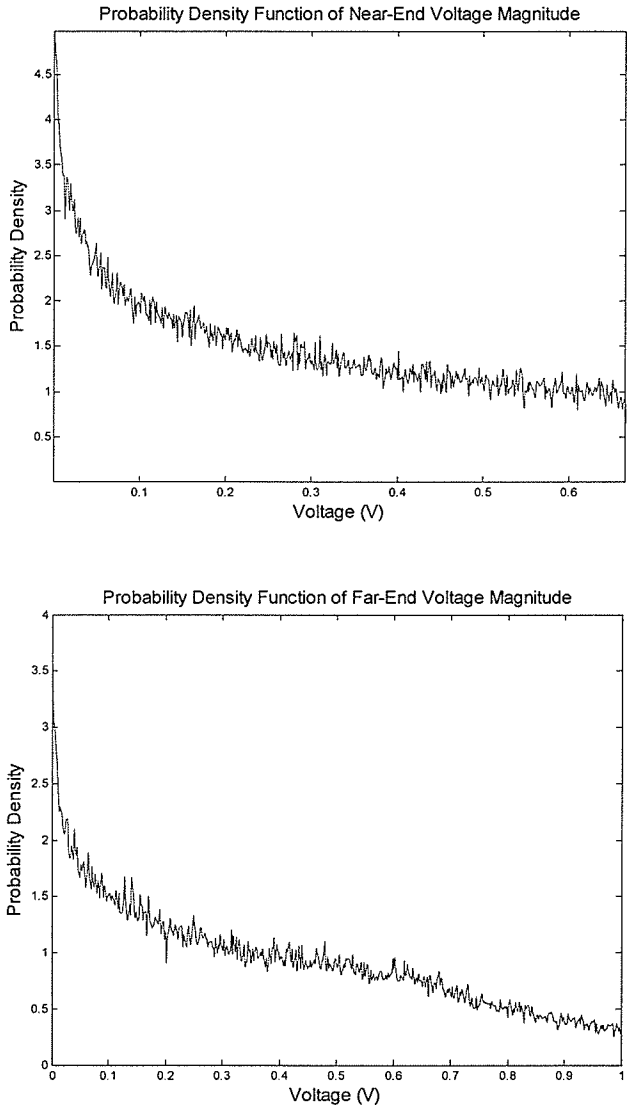

Figure 4-7. 3-D single source - Setup E

While it is merely speculated that it is this superposition that gives the far-end density its discontinuity, this assumption is further validated when the source frequency is reduced to 100 kHz.

Table 4-6. 3-D Single Source - Setup F

Frequency	Field Strength	Length	Separation	k	Z_c	Z_0/ρ_0	Z_L/ρ_L
100 kHz	10 V/m	30 m	0.1 m	0.002	100	50/-0.33	100/0

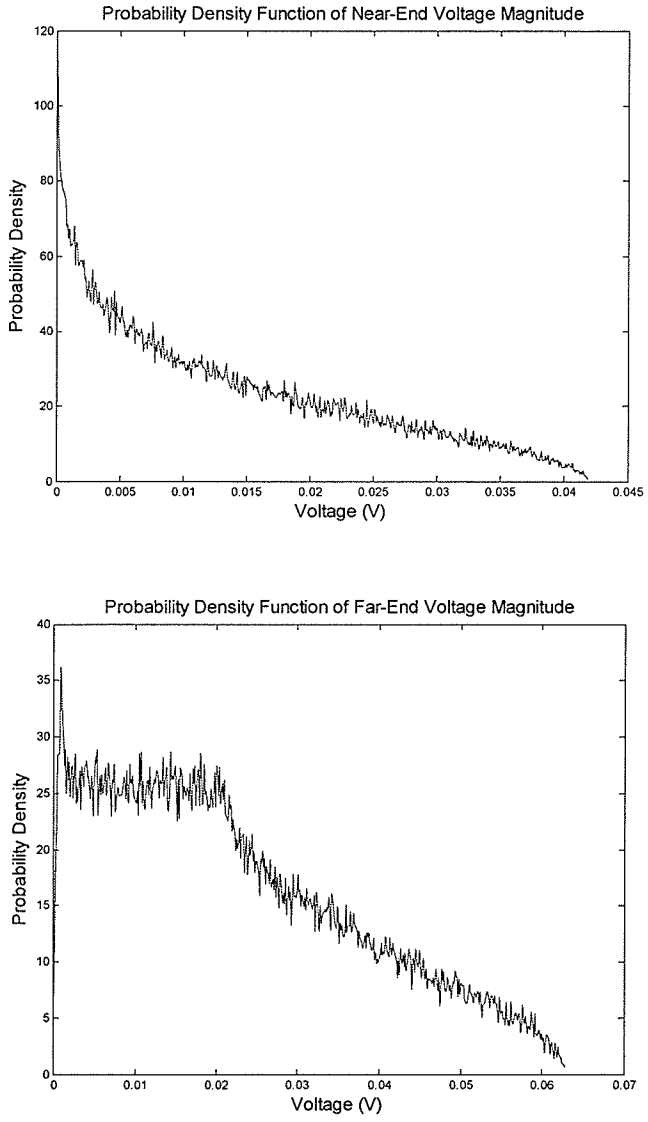

Figure 4-8. 3-D single source - Setup F

Now, the superposition of the two source terms S_1 and S_2 is very apparent in the far-end density. It is also of interest to notice that the effect of the superposition is ultimately governed by the value of the reflection coefficients as indicated by Eq 4.9. This suggest that the more closely matched the terminations, the smoother the resulting density function. The same frequency dependence as in the matched case can give rise to some very peculiar density functions when the terminations are unmatched as illustrated by raising the frequency to 1 MHz:

Table 4-7. 3-D Single Source - Setup G

Frequency	**Field Strength**	**Length**	**Separation**	***k***	Z_c	Z_0/ρ_0	Z_L/ρ_L
1 MHz	10 V/m	30 m	0.1 m	0.02	100	50/-0.33	100/0

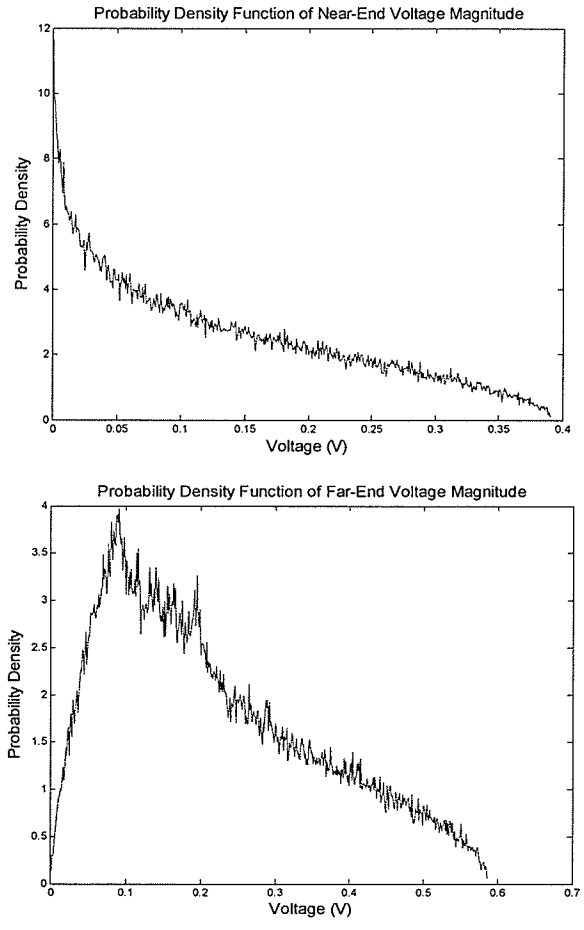

Figure 4-9. 3-D single source - Setup G

If the terminations are now unmatched at both the load and source by selecting $Z_o = 5000$ and $Z_l = 50$ the resulting reflection coefficients are $\rho_0 = 0.96$, $\rho_l = -0.33$ and the probability densities take a wild deviation from those already encountered:

Table 4-8. 3-D Single Source - Setup H

Frequency	Field Strength	Length	Separation	*k*	Z_c	Z_0/ρ_0	Z_L/ρ_L
1 MHz	10 V/m	30 m	0.1 m	0.02	100	5000/ 0.96	50/-0.33

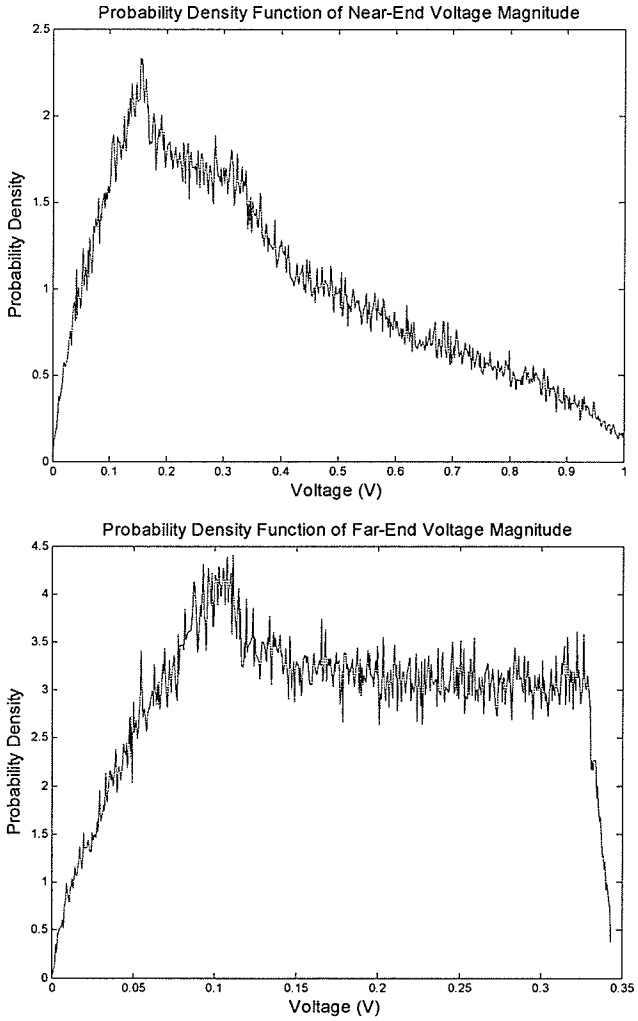

Figure 4-10. 3-D single source - Setup H

Once again, raising the frequency back to 60 MHz gives:

Table 4-9. 3-D Single Source - Setup I

Frequency	Field Strength	Length	Separation	k	Z_c	Z_0/ρ_0	Z_L/ρ_L
60 MHz	10 V/m	30 m	0.1 m	1.26	100	5000/ 0.96	50/-0.33

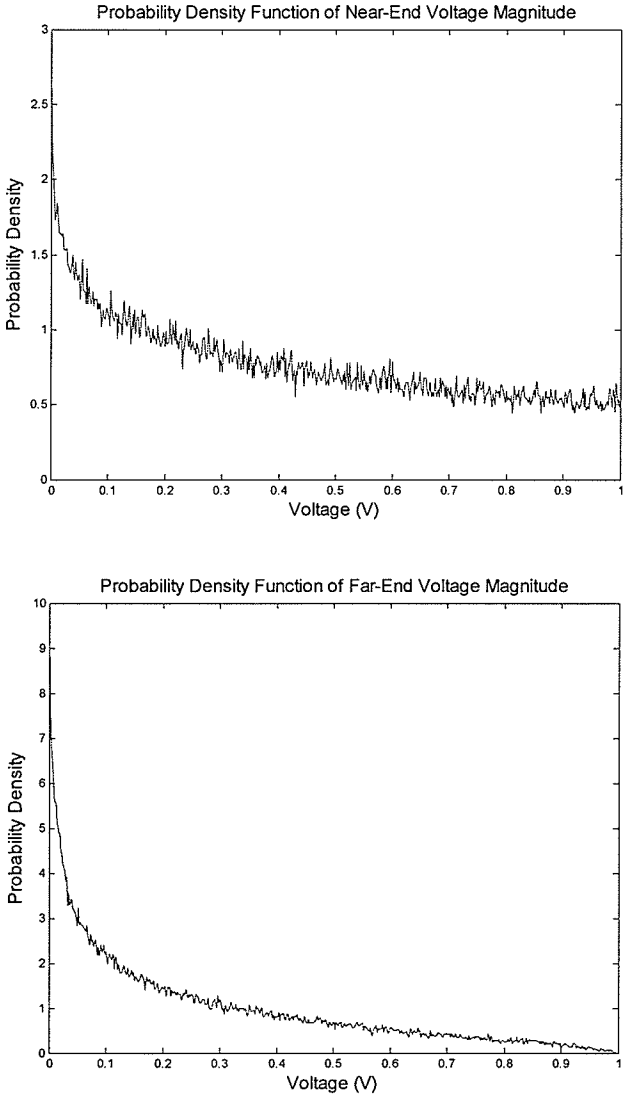

Figure 4-11. 3-D single source - Setup I

From these results it seems that the reflection coefficients play less of a role at large values of kl.

If uncertainty in the frequency allows the assumption that the frequency is uniformly distributed from 100 kHz to 60 MHz the near-end density of Fig. 4-12 is obtained (the far-end density is of a similar shape):

Table 4-10. 3-D Single Source - Setup J

Frequency	**Field Strength**	**Length**	**Separation**	***k***	Z_c	Z_0/ρ_0	Z_L/ρ_L
100 kHz to 60 MHz	10 V/m	30 m	0.1 m	0.0021 to 1.26	100	5000/ 0.96	50/-0.33

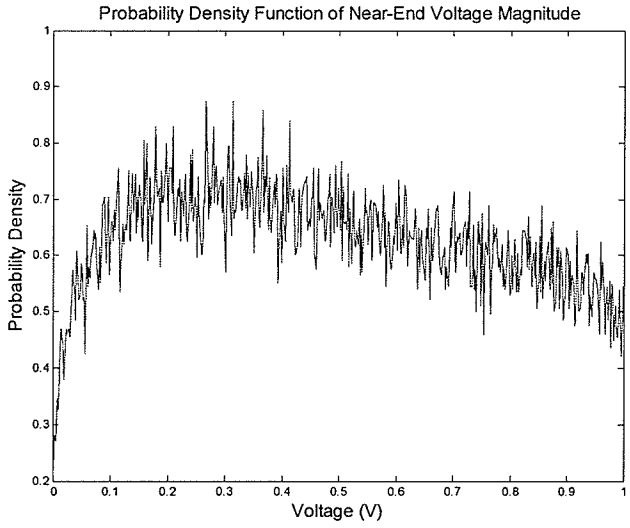

Figure 4-12. 3-D single source - Setup J

This particular density is unlike any that have been encountered so far. Changing the termination impedances to $Z_o = 50\Omega$ and $Z_l = 75\Omega$ but keeping the frequency range from 100 kHz to 60 MHz results in the densities of Fig. 4-13, which simply shows how much the shape of the probability density function depends on the reflection coefficients when low-frequency fields (relative to the length of the line) are present.

Table 4-11. 3-D Single Source - Setup K

Frequency	Field Strength	Length	Separation	k	Z_c	Z_0/ρ_0	Z_L/ρ_L
100 kHz to 60 MHz	10 V/m	30 m	0.1 m	0.0021 to 1.26	100	50/-0.33	75/-0.14

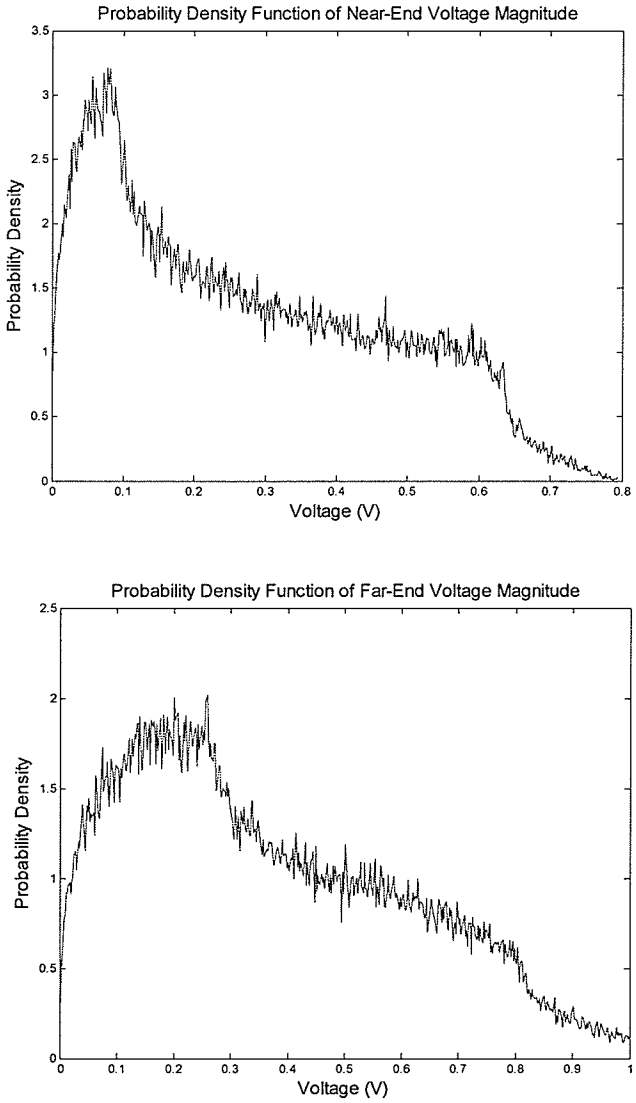

Figure 4-13. 3-D single source - Setup K

Having seen the wide variety of densities functions arising from numerous transmission lines and field frequencies, it seems unlikely that a single function will adequately describe all cases. Fortunately, Monte Carlo analysis makes it possible to quickly calculate the densities for any geometry and source.

4.5.3 Effect of Field Magnitude

To this point, only a deterministic field magnitude has been considered. Although the previous results show only the case of a 10 V/m field magnitude, it can be shown (as found in Example 3 of Section 5.4 in Chapter 5) that multiplying a distribution by a different constant simply scales the distribution accordingly. Hence, if the electric field was instead 1 V/m or 100 V/m all of the resulting distributions would have the exact same form over a different interval. If however, significant uncertainty is present in the field magnitude, many of the distributions already seen seem to become more regular. Consider the case of Table 4-1 and Table 4-2 where now the field magnitude is uniformly distributed between 10 and 20 V/m. The following results are obtained which are very similar to those for the deterministic case:

Table 4-12. 3-D Single Source - Setup L

Frequency	**Field Strength**	**Length**	**Separation**	***k***	Z_c	Z_0/ρ_0	Z_L/ρ_L
60 MHz	10 to 20 V/m	30 m	0.1 m	1.26	100	100/0	100/0

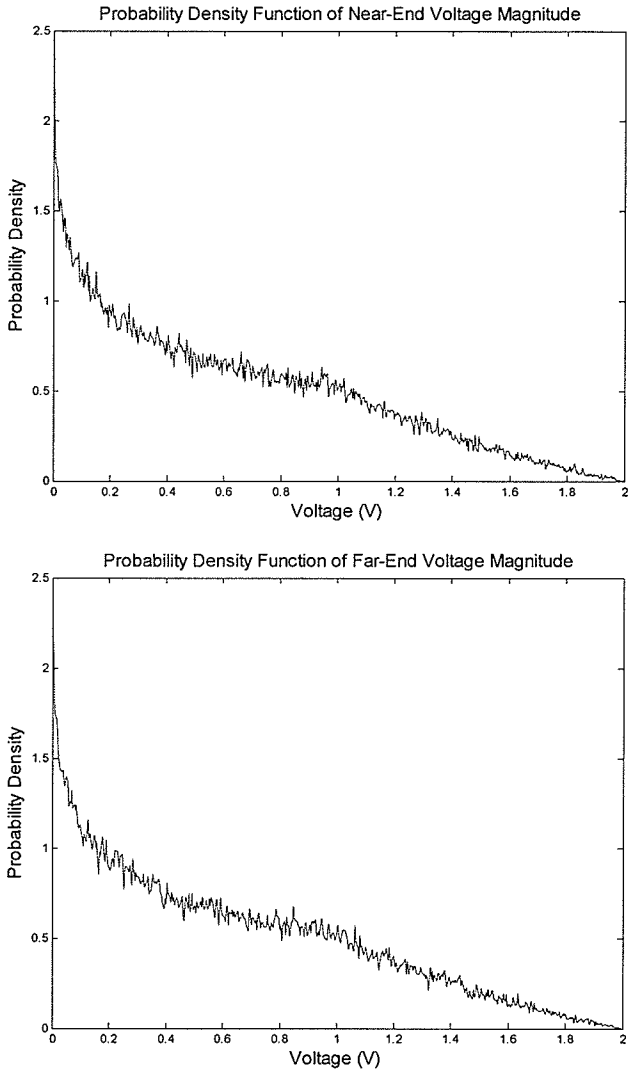

Figure 4-14. 3-D single source - Setup L

Table 4-13. 3-D Single Source - Setup M

Frequency	Field Strength	Length	Separation	*k*	Z_c	Z_0/ρ_0	Z_L/ρ_L
100 kHz	10 to 20 V/m	30 m	0.1 m	1.26	100	100/0	100/0

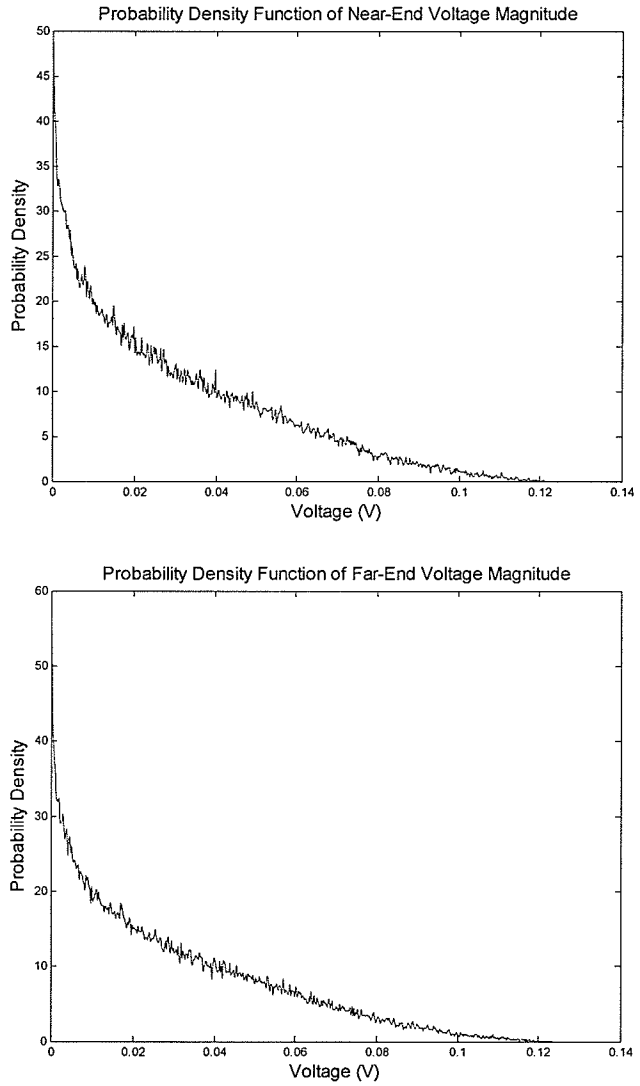

Figure 4-15. 3-D single source - Setup M

In the case of termination mismatches the uncertainty in the field magnitude seemingly smooths the overall density of the termination voltages as shown by comparing the results of Table 4-11 with the same parameters except for source uncertainty from 10-20 V/m.

Table 4-14. 3-D Single Source - Setup N

Frequency	Field Strength	Length	Separation	k	Z_c	Z_0/ρ_0	Z_L/ρ_L
100 kHz to 60 MHz	10 to 20 V/m	30 m	0.1 m	0.002 to 1.26	100	50/-0.33	75/-0.14

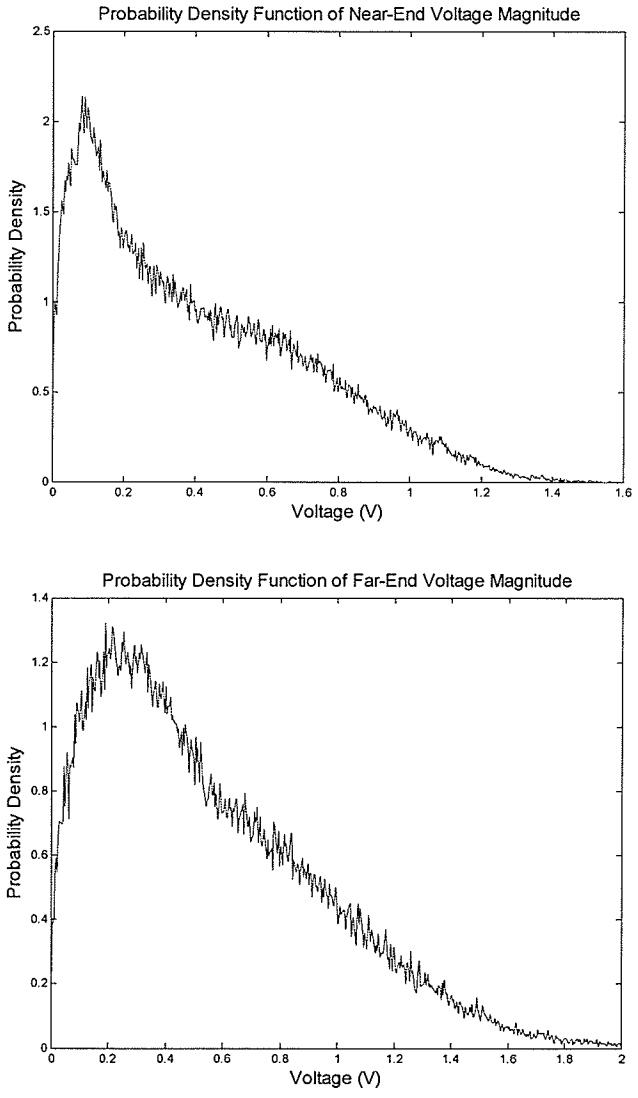

Figure 4-16. 3-D single source - Setup N

If even further uncertainty is assume such that the field magnitude takes on equally likely values from 10 V/m to 100 V/m, the results of Fig. 4-17 are obtained.

Table 4-15. 3-D Single Source - Setup O

Frequency	Field Strength	Length	Separation	k	Z_c	Z_0/ρ_0	Z_L/ρ_L
100 kHz to 60 MHz	10 to 100 V/m	30 m	0.1 m	0.002 to 1.26	100	50/-0.33	75/-0.14

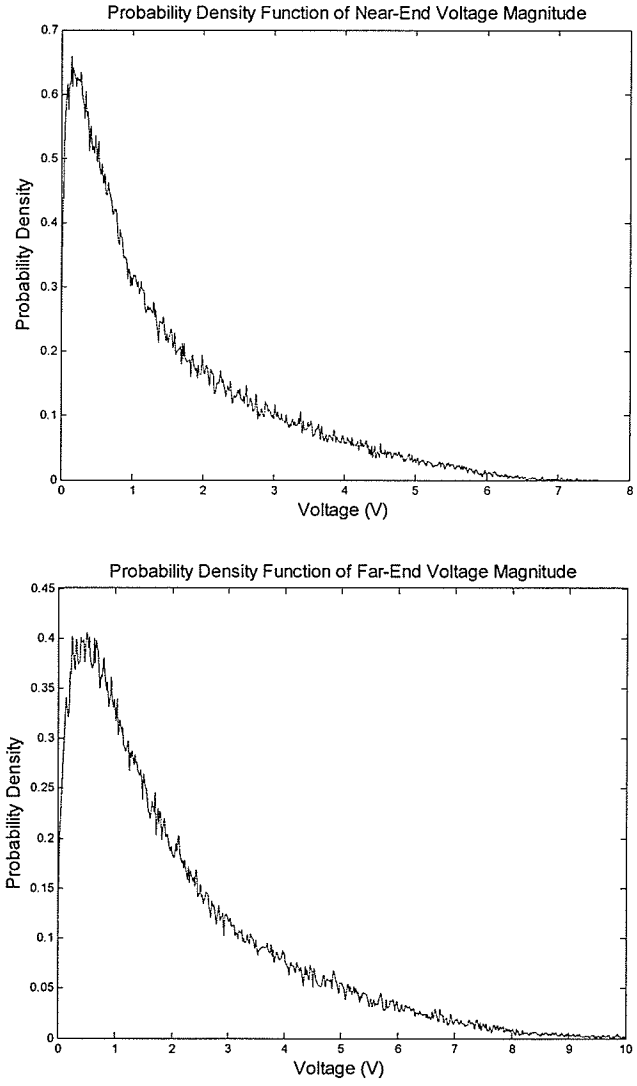

Figure 4-17. 3-D single source -Setup O

In general, the effects of the termination mismatches are reduced as the uncertainty in the field level increases. Comparing this same range of field magnitude with the matched case shows a limiting-type monotonic density function:

Table 4-16. 3-D Single Source - Setup P

Frequency	Field Strength	Length	Separation	*k*	Z_c	Z_0/ρ_0	Z_L/ρ_L
100 kHz to 60 MHz	10 to 100 V/m	30 m	0.1 m	0.002 to 1.26	100	100/0	100/0

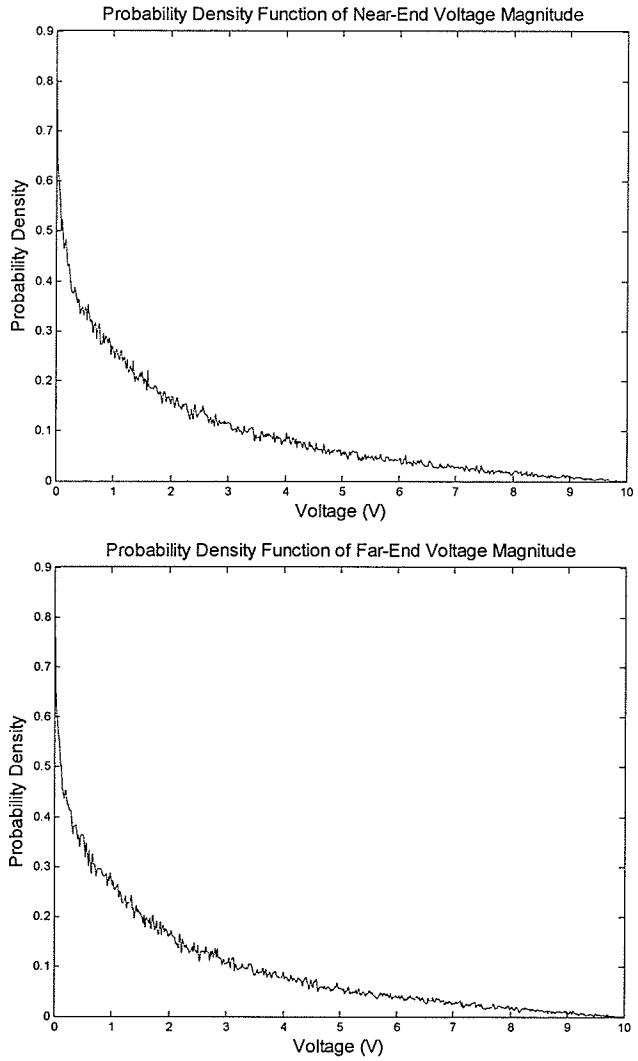

Figure 4-18. 3-D single source - Setup P

4.5.4 Summary of the Three Dimensional Single Source Results

In summary, the resulting probability density functions for a single radiation source equally likely to be located anywhere in space, are highly dependent on the problem in question. It has been shown that for a monochromatic wave with deterministic field magnitude, the resulting density functions are smooth in the case of matched loads. In the case of load mismatches, large discontinuities appear in the density functions. These effects are minimized if sufficient uncertainty is present in the field magnitude or if the product kl is sufficiently high.

4.6 MONTE CARLO RESULTS - A SINGLE SOURCE ON THE HORIZON

Now considering a source impinging from the horizon ($\theta = \pi/2$) with the same frequency and physical properties as Table 4-1 the near-end results of Fig. 4-19 are generated.

Table 4-17. 2-D Single Source - Setup A

Frequency	**Field Strength**	**Length**	**Separation**	***k***	Z_c	Z_0/ρ_0	Z_L/ρ_L
60 MHz	10 V/m	30 m	0.1 m	1.26	100	100/0	100/0

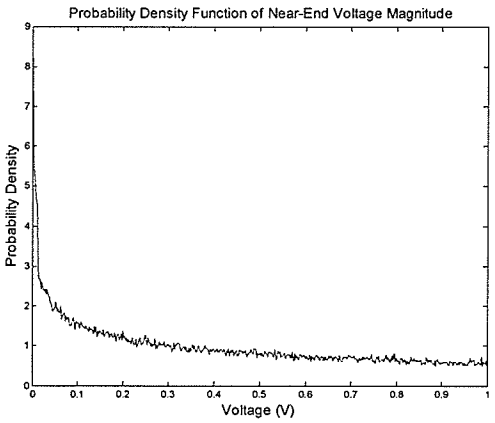

Figure 4-19. 2-D single source - Setup A

Once again the symmetry of matched loads is visible and the phase is uniformly distributed between $-\pi$ and π. Lowering the frequency to 100 kHz as in Table 4-2 produces the same effect as in the three dimensional case:

Table 4-18. 2-D Single Source - Setup B

Frequency	Field Strength	Length	Separation	k	Z_c	Z_0/ρ_0	Z_L/ρ_L
100 kHz	10 V/m	30 m	0.1 m	0.002	100	100/0	100/0

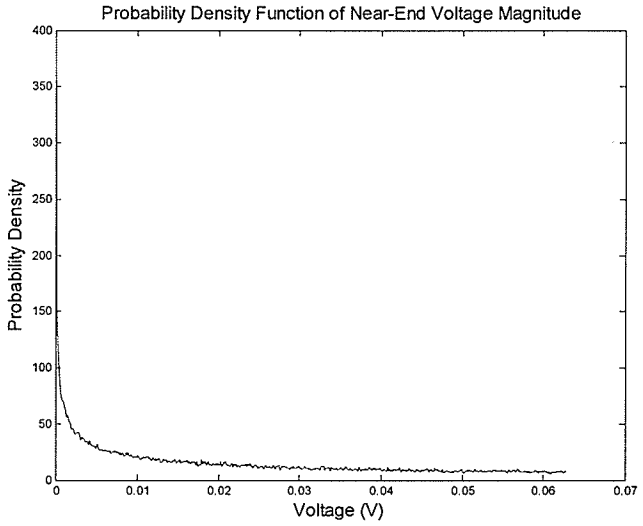

Figure 4-20. 2-D single source - Setup B

Once again, the maximum voltage level is reduced as explained by the dependence on the parameter kl in the previous section.

4.6.1 The Effects of Load Terminations

Once again, the effects of mismatches in the load are not very apparent at high values of kl. This is illustrated using $Z_o = 50\Omega$ while leaving the load impedance matched. The results are similar as those obtained for the three dimensional single source problem.

Table 4-19. 2-D Single Source - Setup C

Frequency	Field Strength	Length	Separation	k	Z_c	Z_0/ρ_0	Z_L/ρ_L
60 MHz	10 V/m	30 m	0.1 m	1.26	100	50/-0.33	100/0

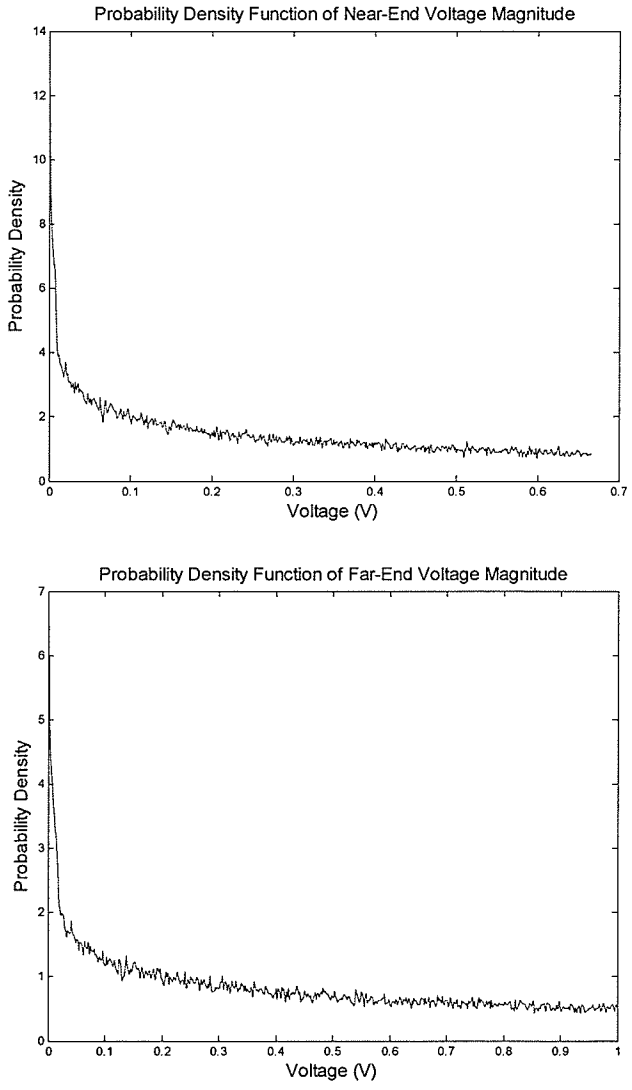

Figure 4-21. 2-D single source - Setup C

As in the three-dimensional case, lowering the frequency to 100 kHz thereby lowering the value of kl to 0.063 gives a great change in the probability density function at the load.

Table 4-20. 2-D Single Source - Setup D

Frequency	Field Strength	Length	Separation	k	Z_c	Z_0/ρ_0	Z_L/ρ_L
100 kHz	10 V/m	30 m	0.1 m	0.002	100	50/-0.33	100/0

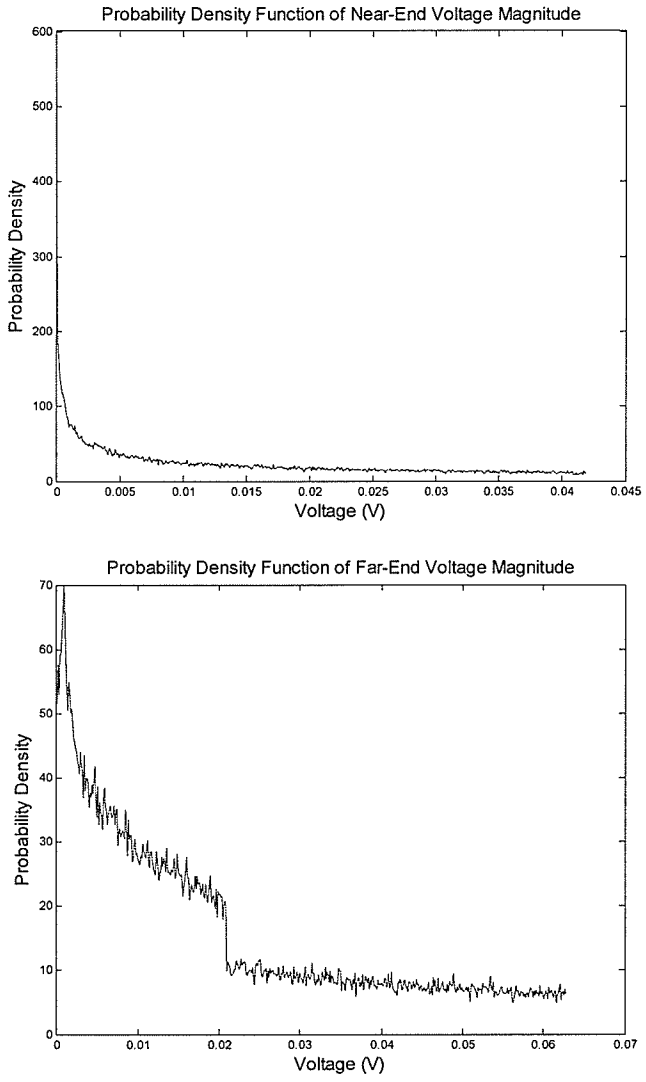

Figure 4-22. 2-D single source - Setup D

4.6.2 Effect of Field Magnitude

Sufficient uncertainty in the field strength once again brings the density function to a limiting-type monotonic case:

Table 4-21. 2-D Single Source - Setup E

Frequency	**Field Strength**	**Length**	**Separation**	***k***	Z_c	Z_0/ρ_0	Z_L/ρ_L
100 kHz	10 to 100 V/m	30 m	0.1 m	0.002	100	50/-0.33	100/0

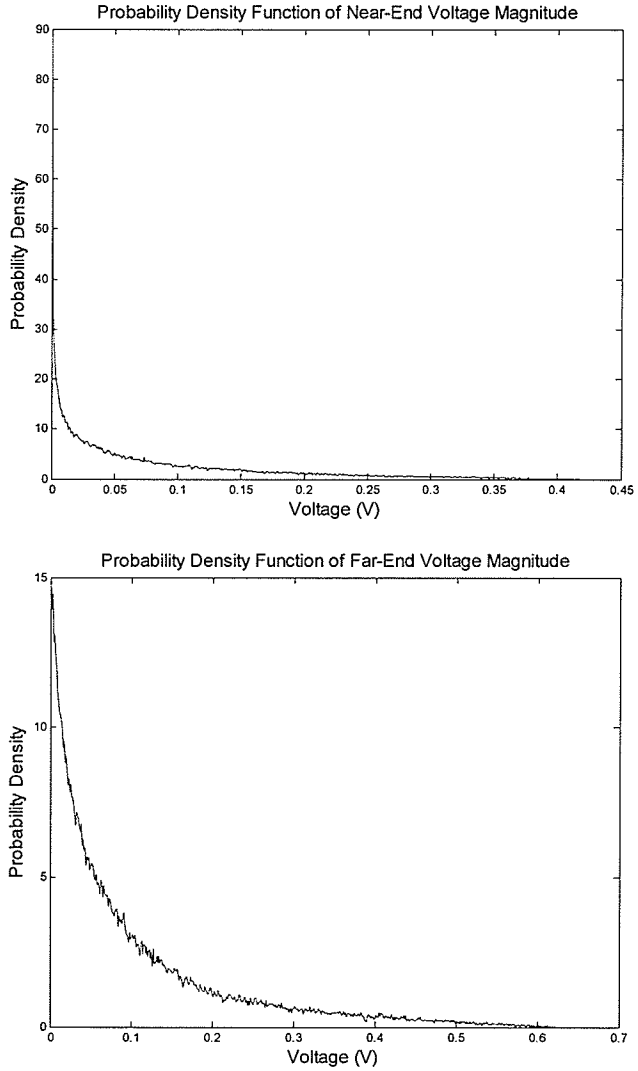

Figure 4-23. 2-D single source - Setup E

4.6.3 Summary of the Single Source on the Horizon Results

As seen from this brief numerical analysis of the single source located on the horizon, the qualitative results are very similar to those in the three-dimensional problem. In both cases, although the physics of the coupling problem greatly affect the probability density functions of the near- and far-end voltages, Monte Carlo analysis is capable of quickly generating plots that accurately portray the complexity of the distributions.

As it is often more convenient to analyze such a distribution analytically, it is now desired to see if any known density functions provide simple and accurate approximations to any of the probability density functions seen to this point. The remainder of this chapter attempts to fit a limited number of known distributions to the obtained numerical results for both single source problems and the problems of N sources both the three and two dimensional cases.

4.7 SOME COMMON PROBABILITY DENSITIES

Although numerical Monte-Carlo algorithms are convenient for discovering the density function of a random event, it is often desired to be able to describe the nature of the distribution with an analytic expression. For example, if an EMC engineer was attempting to design protection for a transmission line in an environment where the field levels are stochastically defined, it would be more convenient to work from an analytic formula for the voltage levels than from a numerical plot.

Herein, only the exponential, gamma and Rayleigh distributions are considered which occur commonly in a wide array of statistical problems. Each of the considered density functions exists for all positive values of the dependent variable from $(0, \infty)$. As will be seen, this type of infinite tail is not ideal due to the bounded nature of the BLT solution.

4.7.1 *The Exponential Distribution*

The exponential distribution is characterized by the probability density function:

$$f_e(x) = \lambda e^{-\lambda x} \tag{4.10}$$

and is a distribution with a single shape parameter λ. The general shape of the curve is shown in Fig. 4-24 for $\lambda = 2$ and $\lambda = 0.2$. Overall, as the parameter changes, the general shape of the density remains the same.

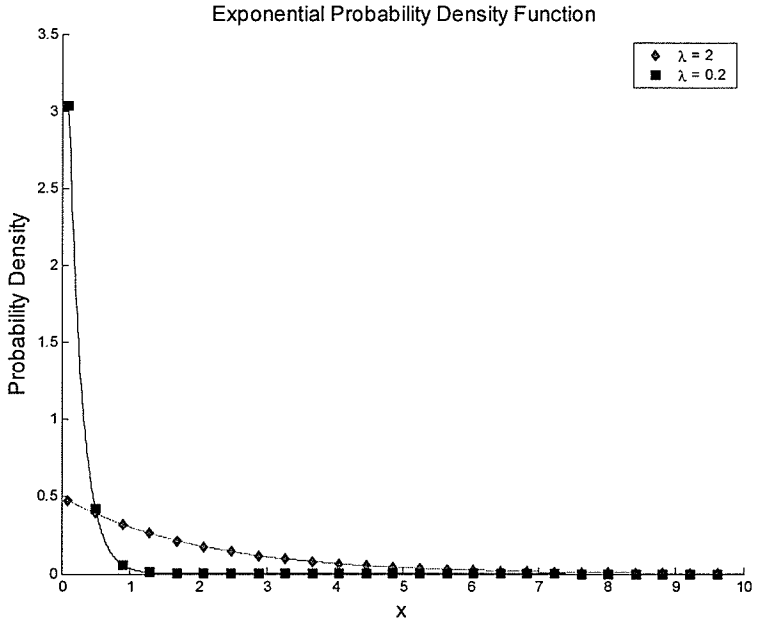

Figure 4-24. Exponential distribution

4.7.2 *The Gamma Distribution*

The gamma distribution is characterized by the density function:

$$f_{gam}(x) = \frac{1}{\beta^{\alpha}\Gamma(\alpha)} x^{\alpha-1} e^{-x/\beta},\ 0 \le x < \infty \tag{4.11}$$

and is a function of two parameters α and β. The function Γ is known as the gamma function and is defined as:

$$\Gamma(\alpha) = \int_0^\infty t^{\alpha-1} e^{-t} dt. \tag{4.12}$$

where, if the argument α is an integer n, the resulting gamma function simplifies to:

$$\Gamma(n+1) = n!, \tag{4.13}$$

where ! denotes the usual factorial operation. The density is shown below for $\alpha = 1$ and $\beta = 1, 2$.

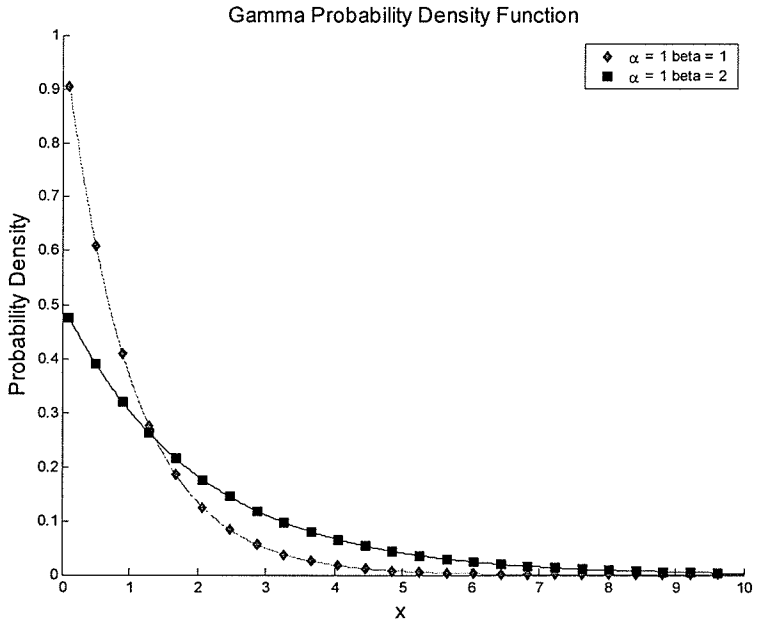

Figure 4-25. Gamma distributions

4.7.3 The Rayleigh Distribution

The Rayleigh distribution arises classically from the square-root of the sum of two normally distributed independent random variables [22]. The distribution requires a single parameter σ and may be defined in terms of its density function:

$$f_{rayl}(x) = \frac{x}{\sigma^2} e^{-\frac{x^2}{2\sigma^2}}, x > 0 \tag{4.14}$$

and is shown in Fig. 4-26 for $\sigma = 1$ and $\sigma = 2$.

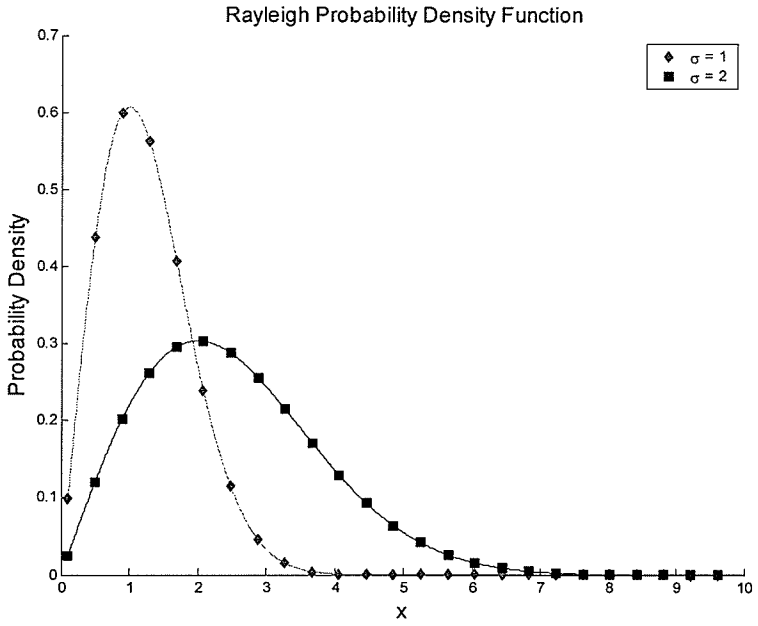

Figure 4-26. Rayleigh distributions

4.8 FITTING DISTRIBUTIONS TO MONTE CARLO RESULTS

The Matlab statistical toolbox contains built in functions for fitting the distributions in question to a set of randomly generated data. The procedure uses Maximum Likelihood Estimation (MLE) [22] to provide a fit to within a default of 95% confidence.

For some of the coupling problems of interest, Matlab was used to fit a probability density, each of the type gamma, exponential and Rayleigh to the Monte Carlo simulations. In the case of single sources, only those problems resulting in sufficiently smooth densities were selected for fitting. For any of the obtained density functions where load-mismatches resulted in a density function that was highly discontinuous Monte Carlo analysis is probably best, but as will be shown, in some situations with mismatched loads, high frequency and field magnitude uncertainty can make fitting accurate.

In addition to the single source cases distribution fits were generated for multiple sources located anywhere in space and anywhere on the horizon.

4.8.1 Fitting to the Three-Dimensional Single Source Problem

Consider yet again the first example of this chapter given in Table 4-1 (reproduced here for convenience). The resulting density function and attempted distribution fitting for the near-end voltage is shown in Fig. 4-27.

Table 4-22. 3-D Single Source Fit - Setup A

Frequency	**Field Strength**	**Length**	**Separation**	***k***	Z_c	Z_0/ρ_0	Z_L/ρ_L
60 MHz	10 V/m	30 m	0.1 m	1.26	100	100/0	100/0

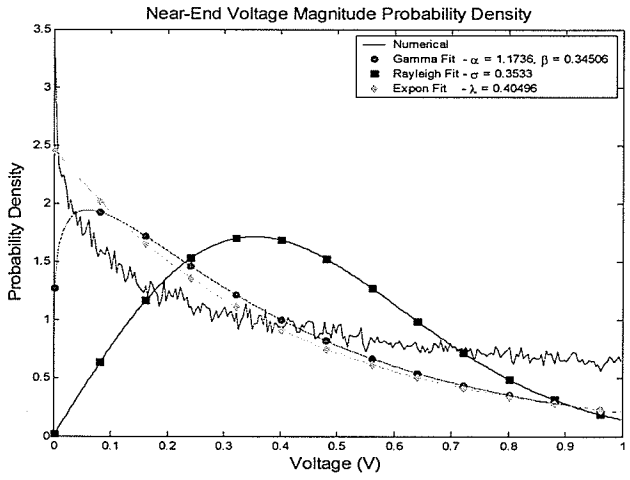

Figure 4-27. MLE fit for 3-D single source - Setup A

From the plots it appears that none of the maximum likelihood estimations seem to fit the numerical curve very well. Actually, this is expected because the numerical density function does not go to zero in the interval $(0, 1)$. In attempting to fit this kind of a distribution with a density function having an infinite tail, no parameter selection will result in a good fit because for the entirety of the fitting curve is to be contained within $(0, 1)$ it must ultimately go to 0 on that interval. This suggests however, that lowering the frequency to 100 kHz as in Table 4-2 will give a better fit as the resulting numerical density goes much closer to 0 in the interval $(0, 1)$ This is shown in Fig. 4-28, again for the near-end density function

Table 4-23. 3-D Single Source Fit - Setup B

Frequency	**Field Strength**	**Length**	**Separation**	***k***	Z_c	Z_0/ρ_0	Z_L/ρ_L
100 kHz	10 V/m	30 m	0.1 m	0.002	100	100/0	100/0

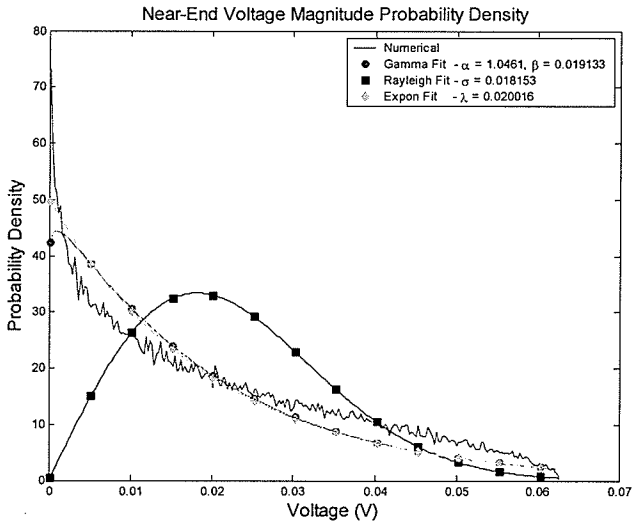

Figure 4-28. MLE fit for 3-D single source - Setup B

Even though now the numerical density function approaches zero in the interval $(0, 1)$ and the gamma and exponential functions fit better than in Fig. 4-28, both the gamma and exponential MLEs fail to adequately capture the random nature of the voltage magnitudes. Potentially, this could pose a problem to an EMC design engineer. Suppose,

for cost reasons, it is desired to design cable protection against 80% of all possible incident fields in a stochastic environment. In order to obtain the required information for designing such protection it is convenient to look at the cumulative probability distribution (CDF) of the problem, obtainable by numerically integrating the density function. The CDF for this problem is compared to the CDFs of the exponential, gamma and Rayleigh distributions having parameters associated with the MLE fits of Fig. 4-29

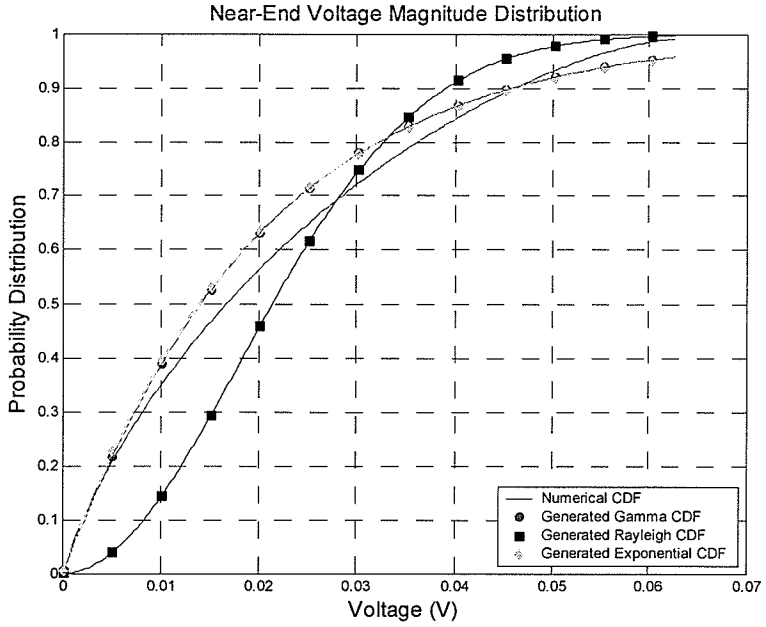

Figure 4-29. CDF for 3-D single source - Setup B

In the numerical CDF, 80% of the probability is contained below 0.36 V while in the gamma and exponential distributions, 80% probability is contained below 0.31 V. Although the difference appears small in this case, when more coupled energy is possible, the difference will become more evident. Consequently, the undershoot of the gamma and exponential fits could potentially lead to system failure if the 80% protection limits are stringent.

There is a single case where a distribution fit works very well for matched loads. If the uncertainty in the field strength is assumed to be between 10 and 100 V/m the resulting distribution fits are:

Table 4-24. 3-D Single Source Fit - Setup C

Frequency	Field Strength	Length	Separation	k	Z_c	Z_0/ρ_0	Z_L/ρ_L
100 kHz	10 to 100 V/m	30 m	0.1 m	1.26	100	100/0	100/0

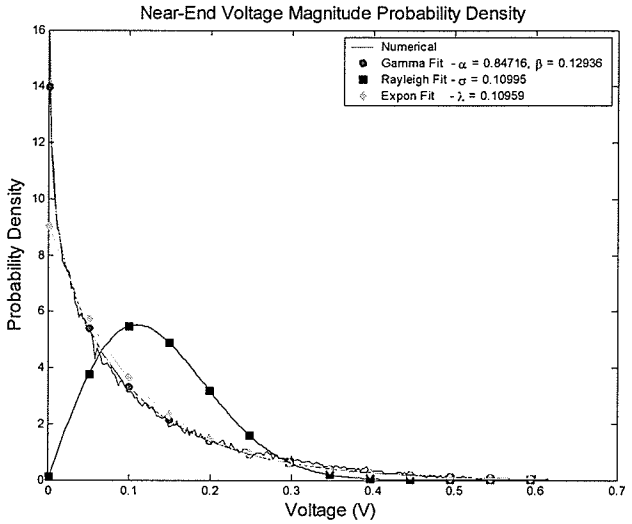

Figure 4-30. MLE fit for 3-D single source - Setup C

The CDF of the numerical results and gamma fit displayed in Fig. 4-31 show much better agreement than previously considered cases.

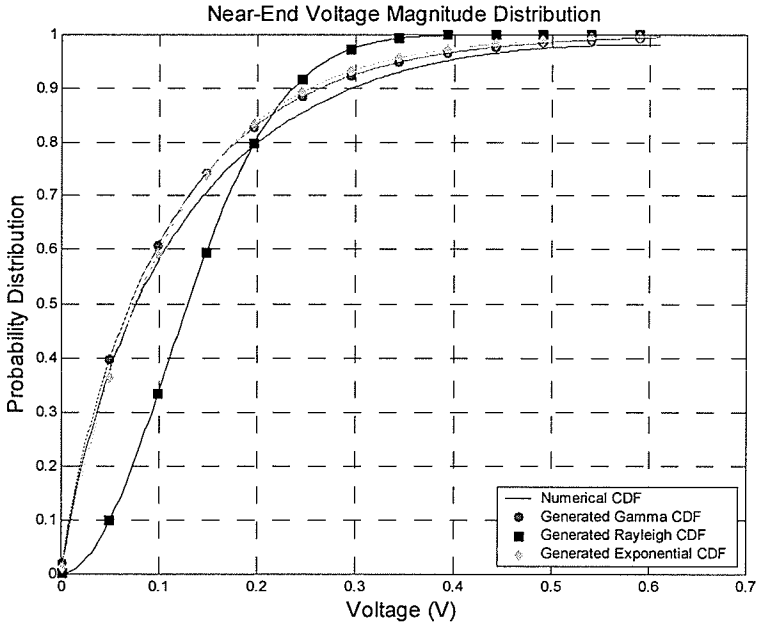

Figure 4-31. CDF for 3-D single source - Setup C

If the line terminations are mismatched, it is apparent from previous results that only sufficient uncertainty in the field strength and/or a sufficiently high maximum frequency will result in an accurate fit. As an example consider the results of Fig. 4-32 where the terminations have been selected as 75Ω and 95Ω where the field is once again a deterministic 10 V/m.

Table 4-25. 3-D Single Source Fit - Setup D

Frequency	**Field Strength**	**Length**	**Separation**	k	Z_c	Z_0/ρ_0	Z_L/ρ_L
100 kHz	10 V/m	30 m	0.1 m	1.26	100	75/-0.14	95/-0.026

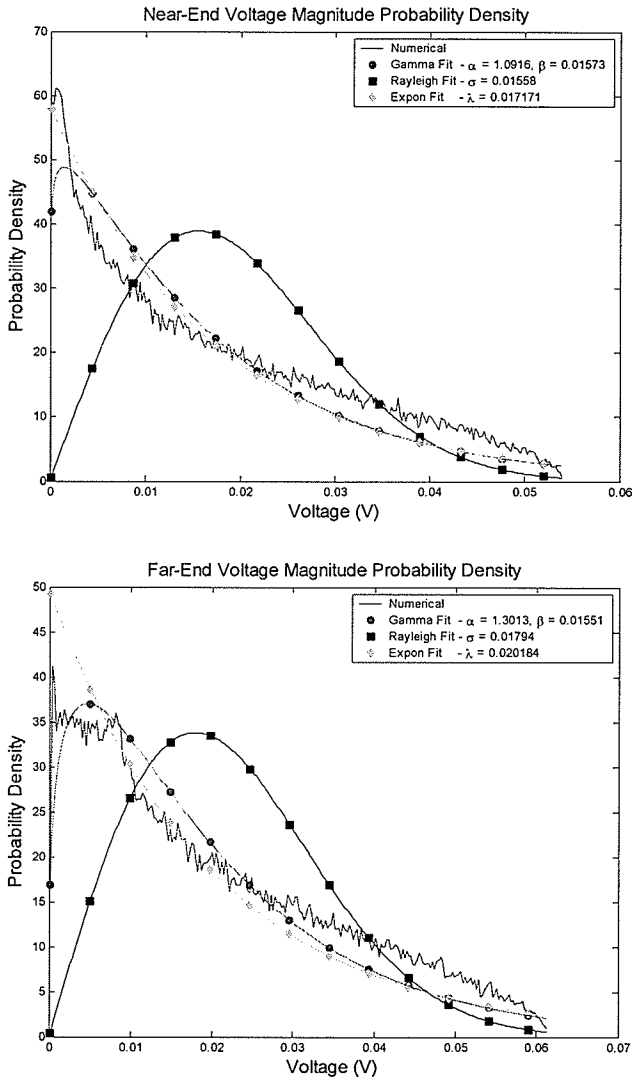

Figure 4-32. MLE fit for 3-D single source - Setup D

As expected, the gamma and exponential fits are still poor. If however, the field strength is assumed to be uniformly distributed between 10 and 100 V/m, the exponential and gamma fits are very accurate as shown in Fig. 4-33.

Table 4-26. 3-D Single Source Fit - Setup E

Frequency	Field Strength	Length	Separation	k	Z_c	Z_0/ρ_0	Z_L/ρ_L
60 MHz	10 to 100 V/m	30 m	0.1 m	1.26	100	75/-0.14	95/-0.026

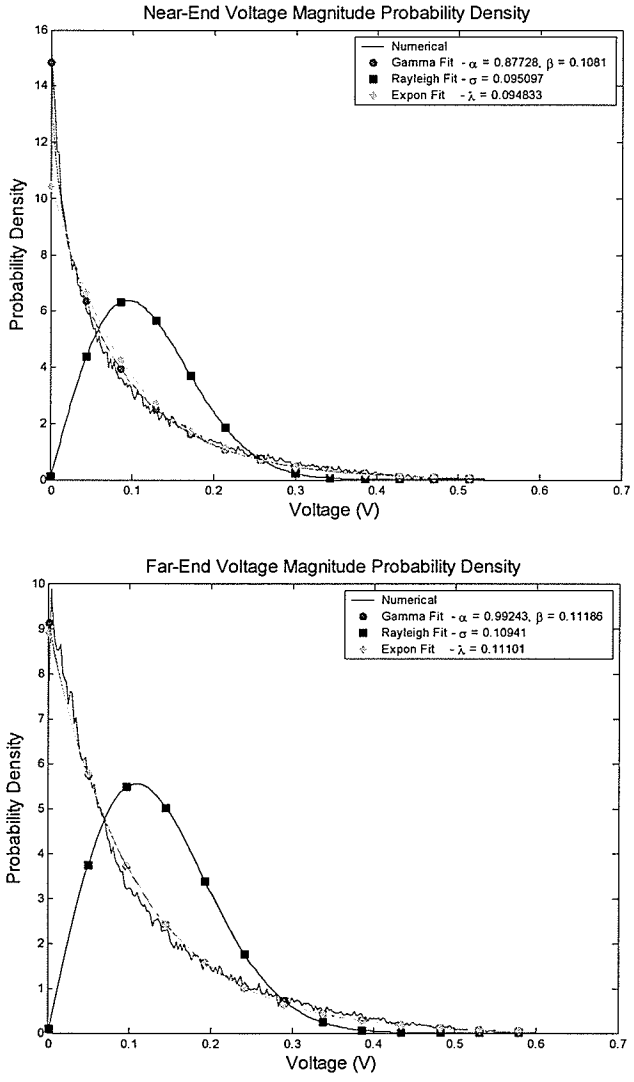

Figure 4-33. MLE fit for 3-D single source - Setup E

Having attempted to fit analytic distributions to the single-source 3-D problem it seems that good agreement occurs only if the field magnitude is contained in a sufficiently large interval. In all other cases, it does not seem that an exponential, gamma or Rayleigh distribution accurately captures the random nature of the coupling problem.

4.8.2 Fitting to the Two-Dimensional Single Source Problem

As already shown in the results of Fig. 4-19 to Fig. 4-23, the two-dimensional single source problem has similar trends as the three-dimensional problem. Therefore, probability density fitting to the horizontally located single source problem is not presented.

4.8.3 Fitting to the Three-Dimensional Multiple Source Problem

Considering the sum of N waves in the three-dimensional problem, two physical examples with 2 and 5 waves each adequately shows two extremes of the possible voltage densities. The first problem is that of matched loads at 100 kHz. Fig. 4-34 and Fig. 4-35 respectively, show the results of 2 and 5 waves on the far-end voltage density function.

Table 4-27. 3-D Multiple Source Fit - Setup A

Frequency	**Field Strength**	**Length**	**Separation**	***k***	Z_c	Z_0/ρ_0	Z_L/ρ_L
100 kHz	10 to 100 V/m	30 m	0.1 m	1.26	100	100/0	100/0

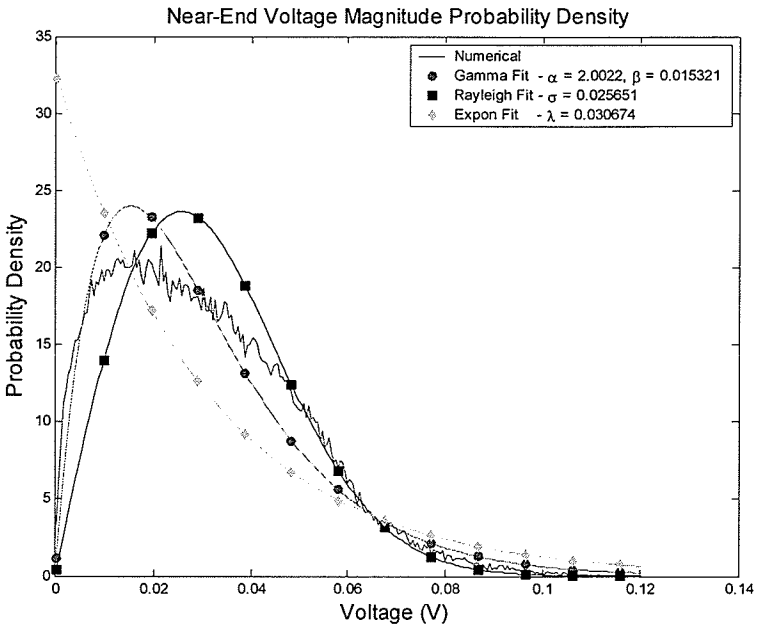

Figure 4-34. MLE fit for 3-D multiple sources - Setup A - 2 waves

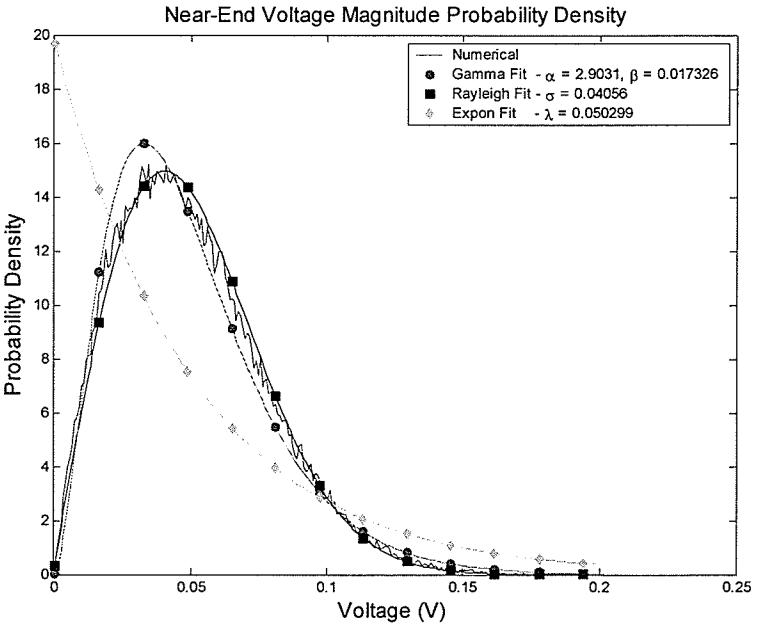

Figure 4-35. MLE fit for 3-D multiple sources - Setup A - 5 waves

From the two resulting densities and fits, it seems that as the number of waves increases, a Rayleigh density becomes an accurate measure of the voltage density. Although not shown, as the number of waves increases further, the Rayleigh fit becomes a better and better match.

For mismatched loads of 75Ω at the source and 95Ω at the load, the fits are shown for 2 and 5 waves in Fig. 4-36 and Fig. 4-37 respectively.

Table 4-28. 3-D Multiple Source Fit - Setup B

Frequency	**Field Strength**	**Length**	**Separation**	***k***	Z_c	Z_0/ρ_0	Z_L/ρ_L
100 kHz	10 V/m	30 m	0.1 m	1.26	100	75/-0.14	95/-0.026

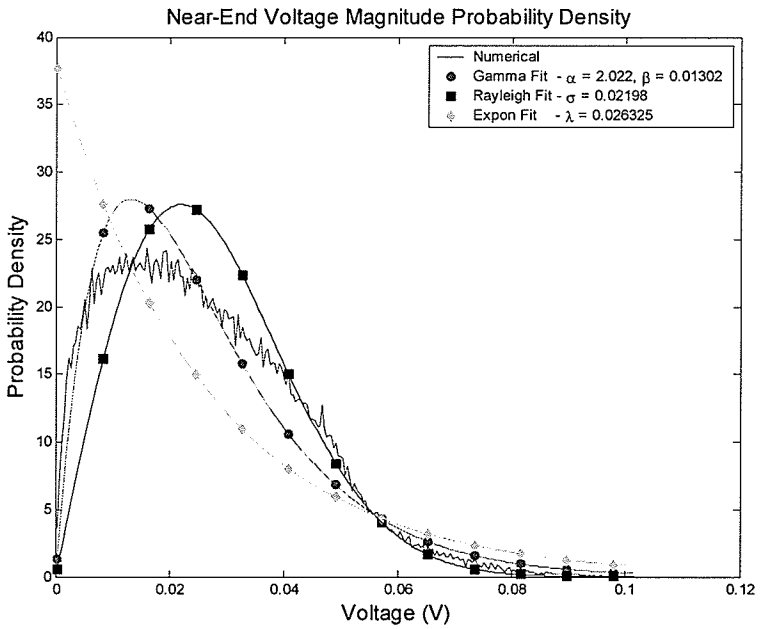

Figure 4-36. MLE fit for 3-D multiple sources - Setup B - 2 waves

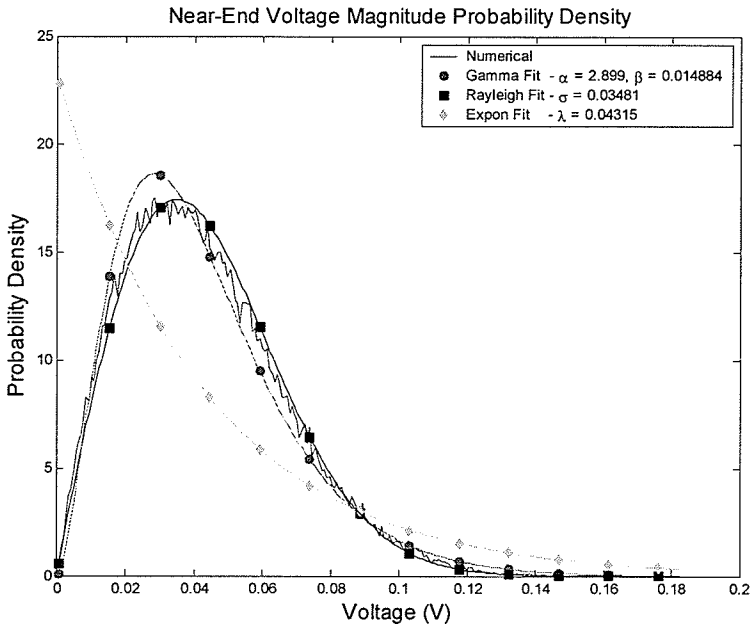

Figure 4-37. MLE fit for 3-D multiple sources - Setup B - 5 waves

Once again, even though the terminations are unmatched, the Rayleigh distribution is a very good fit at 5 waves. The exactness of the fit is best expressed by the CDF of the density as shown in Fig. 4-38 which shows that the Rayleigh distribution is nearly an exact match.

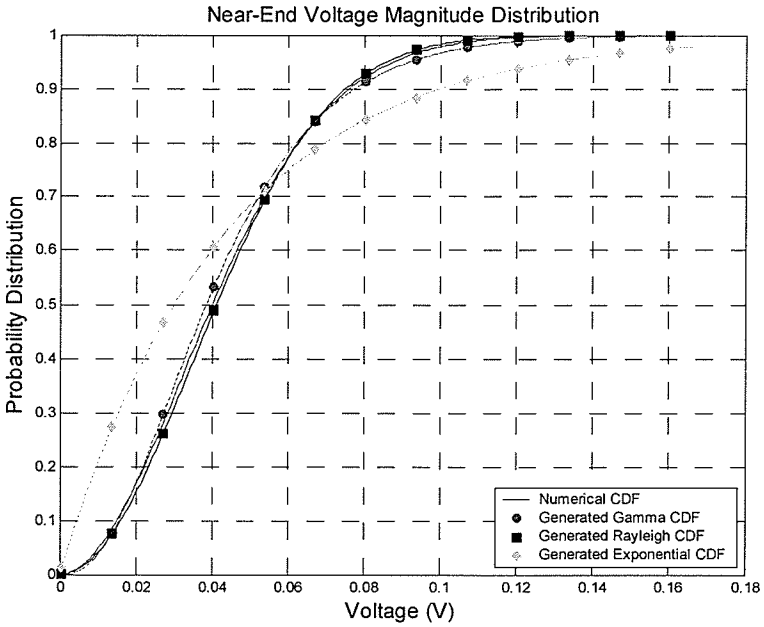

Figure 4-38. CDF for 3-D multiple sources - Setup B - 5 waves

The resulting fits of N waves in three-dimensions are more useful than those of a single wave in three-dimensions. It has been showed that for small mismatches, Rayleigh distributions could be used to accurately model the termination voltages provided a sufficient number of statistically independent waves is present.

4.8.4 Fitting to the Two-Dimensional Multiple Source Problem

Considering the same two physical configurations as in the three-dimensional case, a horizontal source location for the matched case with 2 and 5 waves results in the densities of Fig. 4-39 and Fig. 4-40.

Table 4-29. 2-D Multiple Source Fit - Setup A

Frequency	**Field Strength**	**Length**	**Separation**	***k***	Z_c	Z_0/ρ_0	Z_L/ρ_L
100 kHz	10 V/m	30 m	0.1 m	0.002	100	100/0	100/0

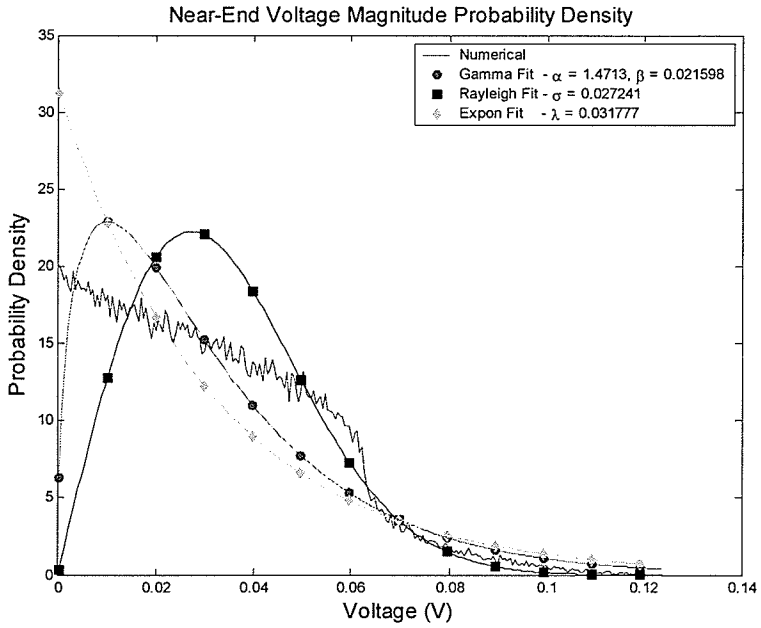

Figure 4-39. MLE fit for 2-D multiple sources - Setup A- 2 waves

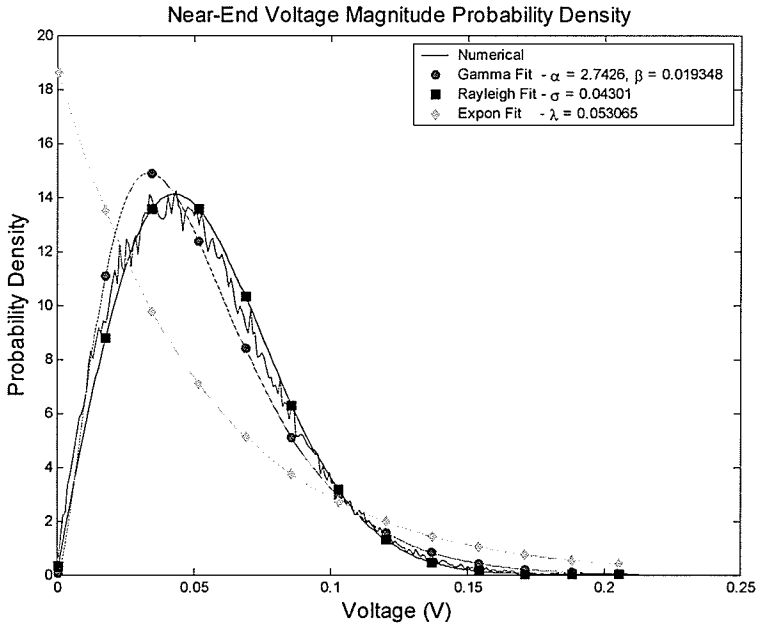

Figure 4-40. MLE fit for 2-D multiple sources - Setup A - 2 waves

In two-dimensions, the fit for two waves is noticeably worse than that in three-dimensions. At 5 waves however, the Rayleigh distribution is once again a very good fit. When the same load mismatches are considered as in the three-dimensional case, the results are:

Table 4-30. 2-D Multiple Source Fit - Setup B

Frequency	Field Strength	Length	Separation	k	Z_c	Z_0/ρ_0	Z_L/ρ_L
100 kHz	10 V/m	30 m	0.1 m	0.002	100	75/-0.14	95/-0.026

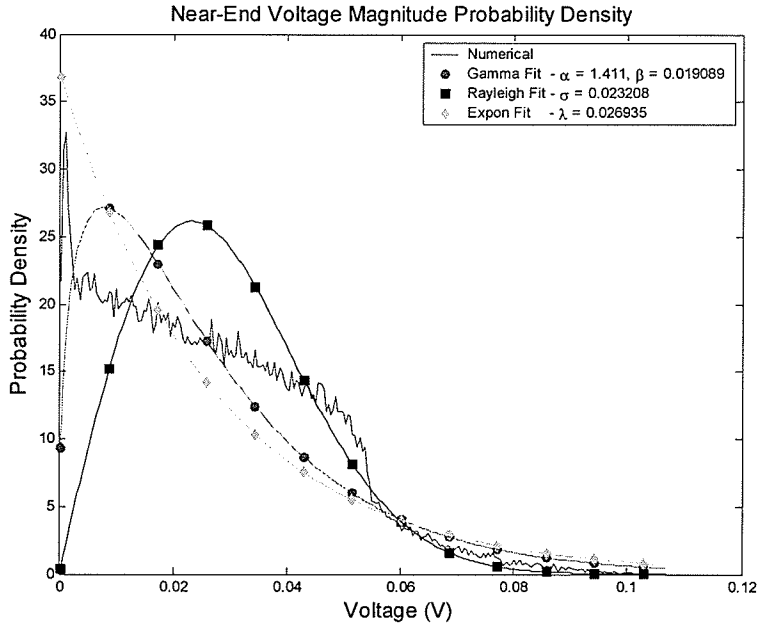

Figure 4-41. MLE fit for 2-D multiple source - Setup B - 2 waves

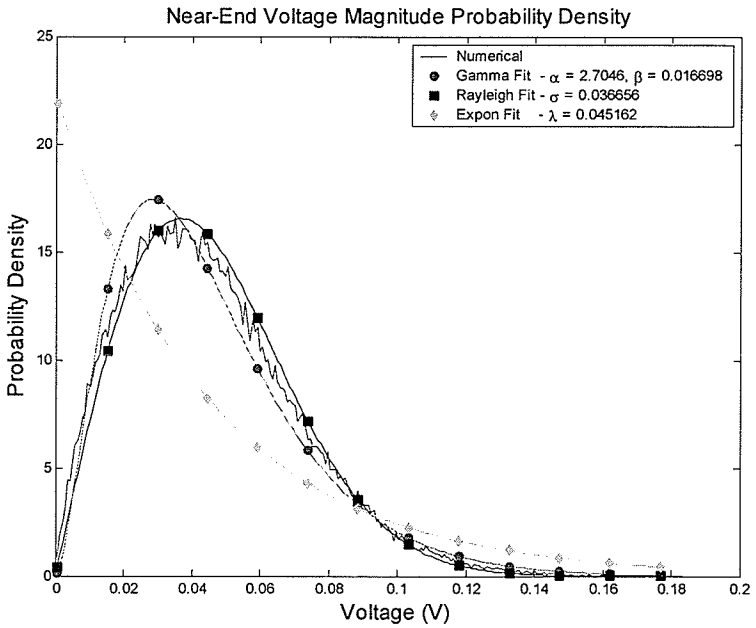

Figure 4-42. MLE fit for 2-D multiple source - Setup B - 5 waves

Once again, a Rayleigh fit is very close provided a sufficient number of waves is present.

4.9 SUMMARY

In this chapter, numerical analysis of the voltage densities at the terminations of a transmission-line arising due to stochastic plane wave coupling have been presented. In general, it seems that only Monte Carlo analysis will give an accurate picture of the voltage densities when the transmission line is unmatched. However, in the case of matched lines, a Rayleigh distribution seems to be a very accurate fit when numerous plane waves are considered. In the case of a single plane wave with deterministic magnitude with matched loads, none of the densities considered accurately match the numerical results. Only if sufficient uncertainty is present in the field strength does the voltage density approach an exponential or gamma distribution. In all single source cases, the phase has been shown to be uniformly distributed over the range $(-\pi, \pi)$.

CHAPTER 5. FUNCTIONS OF RANDOM VARIABLES

The work of Chapter 4 on determining approximate MLE fit densities of the load and source voltage magnitudes resulting from the coupling of stochastic plane waves to a deterministic transmission line failed in many cases. Specifically, for a deterministic field value and matched loads, the considered density fits give a very poor approximation to the actual numerical curve (as shown in Fig. 4-27). Therefore, the remainder of this research is concerned with determining analytic distributions to the BLT solution in the special case of matched loads where the field is assumed to be monochromatic with a deterministic magnitude.

This chapter presents the necessary theory for finding analytic density functions for the BLT solution by considering the BLT equations to be functions of random variables. As a result of the presented theory, it will become apparent that in most, if not all cases, determining an analytic density function is too complicated to be feasible. The probability theory and techniques discussed are well known and are taken extensively from the literature.

In Chapter 6, the developed theory is applied the horizontal incidence problem of Chapter 4 for matched loads, and a single source having a deterministic frequency and field magnitude.

5.1 THE BLT SOLUTION: A FUNCTION OF RANDOM VARIABLES

Consider the BLT solution to the plane-wave coupling problem:

$$\begin{bmatrix} V(0) \\ V(l) \end{bmatrix} = \frac{1}{2(\rho_0\rho_l - e^{2jkl})} \begin{bmatrix} (1+\rho_0)(-\rho_l)S_1 + (1+\rho_0)(-e^{jkl})S_2 \\ (1+\rho_l)(-e^{jkl})S_1 + (1+\rho_l)(-\rho_0)S_2 \end{bmatrix} \tag{5.1}$$

$$\begin{bmatrix} S_1 \\ S_2 \end{bmatrix} = -Ed \begin{bmatrix} \left(\frac{\cos\theta(\cos\theta\cos\phi\cos\zeta - \sin\phi\sin\zeta)}{1 + \sin\theta\cos\phi} + \sin\theta\cos\zeta \right)(e^{(1+\sin\theta\cos\phi)jkl} - 1) \\ e^{jkl}\left(\frac{\cos\theta(\cos\theta\cos\phi\cos\zeta - \sin\phi\sin\zeta)}{1 - \sin\theta\cos\phi} - \sin\theta\cos\zeta \right)(e^{(-1+\sin\theta\cos\phi)jl} - 1) \end{bmatrix} \tag{5.2}$$

From the equations it is apparent that the voltage at the line terminations is an algebraic and transcendental function of the stochastic parameters θ, ϕ, ζ, k and E. Therefore, this chapter is devoted to introducing the appropriate mathematical foundation for determining the probability density function of the near- and far-end voltage as given by Eq 5.1 and Eq 5.2 through transforms of random variables. The development of the theory is borrowed heavily from [22] and [26]. It is still assumed that the reader is familiar with the basic concepts of random variables and distributions of random variables. A brief review of these concepts is presented in Appendix C.

5.2 Determining the Density of a Monotonic Function of a Random Variable

The BLT solution contains sines and cosines of the angles of incidence and polarization. To simplify the equation, it would be convenient to replace all of the trigonometric functions with new random variables with known probability density functions. Therefore, methods for determining the distribution of a function of a single random variable are required. This is first demonstrated for the case of a monotonic function next, and fully developed for any arbitrary function in section 5.3.

Consider a random variable $\boldsymbol{y}$ related to a RV $\boldsymbol{x}$ with known density $f_x(X)$ by the function g.

$$\boldsymbol{y} = g(\boldsymbol{x}) \tag{5.3}$$

In order to determine the statistics of $\boldsymbol{y}$ from the density $f_x(X)$ it is first assumed that the function of interest $g(\boldsymbol{x})$ relates the random variables $\boldsymbol{x}$ and $\boldsymbol{y}$ in a monotonically increasing *or* decreasing way.

Determining $f_y(Y)$ is most easily accomplished by considering the CDF $F(Y)$ of the RV $\boldsymbol{y}$. By definition, $F(Y) = P\{\boldsymbol{y} \le Y\} = P\{g(\boldsymbol{x}) \le Y\}$ and since the function in question is either monotonically increasing or decreasing, an inverse function g^{-1} exists uniquely. Therefore:

1) If the situation is such that g is monotonically *increasing* then the CDF of $\boldsymbol{y}$ is related directly to the CDF of $\boldsymbol{x}$ as $F(Y) = P\{X \le g^{-1}(Y)\} = F_x[g^{-1}(Y)]$. Differentiating the CDF yields:

$$f_y(Y) = \frac{d}{dY}F_x[g^{-1}(Y)] = f_x[g^{-1}(Y)]\frac{d}{dY}|g^{-1}(Y)|. \tag{5.4}$$

In this case the derivative of g^{-1} is always positive. The absolute value sign has been added for convenience when considering the monotonically decreasing case.

2) If the case is that g is monotonically *decreasing* then the CDF of $\boldsymbol{y}$ is related directly to the CDF of $\boldsymbol{x}$ as $F(Y) = P\{X > g^{-1}(Y)\} = 1 - F_x[g^{-1}(Y))]$. Differentiation of the CDF results in:

$$f_y(Y) = \frac{d}{dY}(1 - F_x[g^{-1}(Y)]) = -f_x[g^{-1}(Y)]\left(\frac{d}{dy}g^{-1}(Y)\right), \tag{5.5}$$

but in this case the derivative is always negative making Eq 5.4 also applicable (the point of including the absolute value sign). Finally, Eq 5.4 may be simplified noting that $\dfrac{dg^{-1}(Y)}{dY} = \left.\dfrac{1}{dg(R)/dR}\right|_{R = g^{-1}(Y)}$ resulting in:

$$f_y(Y) = \left.\frac{f_x(R)}{|dg(R)/dR|}\right|_{R = g^{-1}(Y)} \tag{5.6}$$

The use of the variable R in Eq 5.6 is selected as it represents the concept of a *root* of the function $Y = g(X)$ for a given value of Y. In the case that the function is monotonically increasing or decreasing, any given value of Y has a single root given by $R = g^{-1}(Y)$. In summary, calculating the density of a monotonic function of a single RV $\boldsymbol{x}$ simply requires evaluation of the density $f(X)$ at the root of the function for any $\boldsymbol{y} = g(\boldsymbol{x})$ divided by the absolute value of the derivative of the function evaluated at the same root. Note that in the monotonic case, the derivative of the function with respect to the root is equivalent to the derivative with respect to X.

5.3 AN ARBITRARY FUNCTION OF A RANDOM VARIABLE

Having solved for the density of a monotonic function of a RV, a natural extension to determining densities of arbitrary functions of a RV would be to break up the function into monotonically decreasing or increasing regions and apply Eq 5.6 to each region in order to obtain $f(Y)$.

We consider the function $\boldsymbol{y} = g(\boldsymbol{x})$ where $\boldsymbol{y}$ can be broken up into N monotonically increasing or decreasing sections $(X_1, X_2)\ldots(X_i, X_{i+1})\ldots(X_{N-1}, X_N)$ over the range of $\boldsymbol{x}$. In each region of monotonicity (X_i, X_{i+1}) there will exist a single root R_i. Then, the total density of $\boldsymbol{y}$ $f(Y)$ can be determined as

$$f_y(Y) = \sum_{i=0}^{N} \left. \frac{f_x(R_i)}{\left| dg(R_i)/dR_i \right|} \right|_{R = g^{-1}(Y)} \tag{5.7}$$

It will become clear through examples that care must be taken in the evaluation of Eq 5.7. Specifically, the range of $\boldsymbol{y}$ corresponding to different monotic sections of $\boldsymbol{x}$ will ultimately be different for each monotonic section. For example, a monotonic region

(X_1, X_2) under transformation may contribute to a range (Y_a, Y_c) while a monotonic region (X_i, X_{i+1}) may contribute to a range (Y_b, Y_c) where $a < b < c$. For preciseness Eq 5.7 should be written as

$$f_y(Y \in \{g(X_i), g(X_{i+1})\}) = \sum_{i=0}^{N} \left. \frac{f_x(R_i)}{|dg(R_i)/dR_i|} \right|_{R = g^{-1}(Y)} \tag{5.8}$$

in order to remove any ambiguity.

5.4 THREE USEFUL, ILLUSTRATIVE EXAMPLES

The following examples illustrate the application of the theory of functions of a single random variable. They have been selected based on their presence in Chapter 6 when an approximate solution to the BLT equation is attempted.

5.4.1 Example 1

Consider the function

$$\boldsymbol{y} = \sin(\boldsymbol{x}) \tag{5.9}$$

where $\boldsymbol{x}$ is assumed to be uniformly distributed over the range of $(0, 2\pi)$ such that $f_x(X) = 1/(2\pi)$. In this interval, the sine function has exactly two inverses (corresponding to two monotonic regions) and Eq 5.8 becomes:

$$f_y(Y) = \frac{2/(2\pi)}{\cos(\sin^{-1}(Y))} \tag{5.10}$$

Using the usual identity that $\cos(\sin^{-1}(x)) = \sqrt{1 - x^2}$ the total density is found to be

$$f_y(Y) = \frac{1}{\pi\sqrt{1-(Y)^2}} \tag{5.11}$$

A Monte Carlo simulation is compared to the analytic density in Fig. 5-1.

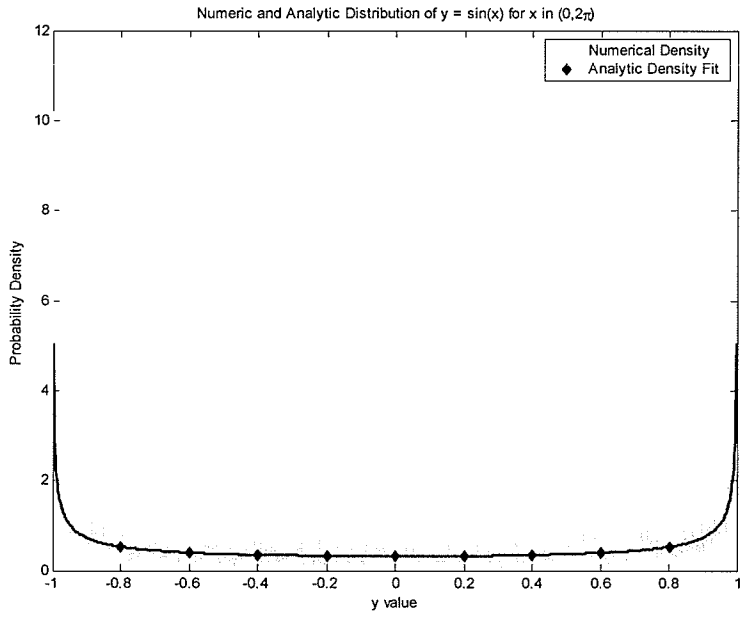

Figure 5-1. Analytic solution for the density of y=sin(x), the simple case

5.4.2 Example 2

Consider the function of Eq 5.9 where now, $\boldsymbol{x}$ is assumed to be uniformly distributed over the range of $(0, a)$ such that $f_x(X) = 1/a$. Unfortunately, based on the range of $\boldsymbol{x}$ this is a much more complicated problem. It is first assumed that there are n complete intervals of length π in the range of $(\pi/2, a)$ plus a remainder interval r whose length is less than π such that $a = n\pi + r + \pi/2$. (The range $(\pi/2, a)$ is assumed since the sine function has a unique inverse on any interval $(k\pi/2, (k+2)\pi/2)$). Then, each of

the n regions of length π in maps uniquely through the sine function to the interval $(-1, 1)$. Denoting the partial probability density of $\boldsymbol{y}$ due to these n intervals by $f_{yn}(Y)$ it is clear from Example 1 that:

$$f_{yn}(Y) = \frac{n}{a\sqrt{1-(y)^2}} \tag{5.12}$$

Considering now the region from $(0, \pi/2)$ there are two possibilities. If $a > \pi/2$ (such that either $n \neq 0$ or $r \neq 0$), this region will map uniquely through the sine function to the interval $(0, 1)$ and add to the partial density $f_{yn}(Y)$ in that region. If however, $a < \pi/2$ (such that $n = 0$), this region will account in total for the density of y and will be mapped to the region $(0, \sin(a))$. Summarizing to this point:

$$f_y(Y) = \frac{1}{a\sqrt{1-Y^2}} \qquad Y \in (0, \sin(a)) \qquad a < \pi/2$$

$$f_{yn2}(Y) = \begin{cases} \dfrac{n+1}{a\sqrt{1-(Y)^2}} & Y \in (0, 1) \\ \dfrac{n}{a\sqrt{1-(Y)^2}} & Y \in (-1, 0) \end{cases} \qquad a > \pi/2 \tag{5.13}$$

where in the first case, $f_y(Y)$ represents the total density while in the second case, $f_{yn2}(Y)$ represents the partial density as contributed to by the n intervals in addition to the interval $(0, \pi/2)$.

Finally, considering the region r there are now four possibilities since the region to which the sine function maps the interval $(\pi/2 + n\pi, a)$ is dependent on the value of n. For example, if n is even and $r < \pi/2$, the region from $n\pi$ to a will be mapped into the interval $(1, \sin(a))$ and the resulting distribution will be:

$$f_y(Y) = \begin{cases} \dfrac{n+2}{a\sqrt{1-(Y)^2}} & Y \in (\sin(a), 1) \\ \dfrac{n+1}{a\sqrt{1-(Y)^2}} & Y \in (0, \sin(a)) \\ \dfrac{n}{a\sqrt{1-(Y)^2}} & Y \in (-1, 0) \end{cases} \tag{5.14}$$

This is illustrated in the figure below for the case of $a = 9$ such that $n = 2$ and $r = 1.146$.

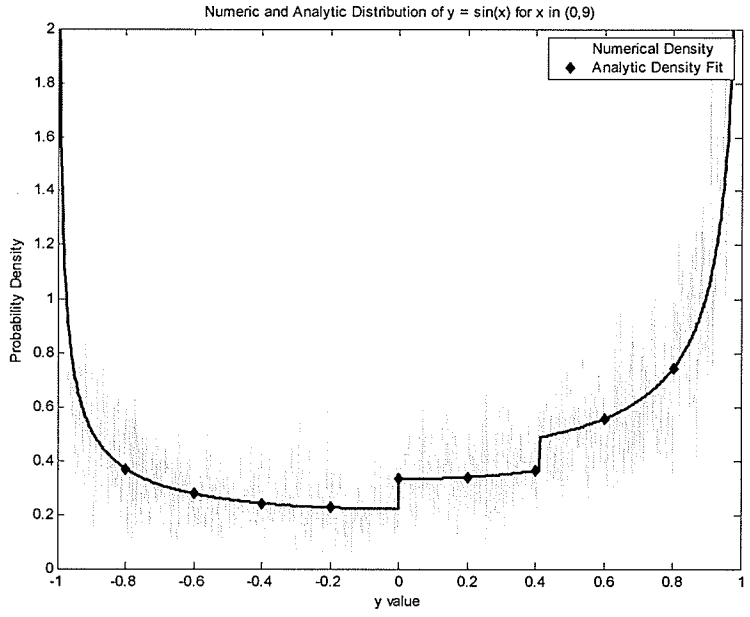

Figure 5-2. Analytic solution for the density of y=sin(x), the complicated case

If instead, n is even and $r > \pi/2$, there will be additional density on the interval from $(0, \sin(a))$ where the $\sin(a)$ in this case is a negative value and of course, it is possible that n is odd or that $n = 0$ and $r \neq 0$. Each case results in a different density function having multiple discontinuities. What is very interesting is that, in many cases, Monte Carlo analysis may not accurately show discontinuities arising in distributions such as the

discontinuities of Fig. 5-2. It seems that this is a benefit of the analytic approach. Unfortunately, due to the complicated nature of these transformations, approximate distributions may be required as will be demonstrated in Chapter 6.

5.4.3 Example 3

Consider the linear transformation

$$\boldsymbol{y} = a\boldsymbol{x} + b, \tag{5.15}$$

Since the function is monotonic, the density of $\boldsymbol{y}$ is obtainable directly from the density of $\boldsymbol{x}$ by Eq 5.4:

$$f_y(Y) = \frac{1}{|a|} f_x\left(\frac{Y-b}{a}\right). \tag{5.16}$$

5.5 A SINGLE FUNCTION OF MULTIPLE RANDOM VARIABLES

Having dealt with the problem of determining the distribution of a random variable that is a function of a single random variable with known distributions, substitution of $x = \cos\theta, y = \cos\phi$ $u = \sin\theta$ $v = \sin\phi$ and $a = \cos\zeta$ $b = \sin\zeta$ into Eq 5.2 allows the source terms to be written as:

$$\begin{bmatrix} S_1 \\ S_2 \end{bmatrix} = Ed\begin{bmatrix} \left(\frac{x(xya - vb)}{1+uy} + ua\right)\left(e^{(1+uy)jkl} - 1\right) \\ e^{jkl}\left(\frac{x(xya - vb)}{1-uy} - ua\right)\left(e^{(-1+uy)l} - 1\right) \end{bmatrix} \tag{5.17}$$

where the distributions of a, b, x, y, u, v are known. Therefore, to solve for the voltage distribution, it is required to determine the distribution of a function of many random variables. This is considered next for the simplified case of two random variables which can readily be extended to any number of random variables.

Given the function $\boldsymbol{u} = g(\boldsymbol{x}, \boldsymbol{y})$ it is convenient to visualize the outcomes of events geometrically using the cartesian plane in two dimensions. The region in the XY plane where $U < g(\boldsymbol{x}, \boldsymbol{y}) \leq U + dU$ is denoted as Δ_u such that

$$\{U < \boldsymbol{u} \leq U + dU\} = \{(X, Y) \in \Delta_u\} \tag{5.18}$$

By definition, the density of $\boldsymbol{u}$ is related to the probability of experimental outcomes by:

$$f_u(U)dU = P\{U < \boldsymbol{u} \leq U + dU\}. \tag{5.19}$$

and so the probability $P\{U < \boldsymbol{u} \leq U + dU\}$ is directly related to the area Δ_u and the bivariate density of $\boldsymbol{x}$ and $\boldsymbol{y}$ by:

$$P\{U < \boldsymbol{u} \leq U + dU\} = \{(\boldsymbol{x}, \boldsymbol{y}) \in \Delta_u\} = \int_{\Delta_u} \int f_{xy}(X, Y)dXdY \tag{5.20}$$

From the last result the useful relation of Eq 5.21 is obtained:

$$f_u(U)dU = \int_{\Delta_u} \int f_{xy}(X, Y)dXdY \tag{5.21}$$

Clearly, in order to determine the probability $P\{U < \boldsymbol{u} \leq U + dU\}$ it is required to integrate the bivariate distribution $f_{xy}(X, Y)$ over the suitable region Δ_u. This procedure is now demonstrated for the sum and product of two random variables.

5.5.1 The Distribution of the Sum of Two Random Variables

Given that a RV $\boldsymbol{u}$ is the sum of two random variables $\boldsymbol{x}$ and $\boldsymbol{y}$:

$$\boldsymbol{u} = \boldsymbol{x} + \boldsymbol{y}. \tag{5.22}$$

the region in the XY plane such that $\{U < \boldsymbol{x} + \boldsymbol{y} \leq U + dU\}$ is obtained by considering lines of constant U:

$$\begin{aligned} Y &= U - X \\ Y &= U + dU - X \end{aligned} \tag{5.23}$$

represented geometrically in the Cartesian plane in Fig. 5-3. Any location (X, Y) corresponds to coordinates $(U - Y, Y)$ and inside the region Δ_u, an area element $dA = dXdY$ can be shown to be $dA = dXdY = dUdY$. In this manner, the X coordinate has been eliminated and it is a judicious choice to integrate both sides of Eq 5.21 by selecting horizontal strips and performing vertical integration (with respect to Y). Then $f_u(U)dU$ in Eq 5.21 becomes:

$$f_u(U)dU = \int f_{xy}(U - Y, Y)dYdU \tag{5.24}$$

where the limits of integration are selected based on the region of existence of the bivariate distribution $f_{xy}(X, Y)$.

As the integration is with respect to Y the differentials dU cancel from both sides to obtain the final expression for the density of $\boldsymbol{u}$:

$$f_u(U) = \int f_{xy}(U - Y, Y)dY \tag{5.25}$$

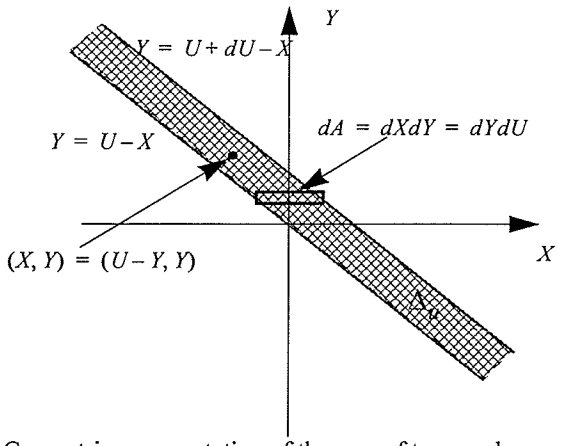

Figure 5-3. Geometric representation of the sum of two random variables

5.5.2 The Distribution of the Product of Two Random Variables

Given that a RV $\boldsymbol{u}$ is a function of two random variables $\boldsymbol{x}$ and $\boldsymbol{y}$ given by:

$$\boldsymbol{u} = \boldsymbol{xy}. \tag{5.26}$$

The region in the XY plane such that $\{U < \boldsymbol{xy} \leq U + dU\}$ is obtained by considering curves of constant U represented geometrically in Fig. 5-4:

$$\begin{aligned} Y &= \frac{U}{X} \\ Y &= \frac{U + dU}{X} \end{aligned} \tag{5.27}$$

Any location (X, Y) corresponds to coordinates $(U/Y, Y)$ and an area element dA can be shown to be $dA = dXdY = 1/|Y|dUdY$. As the X coordinate has been eliminated, it is once again a judicious choice to integrate both sides of Eq 5.21 by selecting horizontal strips and performing vertical integration. The quantity $f_u(U)dU$ becomes:

$$f_u(U)dU = \int \frac{1}{|Y|} f_{xy}\left(\frac{U}{Y}, Y\right) dY dU \ . \tag{5.28}$$

As the integration is with respect to Y the differentials dU cancel to obtain the final formula for the density of $\boldsymbol{u}$:

$$f_u(U) = \int \frac{1}{|Y|} f_{xy}\left(\frac{U}{Y}, Y\right) dY \ . \tag{5.29}$$

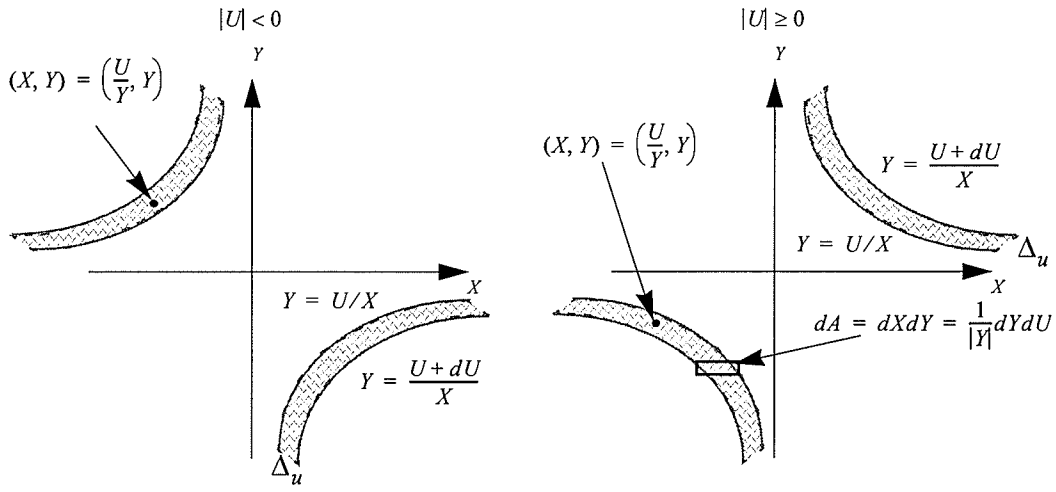

Figure 5-4. Geometric representation of the product of two random variables

In a similar manner, it is possible to obtain the solution to the density of a quotient of two random variables.

It seems that all the necessary tools have been discussed for determining the voltage density of the BLT solution. There are however, two large complications. The first deals with the bounded nature of the random variables. For example, in the case of the sum of two random variables, Eq 5.25 gives the desired distribution where the limits of integration must be appropriately set based on the existence of the bivariate distribution.

This is simple in the case that both $\boldsymbol{x}$ and $\boldsymbol{y}$ have infinite support such that the bivariate distribution is continuous in the XY plane. In this case, the limits of integration are from $-\infty$ to ∞.

If however, the random variables of interest are bounded in a region, the situation is much different. Assuming that $\boldsymbol{x}$ is uniformly distributed on the interval (a, b) and $\boldsymbol{y}$ is uniformly distributed on the interval (c, d) (assuming for convenience $d > b$ and $a, b, c, d > 0$) then the required area of integration becomes the square region bounded by the limits of the random variable distributions as shown in Fig. 5-5 It is immediately obvious that the limits of integration vary depending on the value of $\boldsymbol{u}$.

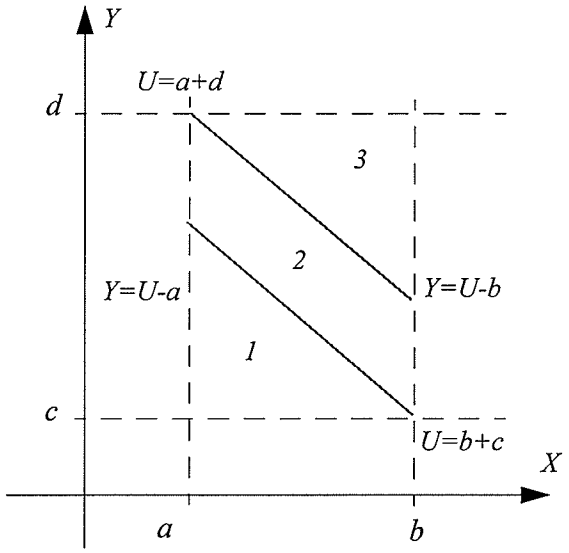

Figure 5-5. Geometric representation of the sum of two bounded random variables

As apparent in the figure, the initial integration limits in region *1* are from $Y = c$ to the intersection point with the bounding line $X = a$ (which gives a value of $Y = U - a$). As b has been assumed to be less than c, the limits of integration change when $U = b + c$ (region *2*). Now the limits must be from $Y = U - b$ to $Y = U - a$. Finally, the limits change again at $U = d + a$ (region *3*) becoming from $Y = U - b$ to $Y = d$. For this very simple problem, there are 3 regions of integration all of which could potentially result in very different densities. And this is only the case for $d > b$!

Similar changes of integration limits arise when attempting to determine the distribution of any function of more than one random variable when any or all of the random variables are bounded. The immediate implication is that perhaps it is not wise to assume bounds on the random variables. The complications that arise for simple functions like addition imply that for more difficult problems (such as the BLT solution) the arising distributions will be very complicated (and indeed this has been shown in Chapter 4). Unfortunately, the very nature of the BLT solution does not allow for distributions with infinite tails. Due to the transcendental functions the BLT solution contains, the distributions created by the polarization angle, angle of incidence or phase angle are all bounded. What is important from the results of this simple example is that the discontinuities of the densities found in Chapter 4 are explained by the changing limits of integration when dealing with functions of bounded random variables.

Additional complications also arise, namely the determination of the multivariate distributions of the random variables in the BLT Solution. Multivariate distributions are simply determined for the case of independent random variables, being simply the product of the respective marginal distributions. Unfortunately, in Eq 5.2, the pairs $(a, b), (u, v), (x, y)$ depend on each other as they are functions of the same random variable. In order to proceed it is necessary to determine the bivariate or multivariate distributions of dependent random variables.

5.6 The Bivariate Distribution of Two Dependent Random Variables

Consider two dependent random variables (DRVs) $\boldsymbol{u}$ and $\boldsymbol{v}$ taking values U and V respectively for any given experiment. If these DRVs are related to two independent random variables $\boldsymbol{x}$ and $\boldsymbol{y}$ (taking values X and Y respectively for a given experiment) by the functions g and h as

$$\begin{aligned} U &= g(X, Y) \\ V &= h(X, Y) \end{aligned} \tag{5.30}$$

In the case that X and Y are real, Eq 5.30 is a mapping of the Cartesian plane onto itself by means of the functions g and h. Specifically, the point (X, Y) in the Cartesian plane is mapped to a point (U, V) in the Cartesian plane by the rules $U = g(X, Y)$ and $V = g(X, Y)$. An obvious point of interest is the existence of the inverse functions $g^{-1}(\cdot)$ and $h^{-1}(\cdot)$ such that given a point (U, V) it is possible to determine form which point (X, Y) it was transformed:

$$\begin{aligned} X &= g^{-1}(U, V) \\ Y &= h^{-1}(U, V) \end{aligned} \tag{5.31}$$

If the inverse functions exist then the functions $g(X, Y)$ and $h(X, Y)$ transform regions in the real plane to regions in the real plane in a one-to-one manner, a result that is beneficial when dealing with bivariate distributions of functions of dependent random variables.

It is the Jacobian of the transformation that determines the existence of the inverse functions. Given the two functions of Eq 5.30 the Jacobian $J(X, Y)$ is defined as the determinant:

$$J(X, Y) = \begin{vmatrix} \frac{\partial}{\partial X} g(X, Y) & \frac{\partial}{\partial Y} g(X, Y) \\ \frac{\partial}{\partial X} h(X, Y) & \frac{\partial}{\partial Y} h(X, Y) \end{vmatrix}. \tag{5.32}$$

For the inverse functions to exist, the Jacobian must be non-zero on the region Ω where $(X, Y) \in \Omega$. The existence of a non-zero Jacobian is assured by continuous first partial derivatives of $g(X, Y)$ and $h(X, Y)$ in the region of the transformation Ω, and in this case, the following results are obtained Eq 26:

1) If the transformation of any point $(X, Y) \in \Omega$ by the functions $g(X, Y)$ and $h(X, Y)$ map the region Ω to the region Ψ, then any point $(U, V) \in \Psi$ corresponds to a unique point $(X, Y) \in \Omega$ given by $X = g^{-1}(U, V)$, $Y = h^{-1}(U, V)$.

2) The inverse functions $g^{-1}(U, V)$ and $h^{-1}(U, V)$ exist and are continuous with continuous first partial derivatives.

When the Jacobian of the transformation Eq 5.30 exists and is non-zero in the region Ω it can be shown that the area of the region Ψ is related to the area of Ω by:

$$\iint_{\Omega} dXdY = \iint_{\Psi} |J_I(U, V)| dUdV, \tag{5.33}$$

where J_I is the Jacobian of the inverse transformation:

$$J_I(U, V) = \begin{vmatrix} \frac{\partial}{\partial U} g^{-1}(U, V) & \frac{\partial}{\partial V} g^{-1}(U, V) \\ \frac{\partial}{\partial U} h^{-1}(U, V) & \frac{\partial}{\partial V} h^{-1}(U, V) \end{vmatrix} \tag{5.34}$$

A formal proof requires the application of Green's Theorem and can be found on p256 in [27]. In addition the Jacobian of the forward transformation is related to that of the reverse transformation by:

$$J_I(U, V) = \frac{1}{J[g^{-1}(U, V), h^{-1}(U, V)]}. \tag{5.35}$$

It is apparent that the Jacobian of the inverse transformation required in the evaluation of Eq 5.33 is computable directly from the Jacobian of the forward transform. If one is continuous and non-zero in the region of interest, the other exists and is continuous with continuous partial derivatives over the region resulting from the transformation.

Having defined the inverse transformation and as a result, discovered the Jacobian, it becomes apparent how these concepts can be used to transform a bivariate density $f(X, Y)$ to the joint density $f(U, V)$ when (X, Y) and (U, V) are related by Eq 5.30. Considering the region of the mapping from Ω to Ψ where the mapping is one-to-one (that is the Jacobian exists and is non-zero), the joint density $f(X, Y)$ is assumed to be zero except over a region $\Omega_1 \subset \Omega$. If ω is any region in the XY plane, then $f(X, Y)$ is non-

zero for the region $\omega \cap \Omega_1$. The corresponding region in the UV plane is denoted $\psi \cap \Psi_1$ where ψ is any region in the UV plane and $\Psi_1 \subset \Psi$ is the region where $f(U, V)$ is non-zero. The transformation is unique since $\omega \cap \Omega_1 \subset \Omega$ and therefore the probabilities in these regions must be the same [26]:

$$\int_{\omega \cap \Omega_1} \int f_{xy}(X, Y)dXdY = \int_{\psi \cap \Psi_1} \int f_{uv}(U, V)dUdV. \tag{5.36}$$

As the Jacobian is assumed non-zero, the inverse transformation exists and using the results of Eq 5.33 relating the area of a region in the (X, Y) plane to an area of the transformed region in the (U, V) plane gives (from Eq 5.36):

$$\int_{\psi \cap \Psi_1} \int f_{xy}[g^{-1}(U, V), h^{-1}(U, V)]\left|J_J(U, V)\right|dUdV = \int_{\psi \cap \Psi_1} \int f_{uv}(U, V)dUdV. \tag{5.37}$$

and finally, a simple examination of the integrals under equality leads to the desired relation:

$$f_{uv}(U, V) = f_{xy}[g^{-1}(U, V), h^{-1}(U, V)]\left|J_J(U, V)\right| \tag{5.38}$$

From Eq 5.38 it is evident that the joint density of the dependent random variables $\boldsymbol{u}$ and $\boldsymbol{v}$ may be found directly from the joint density of the independent random variables $\boldsymbol{x}$ and $\boldsymbol{y}$. This is a very desirable result considering that the joint density of two independent random variables is simply the product of their respective marginal distributions. Although not presented herein, the problem of determining multivariate distributions of any number of random variables is a direct extension of the two-dimensional case [26].

Finally, all of the theory required for dealing with functions of random variables has been covered. Unfortunately, for the BLT solution, the three-dimensional case is too complicated to be approached analytically. Even the two-dimensional case with unmatched loads is much too complicated for numerous reasons. First, the cosines and sines of the random variables θ, ϕ and ζ do not map in a 1-to-1 fashion. Therefore, the

multi-variate distribution of these variables is complicated and difficult to obtain. Furthermore, even if the multivariate density function was determined, a three-dimensional visualization of the integration limits would be required which, in general, is not easy. Even in the case of horizontal incidence, if the loads are unmatched, a superposition of the terms S_1 and S_2 is required which would mean determining the bivariate distribution of S_1 and S_2. For these reasons, these more complicated problems are not attempted at this time. Instead, only the two-dimensional problem with matched terminations is considered in the next chapter.

CHAPTER 6. ANALYTIC AND EMPIRICAL RESULTS

Though not the three-dimensional problem of interest, the BLT solution simplifies significantly when the source terms are assumed to be incident from the horizon. Furthermore, as previously mentioned in Chapter 4, none of the considered distributions (Rayleigh, exponential, gamma) gave good approximations for a single wave impinging on a matched transmission line. Finally, this problem is a good model for various physical problems such as the fields of a radio station tower impinging on a power-line. Therefore, an analytic (or approximate analytic) solution to the horizontal, matched coupling case is desirable. As in Chapter 4, the source is assumed to be uniformly polarized over $(0, 2\pi)$ while the angle of incidence ϕ is assumed to be equally likely from any direction on the interval $(0, 2\pi)$. In this chapter, using the theory of Chapter 5, obtaining an approximate density function is attempted. Unfortunately, even with approximations, the resulting integrals do not provide convenient (if any) results. Therefore, the material is presented only to suggest the extreme difficulty of the problem. On the other hand, a very close empirical approximation to the desired density function was obtained and is presented in Section 6.2.

6.1 THE BLT EQUATION FOR INCIDENCE FROM THE HORIZON WITH MATCHED LOADS

From the general form of the BLT solution, selecting $\theta = \pi/2$, and $\rho_0 = \rho_l = 0$ gives:

$$\begin{bmatrix} S_1 \\ S_2 \end{bmatrix} = -Ed\cos(\zeta)\begin{bmatrix} (e^{(1+\cos\phi)jkl}-1) \\ e^{jkl}(e^{(-1+\cos\phi)jkl}-1) \end{bmatrix} \tag{6.1}$$

$$\begin{bmatrix} V(0) \\ V(l) \end{bmatrix} = -\frac{1}{2}\begin{bmatrix} (e^{-jkl})S_2 \\ (e^{-jkl})S_1 \end{bmatrix} \tag{6.2}$$

Substituting Eq 6.2 into Eq 6.1 gives relatively simple equations for the near- and far-end voltages:

$$\begin{bmatrix} V(0) \\ V(l) \end{bmatrix} = \frac{Ed\cos(\zeta)}{2}\begin{bmatrix} (e^{-jkl})(e^{(1+\cos\phi)jkl}-1) \\ (e^{(-1+\cos\phi)jkl}-1) \end{bmatrix} \tag{6.3}$$

where further simplification occurs by using the complex identity $\sin(x) = (e^{jx} - e^{-jx})/(2j)$:

$$\begin{bmatrix} V(0) \\ V(l) \end{bmatrix} = \frac{Ed\cos(\zeta)}{2}\begin{bmatrix} 2j(e^{-jkl})(e^{((1+\cos\phi)jkl)/2})\dfrac{(e^{((1+\cos\phi)jkl)/2}-e^{-((1+\cos\phi)jkl)/2})}{2j} \\ 2j\dfrac{(e^{((-1+\cos\phi)jkl)/2}-e^{-((-1+\cos\phi)jkl)/2})}{2j} \end{bmatrix} \tag{6.4}$$

The magnitude of the near- and far-end voltages are therefore:

$$\begin{bmatrix} |V(0)| \\ |V(l)| \end{bmatrix} = |Ed\cos(\zeta)|\begin{bmatrix} |\sin(((1+\cos\phi)kl)/2)| \\ |\sin(((-1+\cos\phi)kl)/2)| \end{bmatrix} \tag{6.5}$$

At this point, for simplicity, it is assumed that $|E|d = 1$ such that:

$$\begin{bmatrix} |V(0)| \\ |V(l)| \end{bmatrix} = |\cos(\zeta)|\begin{bmatrix} |\sin(((1+\cos\phi)kl)/2)| \\ |\sin(((-1+\cos\phi)kl)/2)| \end{bmatrix} \tag{6.6}$$

As it is assumed that all angles of ϕ are equally likely, the value of $(1+\cos\phi)kl$ takes values in the range $(0, kl)$ while $(-1+\cos\phi)kl$ exists from $(-kl, 0)$. It should be evident from the material in Chapter 5 that the *shape* of these two distributions will be the

same since $\sin(-x) = -\sin(x)$. Therefore, it is convenient to select both arguments as $(1 + \cos(\phi))kl$ (although of course, the voltage from a particular source location will not map to the same spot in the density function):

$$\begin{bmatrix} |V(0)| \\ |V(l)| \end{bmatrix} = |\cos(\zeta)| \begin{bmatrix} |\sin(((1 + \cos\phi)kl)/2)| \\ |\sin(((1 + \cos\phi)kl)/2)| \end{bmatrix} \tag{6.7}$$

From Eq 6.7 it is apparent that in order to determine the distribution of the load voltage when ζ and ϕ are random variables it is required to determine the product of the random variables $\boldsymbol{x}$ and $\boldsymbol{y}$ where:

$$\begin{aligned} \boldsymbol{x} &= |\cos(\zeta)| \\ \boldsymbol{y} &= |\sin(((1 + \cos\phi)kl)/2)| \end{aligned} \tag{6.8}$$

The approach taken to solving this function of two random variables is to determine the densities of $\boldsymbol{x}$ and $\boldsymbol{y}$ from the theory of functions of a single random variable and then to apply Eq 5.29 for the product of two random variables.

Beginning with $\boldsymbol{x} = \cos(\zeta)$, the resulting distribution is exactly that of Eq 5.11 since ζ is uniformly distributed on $(0, 2\pi)$:

$$f_x(X) = \frac{1}{\pi} \frac{1}{\sqrt{1 - X^2}}, \qquad x \in (-1, 1) \tag{6.9}$$

Now, taking the absolute value of $\boldsymbol{x}$ simply maps the region $(-1, 0)$ onto the region $(0, 1)$ giving:

$$f_x(X) = \frac{2}{\pi} \frac{1}{\sqrt{1 - X^2}}, \qquad X \in (0, 1) \tag{6.10}$$

To determine the distribution of $\boldsymbol{y}$ a step-by-step approach is taken. First let $\boldsymbol{a} = \cos(\phi)$. The resulting density is identical in form to Eq 6.9. Then, letting $\boldsymbol{b} = 1 + \boldsymbol{a}$ and applying Eq 5.16,

$$f_b(y) = \frac{1}{\pi}\frac{1}{\sqrt{1-(B-1)^2}}, \qquad B \in (0, 2) \tag{6.11}$$

Letting $\boldsymbol{c} = kl\boldsymbol{b}/2$ and once again applying Eq 5.16 gives:

$$f_c(C) = \frac{2}{kl\pi}\frac{1}{\sqrt{1-\left(\frac{2C}{kl}-1\right)}}, \qquad C \in (0, kl) \tag{6.12}$$

The final step is to let $\boldsymbol{y} = |\sin(\boldsymbol{c})|$. It is immediately evident from the results of Example 2 in Section 5.4 of Chapter 5 that taking the sine of $\boldsymbol{c}$ is a very complicated operation given the value of kl (and is even more complicated than the example where a uniform distribution was selected because here, the distribution is governed by Eq 6.12). Through experience with working with functions of random variables, a suitable approximation for the case of $kl > \pi$ was found to be

$$f_{yapprox} = \frac{1}{\pi}\frac{1}{\sqrt{1-(Y-1)^2}} \qquad y \in (0, 1) \tag{6.13}$$

The approximate distribution is shown in Fig. 6-1 for the case of $k = 1.26$ (60 MHz source) and $l = 20$:

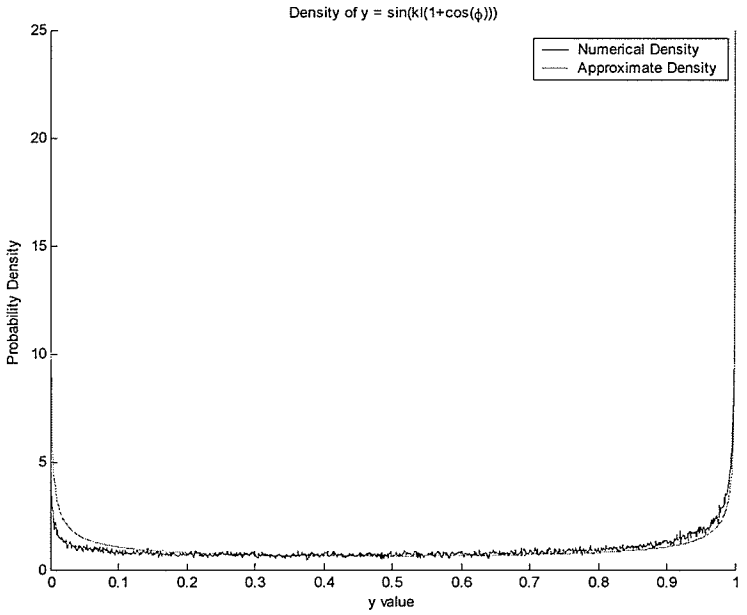

Figure 6-1. First approximation to the density of the random variable y

With this approximation, the distribution of the voltage can be calculated using Eq 5.29 as:

$$f_{|V|} = \int \frac{1}{|Y|} \frac{1}{\sqrt{1-(Y-1)^2}} \frac{1}{\sqrt{1-\left(\frac{|V|}{Y}\right)^2}} \tag{6.14}$$

where the limits of integration can be obtained by considering the curves of integration over the square of probability in Fig. 6-2. From the figure it is apparent that only one region of integration exists where the limits of integration are from $|V|$ to 1. Therefore, the voltage density is given as:

$$f_{|V|} = \int_{|V|}^{1} \frac{1}{Y} \frac{1}{\sqrt{1-(Y-1)^2}} \frac{1}{\sqrt{1-\left(\frac{|V|}{Y}\right)^2}} \tag{6.15}$$

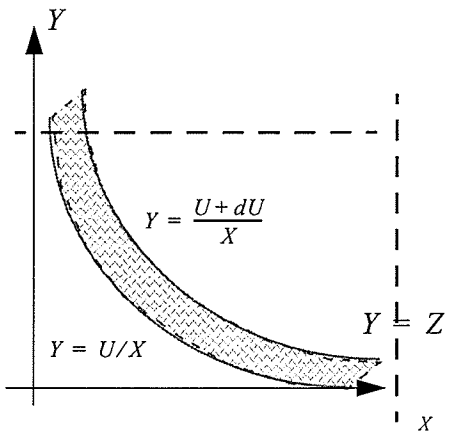

Figure 6-2. Bounded region of integration for the product xy

In this case, no useful solution to the integral could be found (although Mathematica offers a combination of elliptic functions that is rather amusing).

Another attempt to find an approximate density function was made by using a different approximation for the random variable $\boldsymbol{y}$. Instead of the approximate density of Eq 6.2, the density:

$$f_{yapprox} = \frac{1}{\pi}\frac{1}{\sqrt{1-Y^2}} \qquad y \in (0, 1) \tag{6.16}$$

can be assumed which holds if $kl > \pi$. Fig. 6-3 shows the approximation for a 60 MHz source and a line-length of 20 m.

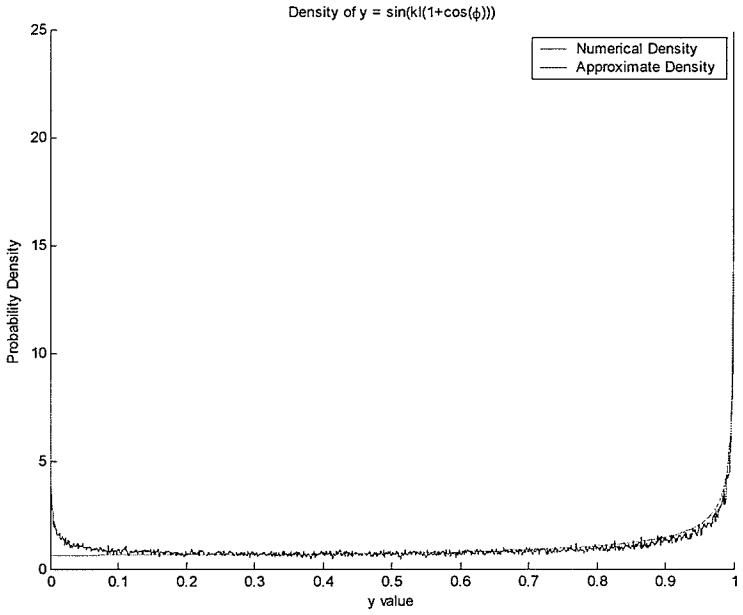

Figure 6-3. Second approximation to the density of the random variable y

Essentially, this approximation undershoots the distribution for low values of y but is an accurate fit at higher values. With this approximation, the resulting integral for the voltage density becomes:

$$f_{|V|} = \int_{|V|}^{1} \frac{1}{Y} \frac{1}{\sqrt{1-(Y)^2}} \frac{1}{\sqrt{1-\left(\frac{|V|}{Y}\right)^2}} \tag{6.17}$$

but once again, the only solution to the integral was found using Mathematica as a combination of Elliptic functions. Although each of these approximations can be numerically integrated to yield a close fit to the voltage magnitude density function, this does not assist in determining a closed-form expression capable of describing the random nature of the problem. At this point, an empirical approach was taken.

6.2 AN EMPIRICAL SOLUTION

While the lack of analytic results is frustrating, having obtained a very good working knowledge of the distributions arising from the transformations of random variables it was found that for the problem of a single field incident from the horizon ($\theta = \pi/2$) on a matched transmission-line, the resulting termination voltage probability density function could be approximated as having the same shape as the sine of a uniform random variable, appropriately shifted and scaled. That is:

$$f_{|V|} \approx \frac{2}{\pi} \frac{1}{\sqrt{1-(|V|-1)^2}} \qquad |V| \in (0,1) \qquad \text{if } (kl > \pi)$$

$$f_{|V|} \approx \frac{2}{\pi|\sin(kl)|} \frac{1}{\sqrt{1-\left(\frac{|V|}{|\sin(kl)|}-1\right)^2}} \qquad |V| \in (0,|\sin(kl)|) \qquad \text{if } (kl < \pi) \tag{6.18}$$

The results of this fit for the two-dimensional case are shown below in Fig. 6-4 for a 100 kHz source and in Fig. 6-5 for a 60 MHz source.

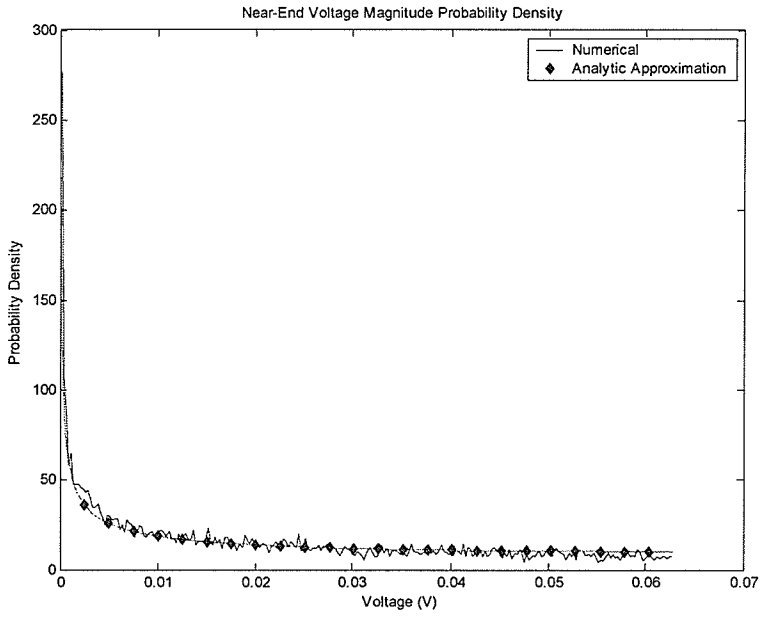

Figure 6-4. Empirical low-frequency fit for the two-dimensional matched problem

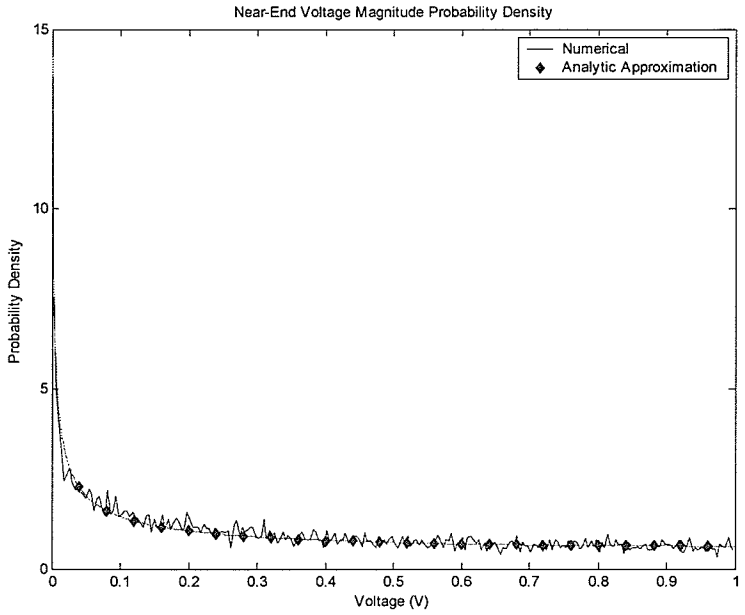

Figure 6-5. Empirical high-frequency fit for the two-dimensional matched problem

The accuracy of the fit is obtained by considering the CDF of the resulting distributions as shown in Fig. 6-6 for the 60 MHz source. Although not perfect, the fit is very good at describing the probability density of the voltage magnitude.

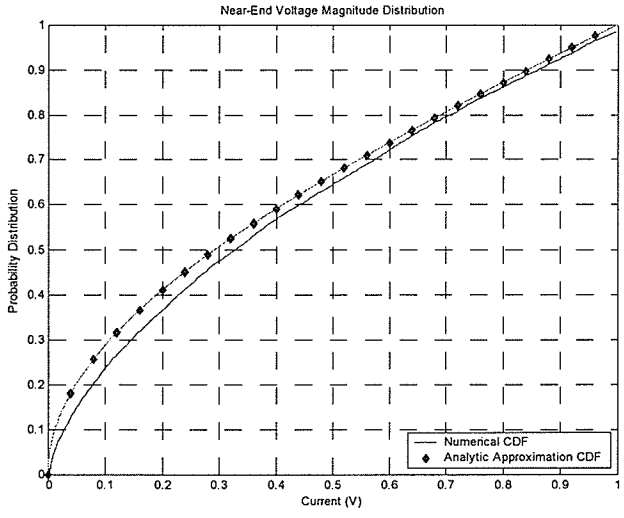

Figure 6-6. CDF of empirical and numerical results for the high-frequency case

In addition, the same empirical density function actually holds well for the case of matched-loads in three-dimensions provided the kl product is sufficiently high as shown in Fig. 6-7.

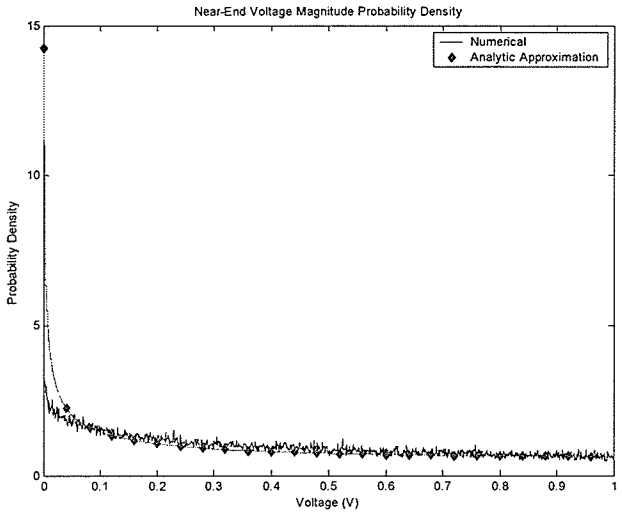

Figure 6-7. Empirical high-frequency fit for the three-dimensional matched problem

Unfortunately, for low frequencies (low kl product) in the three-dimensional case, the empirical density function is much less accurate as shown in Fig. 6-8.

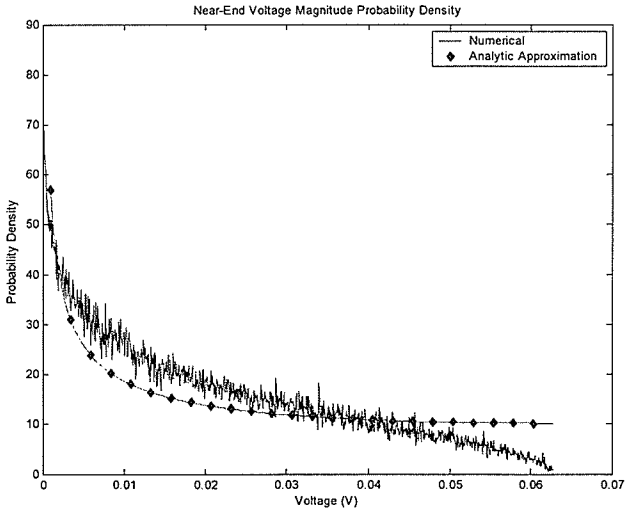

Figure 6-8. Empirical low-frequency fit for the three-dimensional matched problem

6.3 SUMMARY OF RESULTS

In this chapter, an approximate, empirical density function has been determined for the near- and far-end voltage magnitude density of a lossless-matched transmission line being radiated by a monochromatic source equally likely to be incident from any horizontal position. The empirical density function is a simple form and exists only on the bounded interval of interest. As Monte Carlo analysis in Chapter 4 shows no good fit for the density of the voltage magnitude from a single source, the approximate results of this chapter have merit.

Although the empirical results are useful, the work of this chapter has ultimately shown that determining the density functions of the voltage magnitude for the coupling problem in question is difficult even in the simplest cases.

CHAPTER 7. CONCLUSIONS AND FUTURE WORK

The purpose of this thesis has been two-fold: to introduce and formalize the novel problem of HIPDI and to analyze random field coupling to deterministic uniform transmission lines.

In the first case, it has been shown that the existence of HIPDI poses a serious threat to communication channels as demonstrated by the application of the developed theory to the 100BaseTX Ethernet protocol. Specifically, levels as low as 142 mV pk-pk have been shown to disrupt Ethernet communication over CAT-5 for all hardware implementations considered without disrupting computer functionality in any other regard.

Future work in HIPDI research should consider the application to a wireless medium where the coupling problem is not inherent. Since wireless protocols are generally more complicated than wired protocols, such a problem would be a true test of the hardware aperture concept.

In the second problem of stochastic plane wave coupling to a uniform transmission line, it was necessary to develop a tool capable of generating probability density functions via Monte Carlo simulation. The tool used the compact BLT4 solution to make numerical density generation efficient. In many cases, where sufficient field amplitude uncertainty and/or sufficient field frequency uncertainty was present, it was found that exponential, gamma or Rayleigh distributions could be used to accurately describe the voltage densities at the transmission-line terminations arising from single or multiple plane-waves.

It is obvious that further work on the stochastic coupling problem is required. Specifically, the coupling of fields to deterministic or random twisted-pairs should be sought as many coupling problems of interest, including HIPDI, would benefit from the results.

REFERENCES

[1] C. Mojert, D. Nitsch, H. Friedjoff, J. Maack, F. Sabath, M. Camp, and H.Garbe, "UWB and EMP Susceptibility of Microprocessors and Networks," *14th International Zürich Symp. EMC,* Schweiz, Zürich, Feb. 20-22, 2001, pp.47-52.

[2] I. Kohlberb, and R. J. Carter, "Some Theoretical Considerations Regarding the susceptibility of Information Systems to Unwanted Electromagnetic Signals," *14th International Zürich Symp. EMC,* Schweiz, Zürich Feb.20-22, 2001, pp.41-46.

[3] F. Sonnermann, "Susceptibility Investigations of High-Power Em-Fileds on Electronic Systems," *15th International Zürich Symp. EMC,* Schweiz, Zürich, Feb. 18-20, 2003, pp 115 - 120.

[4] D. Nitsch, F. Sabath, H.-U Schmidt, and C. Braun, "Comparison of the High Power Microwave and Ultra Wide Band Susceptibility of Modern Microprocessors Boards," *15th International Zürich Symp. EMC,* Schweiz, Zürich, Feb. 18-20, 2003, pp 121 - 126.

[5] M. A. Messier, K.S. Smith, W. A. Radasky, and M. J. Madrid, "Response of Telecom Protection to Three IEC Waveforms," *15th International Zürich Symp. EMC,* Schweiz, Zürich, Feb. 18-20, 2003, pp 127 - 132.

[6] C. R. Paul, *Analysis of Multiconductor Transmission Lines*, John Wiley & Sons, New York, 1994.

[7] *IEEE Standard for Information Technology--Telecommunications and Information Exchange Between Systems--Local and Metropolitan Area Networks--Specific Requirements--Part 3: Carrier Sense Multiple Access with Collision Detection (CSMA/CD) Access Method and Physical Layer Specifications.,* IEEE std. 802.3-2002.

[8] J. Postel (ed.), "Transmission Control Protocol - DARPA Internet Program Protocol Specification," RFC 793, USC/Information Sciences Institute, September 1981.

[9] J. Postel (ed.), "User Datagram Protocol," RFC 768, USC/Information Sciences Institute, August 1980.

[10]T.K. Sakar and C. Su, "A tutorial on wavelets from an electrical engineering perspective, Part 2: The continuous case," *IEEE Antennas Propagat. Mag.,* vol. 40, pp. 36-49, Dec. 1998.

[11]B. Kordi, J. LoVetri, and G. Bridges, "Using wavelets to characterize time-frequency features of electromagnetic coupling problems," in *Proc. ANTEM'2002,* Quebec, Canada, July 31-Aug. 2 2002, pp.115-120.

[12]S. Celozzi, and M. Feliziani, "EMP-coupling to twisted-wire cables" *IEEE Int. Symp. EMC*, Aug. 21-23, 1990, pp 85- 89

[13]R. Solle, "Electromagnetic coupling of twisted pair cables" *Selected Areas in Communications, IEEE Journal on*, Vol. 20 Issue 5, June, 2002 pp. 883 -892

[14]H.Wang, G. Li, C. Shi, "The analysis of interference immunity of the LAN," *IEEE Int. Symp. EMC*, May 21-24 May 2002, pp. 726 -729

[15]S. Primak, J. LoVetri, "Statistical Modelling of External Coupling of Electromagnetic Waves to Printed Circuit Boards Inside a Leaky Cavity", Final Report, CRC Contract No xx, September 2001

[16]F. Tesche, *EMC Analysis Methods and Computational Models,* John Wiley and Sons, 1997.

[17]T. L. Saaty, *Modern Nonlinear Equations*, Ch. 8 (R. Syski), McGraw-Hill, New York, 1967.

[18]G. Adomian, *Stochastic Systems*, Academic Press, New York, 1983.

[19]T.T. Soong, *Random Differential Equations in Science and Engineering*, Academic Press, New York, 1973.

[20]T. Lapohos, "Multiconductor Transmission Line Networks", Ph.D Thesis, The University of Western Ontario, Apr. 1998.

[21]A. Friedman, *Stochastic Differential Equations and Applications,* Vol 1. Academic Press, New York, 1975.

[22]A. Papoulis, *Probability, Random Variables and Stochastic Processes*, 3rd Ed. WCB/ McGraw-Hill, Boston MA, 1991.

[23]T. H. Lehman, "A Statistical Theory of Electromagnetic Fields in Complex Cavities", *Interaction Note 494,* May, 1993.

[24]R.H. Price, H.T. Daves and E.P. Wenaas, "Determination of the Statistical Distribution of Electromagnetic Field Amplitude in Complex Cavities," *Physical Review E,* Vol. 48, No. 6, 1993, pp. 4716-4729.

[25]G. Marsaglian, "Choosing a Point from the Surface of a Sphere," *Ann. Math. Stat.* Vol. 43 pp. 645-646, 1972.

[26]R. C. Dubes, *The Theory of Applied Probability,* Prentice Hall, NJ, 1968.

[27]A.E. Taylor., *Advanced Calculus,* Ginn and Co. Boston MA.1993.

APPENDIX A. PROBE CALIBRATION

This appendix briefly discusses the calibration method used to calibrate the probe of Experiments A as presented in Chapter 2.

In *Step* 1 of Fig. A-1 the signal generator is initially connected directly to the EMI receiver using a short coaxial cable for verification of consistent frequency and signal level settings between the two instruments. A T-junction is inserted on the short coaxial cable between the signal generator and the EMI receiver. As expected, no appreciable loss in power was observed with the probe attached to the junction as opposed to leaving the junction terminal open-circuited. Therefore, it can be assumed that the connection of the high impedance probe has negligible effects on the interference signal. In *Step* 2, the probe is now attached across the open-circuit and connected back to the second port of the EMI receiver using the same 7 m of LMR400 Coaxial cable used in measuring the interference on the Ethernet cable. A sweep of frequencies from 1 - 100 MHz in steps of 1 MHz was made which yielded the required attenuation factors for the probe-coaxial cable unit. These attenuation factors (in dB) are added to the results of measuring the interference on the Ethernet cable at the corresponding frequencies. Although this procedure uses a short 50 Ω cable instead of the approximately 100 Ω category 5 Ethernet cable, it was assumed that the attenuation factors will remain the same due to the high impedance of the probe.

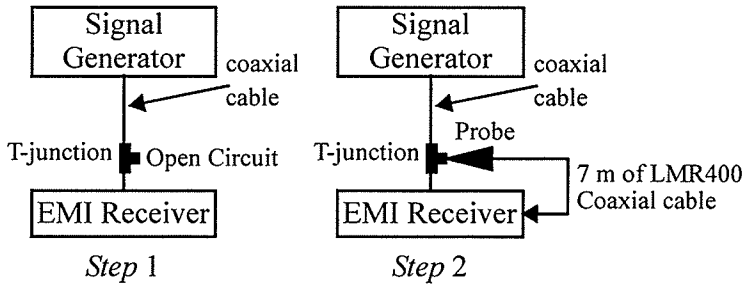

Figure A-1. High impedance probe calibration procedure.

APPENDIX B. FORMULATION OF THE BLT SOLUTION

This appendix formulates the BLT solution to the plane-wave coupling problem to a transmission line of length L oriented as in Fig. 3-1 and follows very closely the derivation in [15]

B.1 THE BLT SOLUTION FROM THE SCATTERED FIELD FORMULATION

By formulating the coupling problem using the scattered-voltage approach [15], the required equations to solve are:

$$\frac{d}{dx}V^{scat}(x) + ZI(x) = V_{s2}(x) \tag{B.1}$$

$$\frac{d}{dx}I(x) + YV^{scat}(x) = 0 \tag{B.2}$$

For mathematical convenience, these equations can be represented in vector form as the system:

$$\frac{d\boldsymbol{U}}{dx} + A\boldsymbol{U} = \boldsymbol{S} \tag{B.3}$$

where:

$$\boldsymbol{U} = \begin{bmatrix} V^{scat}(x) \\ I(x) \end{bmatrix}, A = \begin{bmatrix} 0 & Z \\ Y & 0 \end{bmatrix}, \boldsymbol{S} = \begin{bmatrix} V_{s2}(x) \\ 0 \end{bmatrix}. \tag{B.4}$$

Uncoupling Eq B.1 and Eq B.2 can be accomplished by diagonalizing the matrix A using the left and right eigenvector matrices:

$$L = \begin{bmatrix} 1 & Z_c \\ 1 & -Z_c \end{bmatrix}, R = \frac{1}{2}\begin{bmatrix} 1 & 1 \\ Y_c & -Y_c \end{bmatrix} \tag{B.5}$$

where $Z_c = \frac{1}{Y_c} = \sqrt{\frac{Z}{Y}}$ which gives:

$$LR = RL = \frac{1}{2}\begin{bmatrix} 1+Z_cY_c & 1-Z_cY_c \\ 1-Z_cY_c & 1+Z_cY_c \end{bmatrix} = \begin{bmatrix} 1 & 0 \\ 0 & 1 \end{bmatrix} \tag{B.6}$$

In addition, left and right multiplication of A by L and R gives:

$$LAR = \begin{bmatrix} \gamma & 0 \\ 0 & -\gamma \end{bmatrix} = \Gamma \tag{B.7}$$

where the complex propagation constant $\gamma = \sqrt{ZY} = Z_cY = Y_cZ$.

The BLT solution now uses the transformations

$$\boldsymbol{W} = L\boldsymbol{U} = \begin{bmatrix} W_+(x) \\ W_-(x) \end{bmatrix} = \begin{bmatrix} 1 & Z_c \\ 1 & -Z_c \end{bmatrix}\begin{bmatrix} V^{scat}(x) \\ I(x) \end{bmatrix} = \begin{bmatrix} V^{scat}(x)+Z_cI(x) \\ V^{scat}(x)-Z_cI(x) \end{bmatrix} \tag{B.8}$$

with the left and right eigenvectors chosen as Eq B.5 it is a simple matter to invert the transformation of Eq B.8:

$$\boldsymbol{U} = R\boldsymbol{W} = \begin{bmatrix} V^{scat}(x) \\ I(x) \end{bmatrix} = \frac{1}{2}\begin{bmatrix} 1 & 1 \\ Y_c & -Y_c \end{bmatrix}\begin{bmatrix} W_+(x) \\ W_-(x) \end{bmatrix} = \frac{1}{2}\begin{bmatrix} W_+(x)+W_-(x) \\ Y_cW_+(x)-Y_cW_-(x) \end{bmatrix} \tag{B.9}$$

By using the transformations it is possible to uncouple the Eq B.3 as follows:

$$\begin{aligned} \frac{d}{dx}R\boldsymbol{W} + AR\boldsymbol{W} &= \boldsymbol{S} \\ LR\frac{d\boldsymbol{W}}{dx} + LAR\boldsymbol{W} &= L\boldsymbol{S} \\ d\boldsymbol{W} + \Gamma\boldsymbol{W} &= L\boldsymbol{S} \end{aligned} \tag{B.10}$$

resulting in the two uncoupled ordinary differential equations:

$$dW_+ + \gamma W_+ = V_{s2}(x) \tag{B.11}$$

$$dW_- - \gamma W_- = V_{s2}(x) \tag{B.12}$$

In order to fully solve the ordinary differential equations, the appropriate boundary conditions must be satisfied. In the scattered field method the resulting boundary conditions are:

$$\begin{aligned} V^{scat}(0) &= Z_o I(0) - V_o \\ V^{scat}(L) &= Z_o I(0) - V_l \end{aligned} \tag{B.13}$$

applying Eq B.13 to Eq B.9 gives:

$$\begin{aligned} W_+(0) &= \rho_0 W_-(0) - (1-\rho_0)V_0 \\ W_-(L) &= \rho_L W_+(L) - (1-\rho_L)V_L \end{aligned} \tag{B.14}$$

Thus from Eq B.13 expressions for the outgoing wave at $x = 0$ in terms of the incoming wave and the incoming wave at $x = L$ in terms of the outgoing wave.

The solution to Eq B.11 is easily obtainable if the equations is first multiplied by the integrating factor $e^{\gamma x}$:

$$d(W_+(x)e^{\gamma x}) = V_{s2}(x)e^{\gamma x} \tag{B.15}$$

which can now be integrated from 0 to x giving:

$$W_+(x) - W_+(0)e^{\gamma x} + \int_0^x e^{\gamma\xi} V_{s2}(\xi)d\xi$$

$$W_+(x) = W_+(0)e^{\gamma x} + \int_0^x e^{\gamma\xi} V_{s2}(\xi)d\xi \tag{B.16}$$

In a similar fashion it is possible to determine the solution to Eq B.12.

First multiplying by $e^{-\gamma x}$ results in:

$$d(W_-(x)e^{-\gamma x}) = V_{s2}(x)e^{-\gamma x} \tag{B.17}$$

Integrating both sides from x to L gives:

$$W_-(L)e^{-\gamma L} - W_-(x)e^{-\gamma x} = \int_x^L e^{-\gamma\xi} V_{s2}(\xi)d\xi$$

$$W_-(x) = W_-(L)e^{-\gamma L}e^{-\gamma x} - e^{-\gamma x}\int_x^L e^{-\gamma\xi} V_{s2}(\xi)d\xi \tag{B.18}$$

$$W_-(x) = W_-(L)e^{\gamma(x-L)} - \int_x^L e^{\gamma(x-\xi)} V_{s2}(\xi)d\xi$$

At $x = L$ Eq B.16 becomes:

$$W_+(L) = W_+(0)e^{\gamma L} + \int_0^L e^{\gamma\xi} V_{s2}(\xi)d\xi$$

$$W_+(0) - W_+(L)e^{\gamma L} = -\int_0^L e^{\gamma\xi} V_{s2}(\xi)d\xi = S_1' \tag{B.19}$$

and at $x = 0$ Eq B.18 becomes:

$$W_{-}(0) = W_{-}(L)e^{-\gamma L} - \int_0^L e^{-\gamma\xi} V_{s2}(\xi)d\xi$$
$$W_{-}(L) - W_{-}(0)e^{\gamma l} = \int_0^L e^{\gamma(l-\xi)} V_{s2}(\xi)d\xi = S_2' \tag{B.20}$$

Resulting in a set of four equations in the four unknowns $W_{-}(L), W_{-}(0), W_{+}(L), W_{+}(0)$. If the system is solved for the outgoing and incoming waves at 0 and L then it is possible to determine the terminal voltages and currents through Eq B.9. The resulting currents are:

$$\begin{bmatrix} I(0) \\ I(L) \end{bmatrix} = \frac{Y_c}{2} \begin{bmatrix} W_{+}(0) - W_{-}(0) \\ W_{+}(L) - W_{-}(L) \end{bmatrix} \tag{B.21}$$

and the voltages can be solved to be:

$$\begin{bmatrix} V^{scat}(0) \\ V^{scat}(L) \end{bmatrix} = \frac{1}{2} \begin{bmatrix} W_{+}(0) + W_{-}(0) \\ W_{+}(L) + W_{-}(L) \end{bmatrix}. \tag{B.22}$$

Returning to Eq B.14 - rewritten here for convenience:

$$W_{+}(0) = \rho_0 W_{-}(0) - (1-\rho_0)V_0$$
$$W_{-}(L) = \rho_L W_{+}(L) - (1-\rho_L)V_L$$

it is possible to re-write this in matrix form as:

$$\begin{bmatrix} W_{+}(0) \\ W_{-}(L) \end{bmatrix} = \begin{bmatrix} \rho_0 & 0 \\ 0 & \rho_L \end{bmatrix} \begin{bmatrix} W_{-}(0) \\ W_{+}(L) \end{bmatrix} - \begin{bmatrix} (1-\rho_0)V_0 \\ (1-\rho_L)V_L \end{bmatrix} \tag{B.23}$$

and similarly, Eq B.19 and Eq B.20 can be written as:

$$\begin{bmatrix} W_{+}(0) \\ W_{-}(L) \end{bmatrix} = \begin{bmatrix} 0 & e^{\gamma l} \\ e^{\gamma l} & 0 \end{bmatrix} \begin{bmatrix} W_{-}(0) \\ W_{+}(L) \end{bmatrix} + \begin{bmatrix} S_1' \\ S_2' \end{bmatrix} \tag{B.24}$$

Subtracting Eq B.23 from Eq B.24 gives:

$$\begin{bmatrix}0\\0\end{bmatrix} = \begin{bmatrix}-\rho_0 & e^{\gamma l}\\ e^{\gamma l} & -\rho_L\end{bmatrix}\begin{bmatrix}W_-(0)\\ W_+(L)\end{bmatrix} + \begin{bmatrix}S_1' + (1-\rho_0)V_0\\ S_2' + (1-\rho_L)V_L\end{bmatrix} \tag{B.25}$$

which can be solved for the unknowns $W_-(0)$, $W_+(L)$ in terms of the terms S_1' and S_2':

$$\begin{bmatrix}W_-(0)\\ W_+(L)\end{bmatrix} = -\begin{bmatrix}-\rho_0 & e^{\gamma l}\\ e^{\gamma l} & -\rho_L\end{bmatrix}^{-1}\begin{bmatrix}S_1' + (1-\rho_0)V_0\\ S_2' + (1-\rho_L)V_L\end{bmatrix}. \tag{B.26}$$

Substitution into Eq B.23 gives:

$$\begin{bmatrix}W_+(0)\\ W_-(L)\end{bmatrix} = -\begin{bmatrix}\rho_0 & 0\\ 0 & \rho_L\end{bmatrix}\begin{bmatrix}-\rho_0 & e^{\gamma l}\\ e^{\gamma l} & -\rho_L\end{bmatrix}^{-1}\begin{bmatrix}S_1' + (1-\rho_0)V_0\\ S_2' + (1-\rho_L)V_L\end{bmatrix} - \begin{bmatrix}(1-\rho_0)V_0\\ (1-\rho_L)V_L\end{bmatrix} \tag{B.27}$$

Now it is possible to solve for the current by substituting Eq B.26 and Eq B.27 into Eq B.21:

$$\begin{bmatrix}I(0)\\ I(L)\end{bmatrix} = -\frac{Y_c}{2}\begin{bmatrix}\rho_0 - 1 & 0\\ 0 & \rho_L - 1\end{bmatrix}\begin{bmatrix}-\rho_0 & e^{\gamma l}\\ e^{\gamma l} & -\rho_L\end{bmatrix}^{-1}\begin{bmatrix}S_1' + (1-\rho_0)V_0\\ S_2' + (1-\rho_L)V_L\end{bmatrix} - \frac{Y_c}{2}\begin{bmatrix}(1-\rho_0)V_0\\ (1-\rho_L)V_L\end{bmatrix} \tag{B.28}$$

The above expression can be conveniently re-written as:

$$\begin{bmatrix}I(0)\\ I(L)\end{bmatrix} = -\frac{Y_c}{2}\begin{bmatrix}\rho_0 - 1 & 0\\ 0 & \rho_L - 1\end{bmatrix}\begin{bmatrix}-\rho_0 & e^{\gamma l}\\ e^{\gamma l} & -\rho_L\end{bmatrix}^{-1}\left\{\begin{bmatrix}S_1' + (1-\rho_0)V_0\\ S_2' + (1-\rho_L)V_L\end{bmatrix} + \begin{bmatrix}-\rho_0 & e^{\gamma l}\\ e^{\gamma l} & -\rho_L\end{bmatrix}\begin{bmatrix}\frac{1}{(\rho_0 - 1)} & 0\\ 0 & \frac{1}{\rho_L - 1}\end{bmatrix}\begin{bmatrix}(1-\rho_0)V_0\\ (1-\rho_L)V_L\end{bmatrix}\right\}$$

where the expression in the curly brackets can be simplified to:

$$\begin{aligned}\begin{bmatrix}I(0)\\ I(L)\end{bmatrix} &= -\frac{Y_c}{2}\begin{bmatrix}\rho_0 - 1 & 0\\ 0 & \rho_L - 1\end{bmatrix}\begin{bmatrix}-\rho_0 & e^{\gamma l}\\ e^{\gamma l} & -\rho_L\end{bmatrix}^{-1}\left\{\begin{bmatrix}S_1' + (1-\rho_0)V_0\\ S_2' + (1-\rho_L)V_L\end{bmatrix} + \begin{bmatrix}\rho_0 V_0 - e^{\gamma L}V_L\\ -e^{\gamma L}V_0 + \rho_L V_L\end{bmatrix}\right\}\\ &= -\frac{Y_c}{2}\begin{bmatrix}\rho_0 - 1 & 0\\ 0 & \rho_L - 1\end{bmatrix}\begin{bmatrix}-\rho_0 & e^{\gamma l}\\ e^{\gamma l} & -\rho_L\end{bmatrix}^{-1}\left\{\begin{bmatrix}S_1' + V_0 - e^{\gamma L}V_L\\ S_2' - e^{\gamma L}V_0 + V_L\end{bmatrix}c\right\}\end{aligned} \tag{B.29}$$

The curly brackets are used to denote the source terms:

$$\begin{bmatrix} S_1 \\ S_2 \end{bmatrix} = \begin{bmatrix} S_1' + V_0 - e^{\gamma L} V_L \\ S_2' - e^{\gamma L} V_0 + V_L \end{bmatrix} \tag{B.30}$$

such that Eq B.29 can be re-written as:

$$\begin{bmatrix} I(0) \\ I(L) \end{bmatrix} = \frac{Y_c}{2} \begin{bmatrix} 1-\rho_o & 0 \\ 0 & 1-\rho_L \end{bmatrix} \begin{bmatrix} -\rho_0 & e^{\gamma l} \\ e^{\gamma l} & -\rho_L \end{bmatrix}^{-1} \begin{bmatrix} S_1 \\ S_2 \end{bmatrix} \tag{B.31}$$

From Eq B.31 the total voltage can be obtained using the appropriate boundary conditions for the voltage:

$$\begin{bmatrix} V(0) \\ V(L) \end{bmatrix} = \frac{Y_c}{2} \begin{bmatrix} Z_o & 0 \\ 0 & Z_L \end{bmatrix} \begin{bmatrix} 1-\rho_o & 0 \\ 0 & 1-\rho_L \end{bmatrix} \begin{bmatrix} -\rho_0 & e^{\gamma l} \\ e^{\gamma l} & -\rho_L \end{bmatrix}^{-1} \begin{bmatrix} S_1 \\ S_2 \end{bmatrix} \tag{B.32}$$

which can be simplified to:

$$\begin{aligned} \begin{bmatrix} V(0) \\ V(L) \end{bmatrix} &= \frac{Y_c}{2} \begin{bmatrix} Z_o(1-\rho_o) & 0 \\ 0 & Z_L(1-\rho_L) \end{bmatrix} \begin{bmatrix} -\rho_0 & e^{\gamma l} \\ e^{\gamma l} & -\rho_L \end{bmatrix}^{-1} \begin{bmatrix} S_1 \\ S_2 \end{bmatrix} \\ &= \frac{Y_c}{2} \begin{bmatrix} Z_o\left(1-\dfrac{Z_o - Z_c}{Z_o + Z_c}\right) & 0 \\ 0 & Z_L\left(1-\dfrac{Z_L - Z_c}{Z_L + Z_c}\right) \end{bmatrix} \begin{bmatrix} -\rho_0 & e^{\gamma l} \\ e^{\gamma l} & -\rho_L \end{bmatrix}^{-1} \begin{bmatrix} S_1 \\ S_2 \end{bmatrix} \end{aligned} \tag{B.33}$$

$$= \frac{Y_c}{2}\begin{bmatrix} Z_o\left(1-\frac{Z_o-Z_c}{Z_o+Z_c}\right) & 0 \\ 0 & Z_L\left(1-\frac{Z_L-Z_c}{Z_L+Z_c}\right) \end{bmatrix}\begin{bmatrix} -\rho_0 & e^{\gamma l} \\ e^{\gamma l} & -\rho_L \end{bmatrix}^{-1}\begin{bmatrix} S_1 \\ S_2 \end{bmatrix}$$

$$= \frac{Y_c}{2}\begin{bmatrix} Z_o\left(\frac{2Z_c}{Z_o+Z_c}\right) & 0 \\ 0 & Z_L\left(\frac{2Z_c}{Z_L+Z_c}\right) \end{bmatrix}\begin{bmatrix} -\rho_0 & e^{\gamma l} \\ e^{\gamma l} & -\rho_L \end{bmatrix}^{-1}\begin{bmatrix} S_1 \\ S_2 \end{bmatrix} \qquad \text{(B.34)}$$

$$= \frac{1}{2}\begin{bmatrix} Z_o\left(\frac{2}{Z_o+Z_c}\right) & 0 \\ 0 & Z_L\left(\frac{2}{Z_L+Z_c}\right) \end{bmatrix}\begin{bmatrix} -\rho_0 & e^{\gamma l} \\ e^{\gamma l} & -\rho_L \end{bmatrix}^{-1}\begin{bmatrix} S_1 \\ S_2 \end{bmatrix}$$

$$\begin{bmatrix} V(0) \\ V(L) \end{bmatrix} = \frac{1}{2}\begin{bmatrix} 1+\rho_0 & 0 \\ 0 & 1+\rho_L \end{bmatrix}\begin{bmatrix} -\rho_0 & e^{\gamma l} \\ e^{\gamma l} & -\rho_L \end{bmatrix}^{-1}\begin{bmatrix} S_1 \\ S_2 \end{bmatrix}$$

B.2 PLANE WAVE INCIDENCE

In the above formulation of the BLT solution to an electromagnetic field coupling to a uniform transmission line we have developed an equation in terms of the source terms S_1 and S_2 where the source terms are given by:

$$\begin{bmatrix} S_1 \\ S_2 \end{bmatrix} = \begin{bmatrix} S_1' + V_0 - e^{\gamma L}V_L \\ S_2' - e^{\gamma L}V_0 + V_L \end{bmatrix} \qquad \text{(B.35)}$$

where S_1' and S_2' are related as:

$$\begin{bmatrix} S_1' \\ S_2' \end{bmatrix} = \begin{bmatrix} -\int_0^L e^{\gamma\xi} V_{s2}(\xi) d\xi \\ \int_0^L e^{\gamma(l-\xi)} V_{s2}(\xi) d\xi \end{bmatrix}. \tag{B.36}$$

Therefore, in order to be useful we must calculate the source terms for a given electromagnetic field. Plane wave incidence is considered. The geometry of the incident field is shown in Fig. 3-2.

In Cartesian space, with unit vectors $\hat{\boldsymbol{a}}_x$, $\hat{\boldsymbol{a}}_y$ and $\hat{\boldsymbol{a}}_z$, it is possible to specify the incident field as:

$$E^{inc}(t, \boldsymbol{r}) = \hat{\boldsymbol{e}} E(t - \boldsymbol{v} \cdot \boldsymbol{r}/|v|^2), \tag{B.37}$$

where the position vector $\boldsymbol{r}$ is related to the Cartesian coordinates by as $\boldsymbol{r} = x\hat{\boldsymbol{a}}_x + y\hat{\boldsymbol{a}}_y + z\hat{\boldsymbol{a}}_z$, t is time and $\hat{\boldsymbol{e}}$ is the unit vector in the direction of the electric field. The velocity vector $\boldsymbol{v}$ is related to the Cartesian coordinates in a similar manner as the position vector: $\boldsymbol{v} = v_x\hat{\boldsymbol{a}}_x + v_y\hat{\boldsymbol{a}}_y + v_z\hat{\boldsymbol{a}}_z$, where v_x, v_y and v_z are the components of the velocity vector in the $\hat{\boldsymbol{a}}_x$, $\hat{\boldsymbol{a}}_y$ and $\hat{\boldsymbol{a}}_z$ directions respectively. The velocity vector relates directly to the direction of propagation as $\boldsymbol{v} = -v_o\hat{\boldsymbol{a}}_r$.

As only time-harmonic fields are considered, field is assumed to be monochromatic with an $e^{j\omega t}$ time dependence, resulting in the simplified the field expression:

$$E^{inc}(\boldsymbol{r}) = \hat{\boldsymbol{e}} E e^{-j(\boldsymbol{k} \cdot \boldsymbol{r})}, \tag{B.38}$$

where now E is the complex phasor representation of the plane wave form as it passes through the origin. The propagation vector $\boldsymbol{k}$ is in the direction of the field propagation (or equivalently the direction of the velocity vector) and is related directly to the velocity as $\boldsymbol{k} = \frac{-v_o}{\omega}\hat{\boldsymbol{a}}_r$.

Having fully defined the physically problem, it is possible to specify the unit vector $\hat{\boldsymbol{e}}$ using its cartesian components which relate directly to the angle of polarization:

$$\hat{\boldsymbol{e}} = e_x\hat{\boldsymbol{a}}_x + e_y\hat{\boldsymbol{a}}_y + e_z\hat{\boldsymbol{a}}_z = \cos(\zeta)\hat{\boldsymbol{a}}_\theta + \sin(\zeta)\hat{\boldsymbol{a}}_\phi \tag{B.39}$$

For convenience, this may be written in matrix form as:

$$\begin{bmatrix} 0 & \cos(\zeta) & \sin(\zeta) \end{bmatrix} R \begin{bmatrix} \hat{\boldsymbol{a}}_x \\ \hat{\boldsymbol{a}}_y \\ \hat{\boldsymbol{a}}_z \end{bmatrix} \tag{B.40}$$

where R is the usual transformation from Cartesian to spherical coordinates:

$$R = \begin{bmatrix} \sin\theta\cos\phi & \sin\theta\sin\phi & \cos\theta \\ \cos\theta\cos\phi & \cos\theta\sin\phi & -\sin\theta \\ -\sin\phi & \cos\phi & 0 \end{bmatrix} \tag{B.41}$$

and hence the direction of propagation is given as:

$$\hat{\boldsymbol{e}} = \begin{bmatrix} \hat{\boldsymbol{a}}_x & \hat{\boldsymbol{a}}_y & \hat{\boldsymbol{a}}_z \end{bmatrix} \begin{bmatrix} \cos\theta\cos\phi\cos\zeta - \sin\phi\sin\zeta \\ \cos\theta\sin\phi\cos\zeta + \cos\phi\sin\zeta \\ -\sin\theta\cos\zeta \end{bmatrix} \tag{B.42}$$

In a similar manner to the direction of propagation, the velocity and propagation vector are given as:

$$\boldsymbol{v} = \begin{bmatrix} -v_o & 0 & 0 \end{bmatrix} R \begin{bmatrix} \hat{\boldsymbol{a}}_x \\ \hat{\boldsymbol{a}}_y \\ \hat{\boldsymbol{a}}_z \end{bmatrix} = -v_o(\sin\theta\cos\phi\hat{\boldsymbol{a}}_x + \sin\theta\sin\phi\hat{\boldsymbol{a}}_y + \cos\theta\hat{\boldsymbol{a}}_z) \tag{B.43}$$

$$k = \begin{bmatrix} -k & 0 & 0 \end{bmatrix} R \begin{bmatrix} \hat{\boldsymbol{a}}_x \\ \hat{\boldsymbol{a}}_y \\ \hat{\boldsymbol{a}}_z \end{bmatrix} = -k(\sin\theta\cos\phi\hat{\boldsymbol{a}}_x + \sin\theta\sin\phi\hat{\boldsymbol{a}}_y + \cos\theta\hat{\boldsymbol{a}}_z). \tag{B.44}$$

With these results it is possible to rewrite the complex phasor representation of the time-harmonic plane wave as:

$$E^{inc}(x, y, z) = \hat{\boldsymbol{e}}Ee^{jk(x\sin\theta\cos\phi + y\sin\theta\sin\phi + z\cos\theta)} \tag{B.45}$$

From this expression it is a simple task of determining the field components along the transmission line existing at $y = 0$:

$$E_x(x, 0, z) = (\cos\theta\cos\phi\cos\zeta - \sin\phi\sin\zeta)Ee^{jk(x\sin\theta\cos\phi + z\cos\theta)} \tag{B.46}$$

$$E_y(x, 0, z) = (\cos\theta\sin\phi\cos\zeta - \cos\phi\sin\zeta)Ee^{jk(x\sin\theta\cos\phi + z\cos\theta)} \tag{B.47}$$

$$E_z(x, 0, z) = -\sin\theta\cos\zeta Ee^{jk(x\sin\theta\cos\phi + z\cos\theta)}. \tag{B.48}$$

With these expressions is it also simple to determine the value of the forcing functions:

$$\begin{aligned} V_{s2} &= E_x^{inc}(x, d) - E_x^{inc}(x, 0) \\ &= (\cos\theta\cos\phi\cos\zeta - \sin\phi\sin\zeta)E(e^{jkd\cos\theta} - 1)e^{jkx\sin\theta\cos\phi} \end{aligned} \tag{B.49}$$

$$\begin{aligned} V_0 &= -\int_0^d E_z^{inc}(0, z)dz \\ &= E\sin\theta\cos\zeta\int_0^d e^{jkz\cos\theta}dz = E\sin\theta\cos\zeta\left(\frac{e^{jkd\cos\theta} - 1}{jk\cos\theta}\right) \end{aligned} \tag{B.50}$$

$$V_L = \int_0^d E_z^{inc}(L,z)dz$$
$$= E\sin\theta\cos\zeta e^{jkl\sin\theta\cos\phi}\int_0^d e^{jkz\cos\theta}dz = E\sin\theta\cos\zeta e^{jkl\sin\theta\cos\phi}\left(\frac{e^{jkd\cos\theta}-1}{jk\cos\theta}\right) \quad \text{(B.51)}$$

As only the TEM mode is assumed to exists propagates, the assumption $kd \ll 1$, allowing the approximation $e^{jkd\cos\theta} - 1 \approx jkd\cos\theta$ such that Eqs. B.49-B.51 simplify to:

$$V_{s2} = jkd\cos\theta E(\cos\theta\cos\phi\cos\zeta - \sin\phi\sin\zeta)e^{jkx\sin\theta\cos\phi} \quad \text{(B.52)}$$

$$V_0 = Ed\sin\theta\cos\zeta \quad \text{(B.53)}$$

$$V_L = Ed\sin\theta\cos\zeta e^{jkl\sin\theta\cos\phi} = V_0 e^{jkl\sin\theta\cos\phi}. \quad \text{(B.54)}$$

Now calculate the terms S_1 and S_2 can be determined from Eq B.35 and Eq B.36:

$$\begin{bmatrix} S_1 \\ S_2 \end{bmatrix} = \begin{bmatrix} -\int_0^L e^{\gamma\xi}V_{s2}(\xi)d\xi + V_0 - e^{\gamma L}V_L \\ \int_0^L e^{\gamma(l-\xi)}V_{s2}(\xi)d\xi - e^{\gamma L}V_0 + V_L \end{bmatrix} \quad \text{(B.55)}$$

$$\begin{bmatrix} S_1' \\ S_2' \end{bmatrix} = \begin{bmatrix} -\int_0^L e^{\gamma\xi}kd\cos\theta E(\cos\theta\cos\phi\cos\zeta - \sin\phi\sin\zeta)e^{jk\xi\sin\theta\cos\phi}d\xi \\ \int_0^L e^{\gamma(l-\xi)}kd\cos\theta E(\cos\theta\cos\phi\cos\zeta - \sin\phi\sin\zeta)e^{jk\xi\sin\theta\cos\phi}d\xi \end{bmatrix}$$

The solution to the integral is simple due to the complex exponential:

$$\begin{bmatrix} S_1' \\ S_2' \end{bmatrix} = \begin{bmatrix} -jkd\cos\theta E\dfrac{(\cos\theta\cos\phi\cos\zeta - \sin\phi\sin\zeta)}{jk\sin\theta\cos\phi + \gamma} e^{(jk\sin\theta\cos\phi + \gamma)L} \\ -e^{\gamma l} jkd\cos\theta E\left(\dfrac{\cos\theta\cos\phi\cos\zeta - \sin\phi\sin\zeta}{jk\sin\theta\cos\phi - \gamma}\right) e^{(jk\sin\theta\cos\phi - \gamma)L} \end{bmatrix} \tag{B.56}$$

Therefore, using Eqs 53-56 gives:

$$\begin{bmatrix} S_1 \\ S_2 \end{bmatrix} = -Ed\begin{bmatrix} \left(jk\cos\theta\dfrac{(\cos\theta\cos\phi\cos\zeta - \sin\phi\sin\zeta)}{jk\sin\theta\cos\phi + \gamma} + \sin\theta\cos\phi\right)(e^{(jk\sin\theta\cos\phi + \gamma)L} - 1) \\ e^{\gamma l}\left(jk\cos\left(\theta\dfrac{(\cos\theta\cos\phi\cos\zeta - \sin\phi\sin\zeta)}{-jk\sin\theta\cos\phi + \gamma} - \sin\theta\cos\phi\right)\right)(e^{(jk\sin\theta\cos\phi - \gamma)L} - 1) \end{bmatrix} \tag{B.57}$$

and the BLT solution is complete.

APPENDIX C. A REVIEW OF PROBABILITY THEORY

This appendix simply summarizes some basic probability theory and random variable concepts as presented in [22].

C.1 RANDOM VARIABLES

Given the outcomes ξ_i, $i = 1, \ldots, n, \ldots$ of an experiment, a random variable (RV) $\boldsymbol{x}$ is a mapping from each ξ_i to a number either real or complex. Unless otherwise stated, the RV $\boldsymbol{x}$ is assumed real. For example, if gambling on the roll of a die, each face may be associated with a monetary value. Formally,

$$\boldsymbol{x} = g(\xi). \tag{C.1}$$

The RV $\boldsymbol{x}$ is a function in the usual sense. The domain of the function is the set of all experiment outcomes S and the image of the function is specified explicitly by $g(\xi)$.

C.2 DESCRIBING A RANDOM VARIABLE - CDF AND PDF

In order to describe and manipulate RVs it is convenient to have an appropriate mathematical representation of its statistics. Consider the event that $\{\boldsymbol{x} \leq X\}$ for some X in the domain S of $\boldsymbol{x}$. It is intuitive that the number of outcomes in S such that $\{\boldsymbol{x} \leq X\}$ is

dependent on X and therefore the probability $P\{\boldsymbol{x} \le X\}$ is a number dependent on X. This number is called the *cumulative distribution function* or CDF of $\boldsymbol{x}$ and symbolize it by $F_x(X)$.

$$F_x(X) = P\{\boldsymbol{x} \le X\}. \tag{C.2}$$

When no ambiguity will arise it is convenient to use the notation $F(X)$ to denote $F_x(X)$. Using the axioms of probability and the definitions:

$$\begin{aligned} F(X^+) &= \lim_{0<\varepsilon\to 0} F(X+\varepsilon) \\ F(X^-) &= \lim_{0<\varepsilon\to 0} F(X-\varepsilon) \end{aligned} \tag{C.3}$$

it is possible to define the following properties of the CDF of a RV $\boldsymbol{x}$:

$$\begin{aligned} &\text{a) } F(\infty) = 1 \qquad F(-\infty) = 0 \\ &\text{b) } F(X_1) \le F(X_2) \qquad X_1 < X_2 \\ &\text{c) if } F(X_0) = 0 \text{ then } F(X) = 0 \quad \forall\ X \le X_0 \\ &\text{d) } P\{\boldsymbol{x} > X\} = 1 - F_x(X) \\ &\text{e) } F(X^+) = F(X) \qquad \text{continuity at the right} \\ &\text{f) } P\{X_1 < \boldsymbol{x} \le X_2\} = F(X_2) - F(X_1) \\ &\text{g) } P\{\boldsymbol{x} = X\} = F(X) - F(X^-) \\ &\text{h) } P\{X_1 \le \boldsymbol{x} \le X_2\} = F(X_2) - F(X_1^-) \end{aligned} \tag{C.4}$$

Herein the concern is RVs of the continuous type. That is, the value of $\boldsymbol{x}$ is continuous over either a finite or infinite range. The former will be referred to as *bounded* RVs and the latter as having *infinite support* or simply *infinite* RVs.

Although the CDF of a random variable complete describes its statistics, it is often more convenient to describe a random variable by it's *(probability) density function* $f_x(X)$ (PDF) defined as the derivative of the CDF:

$$f_x(X) = \frac{dF(X)}{d(X)}. \tag{C.5}$$

Once again, when no ambiguity is possible it is convenient to denote $f_x(X)$ by $f(X)$. $f(X)$ is often referred to simply as *density* of $\boldsymbol{x}$.

The probabilistic interpretation of the density of a RV $\boldsymbol{x}$ is obtained by considering the Eq C.4d and Eq C.5:

$$P\{X_1 < \boldsymbol{x} \le X_2\} = F(X_2) - F(X_1) = \int_{X_1}^{X_2} f(X)dX. \tag{C.6}$$

Approximating the differential dX by some finite, but sufficient small amount ΔX it can be seen that:

$$P\{X < \boldsymbol{x} \le X + \Delta X\} \approx f(X)\Delta X \tag{C.7}$$

where the equality holds in the limit:

$$f(X) = \lim_{\Delta X \to 0} \frac{P\{X < \boldsymbol{x} \le X + \Delta X\}}{\Delta X} \tag{C.8}$$

Qualitatively the PDF $f(X)$ of a RV $\boldsymbol{x}$ is described as being the probability that the value of $\boldsymbol{x}$ lies in the range $(X, X + \Delta X]$ when ΔX is sufficiently small. Mathematically it is simply describe as being the derivative of the CDF of $\boldsymbol{x}$. Finally, due to the monotonic nature of the distribution $F(X)$, the density $f(X)$ is non-negative:

$$f(X) \geq 0 . \tag{C.9}$$

C.3 THE DISTRIBUTION OF EXPERIMENT OUTCOMES

It is often convenient to describe a RV by its distribution or density without considering a specific probability space S. In order to interpret a RV in this way it is sufficient to show that given a density $f(X)$ and distribution $F(X)$ then the integral relation

$$F(X) = \int_{-\infty}^{x} f(\alpha) d\alpha \tag{C.10}$$

appropriately describes a RV.

Proof ([22], 4-3 p.74):

The event $\{X \leq X_1\}$ is the outcome X of an experiment where the value of X is less than or equal to X_1. We define the probability of this event as in the case of a RV to be $P\{X \leq X_1\} = F(X)$ as in Eq C.10. Limiting the outcomes of events to real numbers we can define the RV $\boldsymbol{x}$ for every value of X as $\boldsymbol{x}(X) = X$. Then, since the event $\{X \leq X_1\} = \{\boldsymbol{x} \leq X_1\}$, the function $F(X)$ is identically the distribution of the RV $\boldsymbol{x}$. □

This proof simply tells us that we can consider a RV as being described by its density or distribution without concerning the experimental outcomes of a probability space.

C.4 BIVARIATE DISTRIBUTIONS

Many situations arise in which we are concerned with the probability of more than a single experiment. For example, we may have two RVs $\boldsymbol{x}$ and $\boldsymbol{y}$ with distributions $F(X)$ and $F(Y)$ respectively, and desire the probability of the event $\{\boldsymbol{x} \le X\} \cap \{\boldsymbol{y} \le Y\} = \{\boldsymbol{x} \le X, \boldsymbol{y} \le Y\}$. We call the probability of this event the *joint* or *bivariate* distribution $F_{xy}(X, Y)$

$$F_{xy}(X, Y) = P\{\boldsymbol{x} \le X, \boldsymbol{y} \le Y\}. \tag{C.11}$$

which in general *cannot* be expressed in terms of $F(X)$ and $F(Y)$.

Analogous to the case of a single random variable we can define the joint density $f(X, Y)$ of two RVs as

$$f(X, Y) = \frac{\partial^2}{\partial x \partial y} F(X, Y), \tag{C.12}$$

In so doing it is apparent that the joint distribution is obtainable from the joint density by integration

$$F(X, Y) = \int_{-\infty}^{X} \int_{-\infty}^{Y} f(\alpha, \beta) d\alpha d\beta. \tag{C.13}$$

C.5 MARGINAL STATISTICS

It is possible to obtain the separate or *marginal* distributions and densities of two random variables $\boldsymbol{x}$ and $\boldsymbol{y}$ directly from the joint distribution or density as:

$$F(X) = F(X, \infty) \qquad F(Y) = F(\infty, Y)$$
$$f(X) = \int_{-\infty}^{\infty} f(X, Y)dY \qquad f(Y) = \int_{-\infty}^{\infty} f(X, Y)dX \tag{C.14}$$

as proven in [22] 6-1 pp. 126-127.

It is apparent that the marginal statistics of the RVs $\boldsymbol{x}$ and $\boldsymbol{y}$, which completely describe their respective statistics, are obtainable from joint distribution. Unfortunately, obtaining the joint distribution is not always simple.

C.6 The Bivariate Distribution of Two Independent Random Variables

Two RVs $\boldsymbol{x}$ and $\boldsymbol{y}$ are called *independent* if the events $\{\boldsymbol{x} \in A\}$ and $\{\boldsymbol{y} \in B\}$ are independent. This says that the event $\{\boldsymbol{x} \in A\}$ does not affect the outcome of the event $\{\boldsymbol{y} \in B\}$ and vice-versa. By the axioms of probability, the statement of independence is equivalent to the mathematical statement

$$P\{\boldsymbol{x} \in A, \boldsymbol{y} \in B\} = P\{\boldsymbol{x} \in A\}P\{\boldsymbol{y} \in B\}, \tag{C.15}$$

indicating that the probability of the events $\{\boldsymbol{x} \in A\}$ *and* $\{\boldsymbol{y} \in B\}$ occurring is the product of the probabilities of each event occurring separately. Therefore, by considering A to be the event $\{\boldsymbol{x} \leq X\}$ and B the event $\{\boldsymbol{y} \leq Y\}$, by Eq C.11 and Eq C.15 the joint distribution of two independent random variables (IRVs) is

$$F(X, Y) = F(X)F(Y). \tag{C.16}$$

It follows immediately that

$$f(X, Y) = f(X)f(Y). \tag{C.17}$$

Therefore, in the case of IRVs it is possible to calculate the joint distribution or density directly as the product of the marginal distributions or densities. Although a powerful tool, the above results give little insight into determining the joint distribution of two arbitrarily dependent RVs.